Doctoral Thesis

Inatel
Instituto Nacional de Telecomunicações

A 64-element and Dual-Polarized SICL-based Slot Antenna Array Development Applied to TDD Massive MIMO

Hugo Rodrigues Dias Filgueiras

March/2022

A 64-element and Dual-Polarized SICL-based Slot Antenna Array Development Applied to TDD Massive MIMO

Hugo Rodrigues Dias Filgueiras

Ph.D. Thesis Confirmation presented at National Institute of Telecommunications (Inatel), as part of the requirements for obtaining a Ph.D. Title in Telecommunication Engineering.

SUPERVISOR:
Prof. Dr. Arismar Cerqueira Sodré Junior

Santa Rita do Sapucaí – MG, Brazil

2022

Filgueiras, Hugo Rodrigues Dias
F481a
A 64-element and dual-polarized SICL-based slot antenna array development applied to TDD massive MIMO / Hugo Rodrigues Dias Filgueiras. – Santa Rita do Sapucaí, 2022.
129 p.

Orientador: Prof. Dr. Arismar Cerqueira Sodré Junior.
Tese de Doutorado em Telecomunicações – Instituto Nacional de Telecomunicações – INATEL.
Inclui bibliografia.

1. 5G 2. Antenas em Fendas 3. Arranjo de Antenas 4. MIMO Massivo 5. Ondas Milimétricas. 6. Doutorado em Telecomunicações. I. Sodré Junior, Arismar Cerqueira. II. Instituto Nacional de Telecomunicações – INATEL. III. Título.

CDU 621.39

Ficha Catalográfica elaborada pelo Bibliotecário da Instituição
CRB6-2718 – Paulo Eduardo de Almeida

Approval Page

PhD Thesis Defense defended and approved in March 15th, 2022, by the judging committee:

Prof. Dr. Arismar Cerqueira Sodré Junior

Inatel (Brazil)

Prof. Dr. Felipe Augusto Pereira de Figueiredo

Inatel (Brazil)

Prof. Dr. Pei Xiao

University of Surrey (UK)

Prof. Dr. Raj Mittra

University of Central Florida and Pennsylvania State University (USA)

Doctorate Course Coordinator

Prof. Dr. José Marcos Câmara Brito

To my family and friends, for the support
and guidance over the years.

Acknowledgments

I am thankful for God, for illuminating my path and every decision made in my life so I can get so far. Even when things get complicated and quite obscure, there was no doubt regarding His presence in my life in every turn on the way.

I am also thankful for my parents for the unconditional love, support, patience (a lot of it!) and everything else they gave to me since the day I was conceived. Alcino and Sheila, my father and mother, I love you as much as love can be felt. Nothing that I am today would be possible without you two, so thank you.

My wife has a lot to do with my choices too. Maria Clara has been my partner in life since 2010 and my friend since I can remember. Every grown-up decision I have made in my life was already considering her in my life. In her case, love was essential, but patience and support every single day were determinants for this final research. Throughout the Ph.D., we have had many difficulties in life in which we had to learn how to deal with and learn how to be married in the process. Babe, thank you very much for simply existing in my life and making it so much better. You give me the strength to keep going every single day and, until our last one, I must love you.

To the National Institute of Telecommunications, my sincere thank you! I have moved to Santa Rita do Sapucaí from Volta Redonda in 2011, with only 18 years old, and have lived a lot of interesting things in this wonderful city. Inatel has given me my Telecommunication diploma, my master's degree and now I am pursuing my doctorate degree in this same institution. I am thankful for the research structure, the friendly environment and even more for every teacher who gave me just a little of his massive telecommunication and academic experience. More specifically, thank you Prof. Arismar Cerqueira Sodré Junior, for the advices, teachings, technical discussions, career tips, trust and friendship throughout the years since my Master

research in 2016. I am also thankful for our academic mother Gisele Moreira dos Santos, who always has been there when we needed any documents or pieces of information.

To my laboratory companions, you guys have the most important contribution to my career development. We have grown together; we have deeply discussed every technical thing that was possible to discuss. We have argued with each other every single day so everyone could get better and evolve as a researcher and as a telecommunication engineer. Beyond that, we have lived side-by-side every day and I am happy to call my co-workers as friends. Some of them must be named in my "thank you note": Tiago Henrique Brandão, Luiz Augusto Melo Pereira, Matheus Sêda Borsato Cunha, Eduardo Saia Lima and Ramon Maia Borges, thank you very much for the partnership every time I have needed. For the discussions, help, support and friendship throughout this research. Our brainstorming has been essential for the discoveries made in my Ph.D. and our laughs too! Thank you, guys.

I am also really thankful for the judging committee, which has really contributed with this work with high-level discussions and suggestions. Prof. Dr. Pei Xiao, Prof. Dr. Raj Mittra, Prof. Dr. Felipe Figueiredo and Prof. Dr. Arismar Cerqueira, thank you all for the advisements and suggestions throughout my Ph.D. and also the suggestions made in the confirmation exam.

I am thankful for the National Institute of Telecommunication Foundation (FINATEL) and the Brazilian Coordination for the Improvement of Higher Education Personnel (CAPES) for the scholarship. This work was partially supported by RNP, with resources from MCTIC, Grant No. No 01245.010604/2020-14, under the 6G Mobile Communications Systems project of the Radiocommunication Reference Center (Centro de Referência em Radiocomunicações - CRR) of the National Institute of Telecommunications (Instituto Nacional de Telecomunicações - Inatel), Brazil. Thank the financial support from CNPq, CAPES, FINEP and FAPEMIG.

Index

List of Publications

Journals:

[1] **Hugo Rodrigues Dias Filgueiras** and A. Cerqueira Sodre Junior, "A 64-element and Dual-Polarized SICL-based Slot Antenna Array Development Applied to TDD Massive MIMO," *IEEE Antennas and Wireless Propagation Letters*, Vol. 21, no. 4, pp. 750-754, April 2022, DOI: 10.1109/LAWP.2022.3144916.

[2] **H.R.D. Filgueiras**, E. S. Lima, T. H. Brandão and Arismar Cerqueira S. Jr., "5G NR FR2 Femtocell Coverage Map Using an Omnidirectional Twisted SWAA," in *IEEE Open Journal of Antennas and Propagation*, vol. 2, pp. 72-78, 2021.

[3] **H. R. D. Filgueiras,** R. Marques, A. R. Augusto, S. H. Nunes, H. L. de Faria and Arismar Cerqueira S. Jr, "HIRF Broadband Full-Wave Virtual Testing and Experimental Validation," in *IEEE Electromagnetic Compatibility Magazine*, vol. 10, no. 2, pp. 39-46, 2nd Quarter 2021.

[4] J. A. P. Ribeiro, **H. R. D. Filgueiras,** Arismar Cerqueira S. Jr, F. Beltrár-Mejía and J. R. Mejía-Salazar, "3D-Printed Quasi-Cylindrical Bragg Reflector to Boost the Gain and Directivity of cm- and mm-Wave Antennas," in *Sensors*, vol. 21, no. 23, pp. 8014, 2021.

[5] E. C. Vilas Boas, **H. R. D. Filgueiras**, I. Feliciano da Costa, J. A. J. Ribeiro and A. C. Sodre Jr, "Dual-band switched-beam antenna array for MIMO systems," in *IET Microwaves, Antennas & Propagation*, vol. 14, no. 1, pp. 82-87, 2020.

[6] E. S. Lima, R. M. Borges, L. A. Melo Pereira, **H. R. D. Filgueiras**, A. M. Alberti and A. Cerqueira S. Jr., "Multiband and Photonically Amplified Fiber-Wireless Xhaul," in *IEEE Access*, vol. 8, pp. 44381-44390, 2020.

[7] R. M. Borges, L. A. M. Pereira, **H.R.D. Filgueiras**, *et al.*, "DSP-Based Flexible-Waveform and Multi-Application 5G Fiber-Wireless System," in *Journal of Lightwave Technology*, vol. 38, no. 3, pp. 642-653, 1 Feb.1, 2020.

[8] **H. R. D. Filgueiras,** James R. Kelly, Pei Xiao, I. F. da Costa and Arismar Cerqueira S. Jr., "Wideband Omnidirectional Slotted-Waveguide Antenna Array Based on Trapezoidal Slots," in *International Journal of Antennas and Propagation*, vol. 2019, pp. 1-8, 2019.

[9] **H. R. D. Filgueiras**, R. M. Borges, M. Caldano Melo, T. H. Brandão and Arismar Cerqueira Sodré, "Dual-Band Wireless Fronthaul Using a FSS-Based Focal-Point/Cassegrain Antenna Assisted by an Optical Midhaul," in *IEEE Access*, vol. 7, pp. 112578-112587, 2019.

[10] T. H. Brandão, **H.R.D. Filgueiras,** *et al.*, "Dual-band System composed by a Photonics-based Radar and a Focal-Point/Cassegrain Parabolic Antenna," in *Journal of Microwaves, Optoelectronics and Electromagnetic Applications*, v. 17, p. 567-578, 2018.

Under Review:

[11] **H.R.D. Filgueiras**, T. H. Brandão, L. A. M. Pereira and Arismar Cerqueira S. Jr., "A Novel Figure of Merit for Massive MIMO Antenna Arrays," in *Transactions on Antennas and Propagation (TAP)*, 1st submission in October, 2021, 2nd submission in February, 2022.

Conferences:

[12] **H.R.D. Filgueiras**, M. A. S. Ferrero, I. F. da Costa, J. V. da Silva and Arismar Cerqueira S. Jr., "A Novel Full-Wave Methodology for Channel Estimation in Digital mMIMO Applications," *16th European Conference on Antennas and Propagation (EuCAP)*, Madrid, Spain, 2022.

[13] **H. R. D. Filgueiras** and Arismar Cerqueira S. Jr., "SICL-based Antenna Array for 5G Massive MIMO Applications in mm-waves," *Antenna Measurement Techniques Association (AMTA)*, Florida, USA, 2021.

[14] T.H. Brandão, **H. R. D. Filgueiras** and Arismar Cerqueira S. Jr., "Low-Coupling and Dual-Polarized Horn-based Antenna Array aimed to Massive MIMO Applications," *European Microwave Week*, Longon, UK, 2021.

[15] **H.R.D. Filgueiras,** T. H. Brandão, L. O. Veiga, A. Roza, R. Marques, C. W. M. Silva, S. Nunes, H. Lemos and Arismar Cerqueira S. Jr., "Dual-Polarized Vivaldi Antenna Development for Multi-technology Testbed," *International Microwave and Optoelectronics Conference (IMOC)*, Fortaleza, Brazil, 2021.

[16] T.H. Brandão, **H. R. D. Filgueiras** and Arismar Cerqueira S. Jr., "mm-Waves 1x8 Mechanical Reconfigurable Phase-Shifter aimed to Switched-Beam Applications," *International Microwave and Optoelectronics Conference (IMOC)*, Fortaleza, Brazil, 2021.

[17] L.C Alexandre, L.O. Veiga, Agostinho Linhares, H.R.D. Filgueiras and Arismar Cerqueira S. Jr, "Technological Solution for Enabling 5G NR and TVRO Peaceful Coexistence in C-band," *15th European Conference on Antennas and Propagation (EuCAP)*, Düsseldorf, Germany, 2021.

[18] F. Zanella, **H. R. D. Filgueiras**, G. Valério, C. A. Dartora, A. A. Mariano and S. A. Cerqueira, "Nano-Antenna Modelling Based on Plasmonic Charge Distribution for THz-based 6G Applications," *2nd 6G Wireless Summit (6G SUMMIT)*, Levi, Finland, 2020.

[19] **H.R.D. Filgueiras**, R. Marques, A. R. Augusto, S. H. Nunes, H. L. de Faria and Arismar Cerqueira S. Jr., "Numerical High Intensity Radiated Field Assay with Experimental Validation," *19° Simpósio Brasileiro de Micro-Ondas e Optoeletrônica e 14° Congresso Brasileiro de Eletromagnetismo (MOMAG 2020)*, Niterói, Brazil, 2020.

[20] **H.R.D. Filgueiras**, T. H. Brandão and Arismar Cerqueira S. Jr., "Análise de Desempenho de Sistemas FSO com MIMO sob Condições de

Turbulência," *XXXVIII Simpósio Brasileiro de Telecomunicações e Processamento de Sinais - SBrT 2020*, Florianópolis, Brazil, 2020.

[21] **H. R. D. Filgueiras**, T. H. Brandão, J. R. Kelly, P. Xiao and Arismar Cerqueira S. Jr., "Novel Approach for Designing Broadband Slot Antennas," *13th European Conference on Antennas and Propagation (EuCAP)*, Krakow, Poland, 2019.

[22] **H.R.D. Filgueiras**, M. S. B. Cunha, P. H. F. Santos P. H. F. and Arismar Cerqueira S. Jr., "Antena "N" de alto desempenho para aplicações NFC," *XXXVII Simpósio Brasileiro de Telecomunicações e Processamento de Sinais (SBrT)*, Petrópolis, Brazil, 2019.

[23] **H.R.D. Filgueiras**, M. C. Melo, T. H. Brandão and Arismar Cerqueira S. Jr., "Dual-band Parabolic Antenna for High Capacity Backhauls and Fronthauls," *SBMO/IEEE MTT-S International Microwave and Optoelectronics Conference (IMOC)*, Aveiro, Portugal, 2019.

[24] J. R. Kelly, K. Y. Alqurashi, C. Crean, **H. R. D. Filgueiras**, Arismar Cerqueira S. Jr., Z. Chen and H. Wong, "High Gain Beam Steerable Phased Array Incorporating Reconfigurable Parasitics formed from Liquid Metal," *IEEE-APS Topical Conference on Antennas and Propagation in Wireless Communications (APWC)*, Granada, Spain, 2019.

Acronym List

3GPP	Third Generation Partnership Project
5G	fifth generation of mobile communication
6G	sixth generation of mobile communication
BBU	baseband processing unit
BH	backhaul
BS	base station
CA	carrier aggregation
CAPEX	capital expenditure costs
CDMA	code-division multiple access
CO	central office
CRR	radiocommunications reference center
CSI	channel state information
DL	downlink
DL-SCH	downlink shared channels
DMRS	demodulation reference signal
D-RAN	distributed radio access network
DSP	digital signal processing
DU	distribution unit
E	electric field
ECC	envelope correlation coefficient
EGC	equal gain combining
eMBB	enhanced mobile broadband communication
eNodeB	enhanced NodeB
EVM_{RMS}	root mean square error vector magnitude
FDD	frequency division duplexing
FDMA	frequency-division multiple access
FR	frequency range
FSS	frequency selective surface
H	magnetic field
IFFT	inverse fast Fourier transform
IoT	Internet of things
LOS	line of sight

LTE	long-term evolution
M2M	machine-to-machine
MH	midhaul
MIMO	multiple-input multiple-output
mMIMO	massive multiple-input multiple-output
mMTC	massive-machine-type communication
mm-waves	millimeter-waves
MRC	maximum ratio combining
NFV	network function virtualization
NLOS	non line-of-sight
NR	new radio
NYU	New York University
OFDM	orthogonal frequency division multiplexing
OFDMA	orthogonal frequency division multiple access
OPEX	operational expenditure costs
PBCH	physical broadcast channel
PCB	printed circuit board
PDF	probability density function
PEC	perfect electric conductor
PMC	perfect magnetic conductor
PS	pure selection
PSS	primary synchronization signal
PTFE	polytetrafluoroethylene
QAM	quadrature amplitude modulation
QoS	quality of service
QPSK	quadrature phase-shift keying
RAN	radio access network
RB	resource block
RF	radiofrequency
RRC	radio resource control
RRU	remote radio unit
SCS	subcarrier spacing
SDN	software-defined network
SICL	substrate integrated coaxial line
SIW	substrate integrated waveguide
SLL	side-lobe level
SNR	signal-to-noise ratio
SSB	synchronization signal block
SSS	secondary synchronization signal
SWAA	slotted waveguide antenna array
TDD	time division duplexing
TDMA	time-division multiple access
TE	transverse electric
TEM	transverse electromagnetic

TM	transverse magnetic
UE	user element
UHF	ultra-high frequency
UL	uplink
UL-SCH	uplink shared channels
URLL	ultra-reliable low latency
UTA	University of Texas at Austin
V2X	vehicle to everything
WDM	wavelength-division multiplex
WOCA	wireless and optical convergent access

Resumo

Este trabalho é concernente ao desenvolvimento de um arranjo de antenas para a banda de 26 GHz com polarização dupla e 64 elementos baseados em fendas impressas, excitados independentemente por uma linha do tipo coaxial integrada ao substrato (SICL-SAA), a fim de garantir baixo nível de acoplamento mútuo entre os mesmos. Os elementos irradiadores são constituídos por fendas impressas no substrato Rogers CuClad 233 de 0,25 mm de espessura. Na camada inferior, implementa-se cavidades individuais atuando como refletores, para garantir irradiação normal ao plano do arranjo sem comprometer o nível de acoplamento mútuo. Conduz-se um procedimento de desenvolvimento em 11 etapas, obtendo-se um modelo numérico final da SICL-SAA com 1,8 GHz da banda, de 25 a 26,8 GHz (6,9%), considerando coeficiente de reflexão (S_{11}) menor que -10 dB e 1 GHz da banda para S_{11} < -20 dB. Os resultados experimentais se mostram em excelente concordância com os numéricos. A SICL-SAA provê 2 GHz de banda para S_{11} < -10 dB, acoplamento mútuo abaixo de -23 dB ao longo de toda banda, *envelope correlation coefficient*, ECC < -60 dB, abertura de feixe de 85° em ambos os planos e ganho de 7,4 dBi em 26 GHz. Além disso, uma nova metodologia para avaliar arranjos de antenas em sistemas MIMO TDD (*time division duplexing*), baseada no diagrama de irradiação do arranjo, é concebida visando interpretar a cobertura e a resolução espacial, por meio da inspeção dos múltiplos feixes resultantes do processo de codificação digital. Particularmente, o impacto na resolução espacial do sistema MIMO massivo (mMIMO) é avaliado em função da correlação entre canais, utilizando uma abordagem exclusivamente em rádiofrequência (RF). Propôs-se uma nova figura de mérito (fator Λ) capaz de quantificar os múltiplos feixes criados pela sobreposição de diagramas de irradiação do sistema mMIMO.

Palavras-chave: 5G, antenas em fendas, arranjo de antenas, MIMO massivo, ondas milimétricas, SICL e TDD.

Abstract

This research is focused on the development of a 64-elements and dual-polarized slot-based antenna array, fed by a substrate integrated coaxial line (SICL-SAA), with the purpose of reducing mutual coupling in the 26 GHz band. We propose using printed slot antenna array elements on a 0.25 mm thickness Rogers CuClad 233. At the bottom layer, individual cavities are applied for ensuring boresight radiation without compromising the low mutual coupling level among the array elements. An eleven-step design procedure is carried out, reaching on a final numerical SICL-SAA with 1.8-GHz bandwidth, from 25 to 26.8 GHz (6.9%) considering reflection coefficient (S_{11}) lower than -10 dB and a 1-GHz bandwidth for S_{11} < -20 dB. Experimental results have been shown in excellent agreement with full-wave numerical simulations, demonstrating up to 2 GHz bandwidth from 24.5 to 26.5 GHz for S_{11} < -10 dB for all array elements. The mutual coupling between adjacent elements is kept lower than -23 dB for the entire bandwidth, *envelope correlation coefficient*, ECC < -60 dB and the radiating elements provide an 85º beamwidth in both planes ($\varphi = 0°$ and $\varphi = 90°$) and 7.4 dBi gain. Furthermore, a new radiation pattern-based methodology for time division duplexing (TDD) massive MIMO (mMIMO) array evaluation is conceived, which enables to interpret the antenna array coverage and spatial resolution, by inspecting the array resultant multiple beams. Particularly, the impact on the mMIMO spatial resolution is also conducted as a function of the channel correlation, by means of an exclusively radiofrequency approach, i.e. with the advantage of not considering the system-level features. The proposed figure of merit (Λ factor) quantifyies the created multiple beams by the overlapped radiation patterns from mMIMO systems.

Keywords: 5G, antenna array, massive MIMO, millimeter waves, SICL, slot antennas and TDD.

Chapter 1
1. Motivations and Contextualization
1.1. Contextualization

Mobile communication systems have been continuously evolving as the data traffic demand increases. In the past, the evolution between consecutive mobile generations, e.g., from 3G to 4G (third and fourth generations of mobile communication), mainly consisted of redesigning the mobile radio access network (RAN) in order to allow increasing data traffic and enhancing user experience [1].

The radio access network can be implemented in multiple and distinct architectures. Basically, it could be divided on a distributed RAN (D-RAN), centralized RAN (C-RAN) and a variation between those concepts [2][3]. The D-RAN architecture consists of physically locate the baseband processing unit (BBU) with the remote radio unit (RRU) in the base station (BS). Such an approach was widely adopted in 3G architecture, however, it demands high management and cost effort. 4G embraced the C-RAN architecture approach, in which the BBU has been moved to a central office (CO), centralizing the baseband processing functions from multiple BBUs at the same location, giving rise to the BBU pool concept. On C-RAN architectures, RRU may be located a few kilometers (up to 20 km) from BBU, connected by a physical link denominated as fronthaul (FH) [2-4]. As a consequence, C-RAN provides broadband communication to mobile users at capital (CAPEX) and operational (OPEX) expenditure costs and high spectral efficiency. Notably, CAPEX is extremely reduced in the enhanced NodeB (eNodeB), which only contains RRU, allowing an increase in the number of sites and reach remote areas [2-4].

Tactile devices, machine-to-machine (M2M) communication, industry 4.0 and Internet of things (IoT) are some examples, which have been expanding the provided applications, technologies and services. Such applications require high connectivity and reliability with low latency networks. In this way, an entirely new architecture must be taken into consideration, since the data traffic is not the only concern in this new generation. According to 3GPP (Third Generation Partnership Project), the fifth generation of mobile communication (5G) is expected to cover three main scenarios [5-7]: enhanced mobile broadband communication (eMBB); massive-machine-type communication (mMTC); ultra-reliable low latency (URLL) applications [3-7]. Additionally, remote and rural access have been also triggering a lot of interest, mainly in wide countries, such as Brazil, China, and Canada [8].

Many architectures have been proposed to attend 5G scenarios. The CHARISMA project (Converged Heterogeneous Advanced 5G Cloud-RAN Architecture for Intelligent and Secure Media Access) [9] consists of a hierarchical approach, with active nodes between the central office (CO) and the user elements (UEs). Each node has its own management unit to perform data storage, processing and routing functionalities, which means the data can be routed through the smallest path to achieve low latency networking. Additionally, CHARISMA offers open access as features intrinsic to its design and a security network by applying software-defined network (SDN) and network function virtualization (NFV), creating an applicable solution for 5G usage scenarios [9][10].

The 5G CHAMPION is an architecture proposed to integrate multi-functionalities, such as beamforming, satellite service provisioning, virtualized infrastructure, software reconfiguration, accurate positioning and high-speed solutions [11]. Most challenging 5G scenarios are proposed to be addressed by 5G CHAMPION, including: latency in the millisecond range; capability to serve very dense user environments without performance degradation; capability to provide multiple network functions; support high precision/integrity ubiquitous location-based services and timing; capability to support various types of IoT, and interoperability between them; capability to efficiently provide omnipresent 5G services [11]. 5G CHAMPION has been implemented on a testbed targeting the provision of 5G services at the 2018

Winter Olympics in Korea [12]. They were able to obtain a total transmission data rate of 2.5 Gbit/s on a 1-GHz bandwidth signal, making use of dual-polarized array antennas in both transmission and reception [12].

Particularly, our research group has also contributed to 5G projects worldwide. The Radiocommunications Reference Center (CRR from Portuguese "Centro de Referência em Radiocomunicações) has its goal of implementing mechanisms for allowing Brazil to occupy a prominent place in the telecommunication sector, by researching, evaluating, and developing technologies and solutions aimed to Brazilian society demands, considering specific demographical, geographical, and economic features [13]. It focused on four subject areas including long-range, high-capacity radio links, wireless broadband access, 5th-generation networks and satellite communication links [13]. Under the CRR scope, multiple projects have also been proposed including the development of a 5G transceiver with Brazilian human resources and technology using flexible and manageable waveform applied to long-range communications [14][15]. The 5G Range project aimed for designing, developing, implementing and validating mechanisms to enable 5G networks to provide an economically effective solution for Internet access in remote areas [14-16]. The 5G IoT project, which has aimed its research on developing IoT technical solutions embedded into a 5G network [17] and, finally, the "6G Brasil" [18][19], which is the first Brazilian project focused on 6G and has established a formal partnership with 6G Flagship Project from Oulu University in Finland, which leads 6G research worldwide [20].

In this context, the transport network has to be able to offer high data traffic to support any of the proposed architectures, so they can handle and manage the user data demand, but also the network physical and virtualized functionalities, which enables the network to operate with low latency and high reliability [4]. In future generation mobile network architecture, as exampled in [21], the core network is connected to a CO, containing the BBU pool, through a backhaul (BH), typically using wavelength-division multiplex (WDM) systems. A BH can also connect multiple COs to each other. COs provide the baseband processed signals to a distribution unit (DU) or directly to RRUs. The connections between BBUs and DU are named midhaul (MH)

and between BBUs and RRUs are named FH. Fronthauls are also used to connect DUs to RRUs and MHs are also used to provide high data traffic to femtocells [22]. Some wireless FH could be assisted by a photonic MH, giving rise to the concept of a hybrid 5G-Xhaul [21-23]. The proposed architecture has to jointly use wireless [24] and photonics [25-27] techniques for increasing the spectral efficiency and, as a result, the data traffic in both optical MH and wireless FH. Furthermore, supercells operating with reasonable throughputs (up to 600 Mbit/s) can manage a massive number of micro and femtocells in its interior, creating extremely high throughput hotspots reaching up to 20 Gbit/s per user [28-30], giving rise to a heterogeneous network (HetNet).

5G has been recently standardized in its first release [31], 3GPP-Release 15, which has not been idealized for attending all four scenarios. In the next decade (the 2020s), as technology and market emerge, new standard releases are going to be proposed to encompass all 5G scenarios. Beyond 5G, 6G is a vision for the 2030s, which will require a much wider and holistic approach to identify the system needs [32]. M. L. K. Latva-aho claims the main idea of 6G consists of a network based on the term "Ubiquitous Wireless Intelligence" [32], which means services following users everywhere and seamlessly, with wireless connectivity and context-aware smart services and applications for both human and non-human users.

6G use cases are expected to require very sophisticated operations, with high-resolution localization at the centimeter level, high-accuracy inter-device synchronicity within 1 μs, support an ultra-dense network with 100 devices per cubic meter and battery lifetime up to 20 years [32]. The 5G premises in terms of low latency and reliability are going to be much more restrictive in the 6G network [32][33], i.e. industrial usage expects a maximum latency of only 0.1 ms and reliability of at least 99.9999% [32]. Like all of the previous mobile communication evolution (from 1G to 5G), enhancing the system throughput is one of the many premises. 6G is expected to be the first wireless standard with links requiring peak throughput exceeding the 1 Tbit/s benchmark [32-34]. To support multiple links and user experience with such a high rate, the terahertz (THz) frequency range is expected to be exploited in 6G due to its huge capacity and bandwidth [32-34].

Regardless of the technology, the millimeter-waves (mm-waves) frequency range also consists itself as a promising solution for providing large bandwidth, reaching capacities up to several gigabits per second [35]. However, higher frequencies introduce severer propagation and penetration losses, which can be minimized with beamforming and massive multiple-input multiple-output (mMIMO) techniques [39]. High-gain and steerable antennas can transmit and receive signals in specific directions for compensating the high path loss [37], whereas mMIMO can considerably increase the system capacity and reliability by taking advantage of multiple propagation channels yielding multiplexing and diversity gains [38][39].

Until 2015, the University of Texas at Austin (UTA) and the New York University (NYU) were the two most important research groups in propagation studies performed at mm-waves bands in dense urban environments. In 2015, Rappaport *et al.* have compiled all of their group previous work into a unique invited paper [40]. In their manuscript, they have reported the hardware used for performing mm-waves measurements and obtained omnidirectional and directional path loss models based on thousands of wide-bandwidth power delay profiles. Additionally, they reported a spatial statistic of mm-waves channels, intending to extend ultra-high frequency (UHF) and microwave standard channel models to properly represent the phenomena in mm-waves channels. Finally, they have introduced a novel channel modeling named spatial lobe, which characterizes the mm-waves outdoor urban channels up to 73 GHz.

Massive MIMO pledges to increase channel capacity in a multi-user MIMO scenario with a simple precoding scheme [41]. Such a feature is obtained under the under the assumption of asymptotically favorable propagation, i.e., the channel vectors become asymptotically orthogonal as the number of antennas increases, which means the inter-user interference vanishes [42]. Massive MIMO is capable of supporting both extremely scattering environments and pure line of sight (LOS) scenarios [43]. The first one, in which the channels become orthogonal due to the law of large numbers, they are usually modeled by independent and identically distributed (i.i.d.) Rayleigh distributed channel coefficients. While the last one, considering a pure LOS environment, without any scattering objects between transmitter and receiver, the

channel matrix is obtained by using geometric models, assuming a far-field approximation, i.e., planar wavefront [41].

For a massive MIMO system to properly work, each antenna has to be independently controlled and weighted [41]. Although having an outstanding performance in terms of system capacity, such an approach is quite expensive due to the need for a massive number of RF chains [41-43]. In its first implementation, 5G NR has adopted a switched-beam approach [31]. The switched-beam consists of a massive number of antennas, subdivided into sub-arrays for creating multiple directive beams. Each beam can cover a small angular area with high gain and the user information is transmitted on a unique beam. In this architecture, UE identifies the beam with the higher signal-to-noise ratio (SNR) and informs BS for transmitting its information through it [31]. Such an approach is more cost-effective and can provide high SNR to UE, but cannot provide the massive spectral efficiency enhancement expected from the mMIMO scheme.

1.2. Aim of the Research

The current work has the aim of presenting the development and characterization of a SICL-based slot antenna array (SICL-SAA) operating in the 26 GHz band. It consists of an antenna array for a time division duplexing (TDD)-based digital mMIMO applications. Furthermore, the work presents a new radiation pattern-based methodology analysis for antenna array performance evaluation into a multipath environment, including the proposal of a new metric for quantifying its operability. The proposed SICL-SAA is printed-based with independent feeding for taking advantage of uncorrelated channels when needed.

1.3. Literature Review on mm-waves and Massive MIMO Antennas

This Section presents a state-of-the-art antenna proposal review. The aim is to identify the most recent proposed electromagnetic solutions, disruptive technologies and application-oriented antenna proposals. Manuscripts published from 2016 to 2021 have been preferred for this literature review. Initially, we will focus on 5G and beyond

antennas, not considering the array proposals. Posterior, we shall present state-of-the-art manuscripts focused on antennas applied to MIMO and mMIMO systems.

In 2016, Jang-Soon Park *et al.* have proposed a tilted combined beam antenna for 5G communications using the 28-GHz band [44]. Their antenna was based on two distinct radiating elements, a patch antenna and a waveguide aperture. The first one has been used to achieve a wide beamwidth in the azimuth plane and the second one to increase the antenna directivity in the elevation plane. The authors have been able to combine the two patterns, obtaining a relatively high gain at the desired tilted direction, by adjusting the distance between the patch and waveguide aperture. Their prototype has presented bandwidth from 27.2 to 28.7 GHz considering the reflection coefficient magnitude (S_{11}) lower than -15 dB. The prototype has presented gain varying from 7.2 to 7.41 dBi throughout the operating bandwidth and, at 28 GHz, presented beamwidth of 52° and 72° in the electric (*E*) and magnetic (*H*) planes, respectively. Finally, the antenna maximum gain has been tilted to $\theta = 53°$. The authors have claimed their antenna has been developed for 5G mobile communications, to be used as an external RF terminal, since the prototype was not small enough to be fully integrated inside practical UE devices. However, at that time, there was no fixed standard related to 5G communications, so they have claimed that their work could be meaningful research as an opening research stage of 5G communications.

A 28 GHz switched-beam antenna based on surface PIN (S-PIN) diodes has been proposed for 5G systems in 2017 by Yevhen Yashchyshyn *et al.* [45]. This research has been aimed to achieve multiple beams and the possibility of switching among them. The designed reconfigurable antenna has been composed of two identical radiating reconfigurable structures based on a slotted waveguide antenna array (SWAA) with a slit etched along its narrower wall. The slit is flared in the direction of the *E*-field for acting as a sectoral horn, improving the radiation efficiency part of the waveguide is filled with Polytetrafluoroethylene (PTFE), giving rise to a transition between guided wave and air. The reconfigurable semiconductor circuit has been composed of 15 reconfigurable slots with embedded S-PIN diodes. In this way, the SWAA's slots could be reconfigured by appropriate biasing, enabling or not radiation

through them. The authors have been able to switch among five beams, pointed towards 0°, ±30° and ±45°. In the worst-case scenario, the antenna has provided 600 MHz bandwidth centered at 28.05 GHz, reaching up to 7 dBi gain.

Two distinct works have been selected from the year 2019. In [46], Chun-Xu Mao *et al.* have proposed a planar sub-millimeter-wave array antenna with enhanced gain and reduced sidelobes for 5G broadcast applications at 26 GHz. The proposed prototype is based on two dipoles and a substrate integrated cavity as a power splitter. The dipoles are placed side-by-side to create an omnidirectional pattern in the azimuth plane. The authors have been able to combine the dipole and cavity resonance to achieve a wide bandwidth from 27 to 29.5 GHz. Finally, they have structured an eight-element array for enhancing gain, reaching up to 12 dBi omnidirectional gain for broadcast applications. By managing both amplitude and phase of each element, they have been able to significantly reduce the array side-lobe level. Concurrently, Yin Zhang *et al.* in [47], have proposed a 2-element array based on a dielectric resonator. It consists of a slot-based antenna fed by a stripline. On top of it, a dielectric with relative permittivity of 9.8 is set to act as a cavity resonator. Finally, two additional striplines have been placed to increase isolation between the ports, reaching 24 dB. The prototype has provided approximately 10-dBi gain at 28 GHz and 1.29-GHz bandwidth centered at 27.84 GHz.

A wideband printed circuit board (PCB)-stacked Luneburg lens antenna with a flared open edge for multi-beam scanning application at 5G millimeter-wave (mmW) band has been proposed in 2021 by Xi Wang *et al.* in [48]. In their research, they have aimed to fulfill the increased data traffic in mobile communications by proposing a high-gain (15.4 dBi) and wideband antenna (from 26 to 37 GHz) for switched-beam applications. It consists of 11 resonant elements, shifted among each other by 15°, around a unique circular Luneburg lens.

In [49], Mei Xue *et al.* have proposed a low-profile millimeter-wave broadband metasurface antenna with four resonances. The radiating element has been composed of four groups of co-planar patches with different dimensions, which have contributed to a high and stable gain. The authors have proposed to etch dual slots on the patch,

directly fed by the coaxial probe, to reduce cross-polarization levels. Their prototype has provided a 16% bandwidth centered at 28.4 GHz with gain of 10.1 dBi.

Table 1.1 summarizes the main results achieved by the authors from [44-49], intending to identify the used technologies, electromagnetic features and proposed applications. One can note the possibility of applying multiple and distinct technologies for encompassing 5G demands. Multiple probes [48] or S-PIN-based SWAAs [45] could be employed for switched-beam application, whereas waveguide-based antennas [44][45], dielectric resonators [47], Luneburg lenses [48] and cavities could be used for increasing the antenna gain [46]. Printed [44][48] and multi-resonance antennas [49] are preferable for their flexibility and enhanced bandwidth.

Table 1.1 – State-of-the-art antenna solutions in mm-waves.

Reference	Technology	Bandwidth	Gain	Application
[44]	Printed and waveguide	27.2 to 28.7 GHz	7.2 to 7.41 dBi	External RF terminal for 5G
[45]	SWAA embedded with S-PIN	27.75 to 27.35 GHz	7 dBi	Switched-beam
[46]	Dipoles and substrate integrated cavity	27 to 29.5 GHz	12 dBi	Omnidirectional coverage for broadcast
[47]	Slot-based antenna with dielectric resonator	27.2 to 28.5 GHz	10 dBi	Low-order MIMO applications
[48]	PCB-stacked Luneburg lens	26 to 37 GHz	15.4 dBi	Switched-beam
[49]	Multi resonance metamaterial based on co-planar patches	26.3 to 30.7 GHz	10.1 dBi	Low-profile applications

The following manuscripts are focused on MIMO and mMIMO solutions. All papers consider the MIMO system to define the antenna array requirements. It is worth highlighting the need for low coupling among elements for ensuring low correlation among channels on a mMIMO environment [42]. In 2016, Yue Gao *et al.* have proposed a dual-polarized patch antenna array with low coupling among elements [50]. The proposed system was composed of 144 ports operating at 3.7 GHz, based on 18 low-profile subarrays on a 360° coverage. Each subarray consists of four patches with two ports, one for each polarization. The feeding network has been used to obtain the dual-polarization feature on a 4-element patch array, with higher gain and lower

coupling when compared to a dual-port single patch. The authors have proposed a system with 18 subarrays, each one composed of a 4-element array, and ensured mutual coupling among any elements no higher than -35 dB for good mMIMO performance.

A dipole-based and dual-polarized antenna array has been proposed by Mohana Vamshi Komandla *et al*. in 2017 [51]. They have proposed the usage of cross-polarized dipoles, one on each side of a substrate, with a cavity below the structure for ensuring radiation in a unique direction by acting as a reflector. A 16-element array is proposed, each one with two connectors (±45° polarizations), operating from 4.9 to 6 GHz. The coupling among elements has been kept lower than -20 dB throughout the operating bandwidth. The authors have evaluated the envelope correlation coefficient (ECC), which should be kept as low as possible and characterizes the array diversity performance, i.e., isolation among channels. They have claimed that an acceptable value for ECC is lower than 0.3 and their proposed prototype has been kept lower than 0.1. Finally, their prototype has been numerically simulated for proving its beamforming feature and they have been able to steer a unique beam up to 50° and simultaneously create four beams for a multi-user environment. The antenna gain has been kept above 20 dBi in all of the evaluated scenarios.

The research conducted by Xi Yang *et al.* in 2017 [52] consists of a design and implementation of a TDD-based 128-element mMIMO system. The authors have presented an analytical model, a link-level simulation and the design and implementation of a 128-element mMIMO antenna array prototype to validate the concept. Experiments have been conducted by transmitting a real-time video at uplink (UL) and data transmission at downlink (DL) with multiple single-antenna users, simultaneously, on a 20-MHz bandwidth. Their system made use of orthogonal frequency division multiplexing (OFDM) waveform and, in its structure, a 10-ms frame, subdivided into 10 subframes of 1-ms each, carries the information. Since their system allocation is software programmable, it has been possible to vary the allocation of some time-slots (two time-slots compose one subframe) for UL and others for DL according to the application demand. A pilot OFDM symbol, i.e., known information, is transmitted at UL for channel estimation and compensation at DL. The system

should properly work if the channel does not change on an UL and DL period, i.e., channel coherence time. If the coherence time is respected, the system takes advantage of the channel reciprocity.

The prototype composed of 128 dipole antennas has been divided into 8 sub-arrays of 16 antenna elements in [52], arranged on a planar array. The elements were printed-dipoles mounted above metallic reflectors. The array operates from 3.8 to 4.3 GHz and the elements are spaced of 0.8λ (at 4.1 GHz) in both horizontal and vertical directions. The authors have claimed they have opted for a simple array deployment, so no sophisticated technique is implemented. In any case, element isolation higher than 25 dB has been ensured for good mMIMO performance. From the antenna point-of-view, 0.8λ spacing is acceptable for ensuring a unique directive beam, without grating lobes, however, such a spacing could degrade mMIMO performance due to lack of channel diversity. Nonetheless, since the array has been divided into 8 sub-arrays, the spacing among them has been kept close to 3.2λ, which ensures good channel diversity and, consequently, good mMIMO performance. As a final result, the authors have reached up to 69.12 bit/s/Hz spectral efficiency on a quadrature phase-shift keying (QPSK) modulation, which provides only 1 bit/s/Hz on a conventional single antenna system, proving the expected spectral efficiency enhancement pledged by a mMIMO system.

Yun Hu *et al.* have proposed in 2018 [53] a digital multi-beam array at 26 GHz with 16 elements. The manuscript has focused on the beamsteering feature instead of mMIMO application. The antenna element was a dual exponentially tapered slot, which is a variation of a conventional Vivaldi antenna. Each element has been fed by a substrate integrated waveguide (SIW), so the slot can be properly excited with a propagating mode, i.e., transverse electric (TE), and the coupling among elements could be minimized, which has been kept lower than -20 dB with a distance between adjacent elements of 6 mm. The 16-element array feeds a planar lens, based on the Jerusalem Cross, which increases the system gain from 20 to 25 dBi and enables beamsteering from -50° to 50° by properly weighting the signal phase in each antenna element.

In 2020, Shunli Li *et al.* [54] have proposed a metasurface lens antenna, with dual-polarization, envisaging to cover both multibeam and mMIMO applications. The authors have designed a Jerusalem Cross-based metasurface lens for increasing gain and enabling multibeam applications. The lens is fed by a 64-element patch array, with dual-polarization, operating from 5.17 to 6.1 GHz. The manuscript presents a scanning angle of ±25° with gain up to 22.4 dBi and 3.3 dB variation. Coupling among elements has been kept lower than -20 dB in the bandwidth of interest. The authors have been able to create a switched-beam feature by selecting one port of the feeding array, or a combination of ports. By switching among ports, multiple beam angles have been created. Multiple beams at the same frequency have been achieved, whereas frequency division multiplexing could be implemented in each one for increasing system throughput.

In [55], Murat Temiz *et al.* have conducted a study on the impact of antenna array geometry on indoor mMIMO networks. Their research has investigated the impact of channel correlation on a prototyped mMIMO system aiming to identify an antenna array geometry with reduced mutual coupling and channel correlation. Since spatial channel diversity is the fundamental merit of mMIMO technique, high channel correlation would significantly restrict its performance. The authors have designed a directional wideband single antenna element for the antenna array and UEs. The antenna element has been designed to operate from 4 to 4.7 GHz and consisted of a patch antenna based on a suspended plate technique, which has an air gap between radiating element and reflector for increasing radiation efficiency. Two planar antenna arrays have been designed for channel correlation analysis, a uniform antenna array and a shifted antenna array. The uniform one has been composed of equally distributed elements, aligned in both horizontal and vertical directions, whereas the shifted one consisted of shifting lines of radiating elements in the matrix, increasing the spacing between adjacent elements without compromising the array area. The obtained results have proved the shifted array outperforms the uniform conventional array in terms of network capacity, due to a lower level of mutual coupling among antenna elements and lower channel correlation (lower than -15 dB for the linear array and -20 dB for the shifted array), especially in line-of-sight (LOS) propagation.

A further investigation on the array topology has been made by Yanki Aslan *et al*. in 2021 [56]. Their research has been based on evaluating the elements periodicity. They have claimed that aperiodic element distribution within an array has the potential of increasing the system quality of service (QoS) in terms of inter-user interference reduction. The authors have considered four array topologies: ***i)*** 64-element array with fully aperiodic elements distribution and minimum distance among adjacent elements of 0.5λ; ***ii)*** 256-element array with fully aperiodic elements distribution and minimum distance among adjacent elements of 0.5λ; ***iii)*** 256-element array with quasi-modular distribution and minimum distance among adjacent elements of 0.5λ; ***iv)*** 256-element array with quasi-modular distribution and minimum distance among adjacent elements of λ. The system scenario has been considered as an isolated cell, in a pure LOS environment, with a *N*-element antenna array at the BS providing services to *K* single omnidirectional antenna users simultaneously, using the same frequency on spatial division multiplexing scheme. The arrays performance have been evaluated in terms of interference among multiple users. The authors have concluded higher-order aperiodic arrays have the potential of mitigating inter-user interference by reducing side-lobe level (SLL) and reducing channel correlation. In addition, further spacing adjacent elements for at least λ, increases inter-user interference due to SLL increment, but only on a LOS environment, in which no multipath is considered. The advantages of using more spaced elements in this scenario are regarding thermal dissipation and spacing for electronics on active antenna deployments, with limited impact on QoS.

Table 1.2 compiles the main contributions achieved by the authors from [50] to [56]. It has been possible to observe, most papers presented in literature regarding antenna arrays for beamforming, MIMO and mMIMO applications make use of simple antenna elements. The selected papers have been based on patch, dipole or slot antennas and, the main contributions are related to the feeding network, beamsteering range, the technique used for reducing mutual coupling and spectral efficiency enhancement. Regardless of the application, reducing mutual coupling is an important performance metric and has been kept lower than -20 dB in most papers. Some of the authors have ensured the low coupling by evaluating the distance between adjacent elements, which have been mostly kept between 0.5λ and 1λ for beamforming and

multiple beams applications. MIMO and TDD-based digital mMIMO systems make use of channel diversity, so the antennas have to be further spaced, and this feature has been possible to be verified in literature as well.

Table 1.2 – State-of-the-art antenna array solutions for beamforming, MIMO and mMIMO applications.

Ref.	Technology	Array topology	Bandwidth [GHz]	Mutual coupling	Elements spacing	Application	Contribution
[50]	Patch	18 low profile subarrays on a 360° coverage	3.6 to 3.8	< -35 dB	λ	MIMO	Dual polarized antenna scheme achieved by feeding network on a 4-patch radiating element
[51]	Dipole with cavity acting as reflector	16-element planar array (4x4)	4.9 to 6	< -20 dB	0.6λ	Analog Beamforming	Beamsteering up to 50° and multiple-beam feature up to 4 beams
[52]	Dipole with reflector	128-elements planar array	3.8 to 4.3	< -25 dB	3.2λ between sub-arrays	TDD-based digital mMIMO	69.12 bit/s/Hz spectral efficiency on a QPSK modulation
[53]	Tapered slot	16-element planar array and metasurface lens	24.5 to 27.5	< -20 dB	0.52λ	Digital beamsteering	Increased gain with metasurface lens and beamsteering from -50° to 50°
[54]	Patch	64-element planar array and metasurface lens	5.17 to 6.1	< -20 dB	0.8λ	Multiple-beam	Scanning angle of ±25° and switched-beam feature by port selection
[55]	Patch antenna based on a suspended plate	18-element uniform and shifted planar antenna arrays	4 to 4.7	< -20 dB	0.64λ	TDD-based digital mMIMO	Shifted antenna array geometry introduction for decreasing channel correlation
[56]	Patch	256-elements aperiodic distribution	26.5 to 29.5	Not provided	0.5λ or 1λ	Beamforming	Aperiodic distribution antenna array for decreasing channel correlation

An important piece of information regarding Table 1.2 is the frequency of operation and their relation with the application. Table 1.1 has reported antennas

applied to 5G in the millimeter-wave frequency range, whereas Table 1.2 reports the array solutions applied to beamforming, MIMO and mMIMO systems, which are also aimed at 5G networks. Many papers in the literature claim higher frequencies enable high-order antenna arrays due to the small wavelength, however, most papers on arrays presented in the literature are focused on sub-6 GHz bandwidth. Such a feature has been observed to be a proof-of-concept solution since implementation costs in higher frequencies are a considerable impairment. In any case, all of the proposed techniques presented in Table 1.2 can be applied at mm-waves.

Finally, it has been noticed there are more solutions in the literature applied to beamforming, beam steering, and multiple-beam applications than to TDD-based digital mMIMO ones. Once again, this is related to implementation costs, since beamforming techniques can be applied with a smaller number of RF chains. However, it is important to keep in mind the real scenario environment: those analog beamforming and steering techniques establish few users (some manuscripts are applied to a unique user) under a LOS condition, whereas TDD-based digital beamforming guarantees multiple-access for multiple users due to channel diversity in a non-LOS (NLOS) scenario, which is more realistic on a dense urban environment. For research purposes, it is important to keeping contributing with TDD-based mMIMO, considering the expected electronics and RF evolution and cost reduction throughout the next years.

Our research group, Laboratory Wireless and Optical Convergent Access (WOCA), from Inatel, have proposed multiple antennas applied to 5G networks in literature in the past few years [21][57-63]. In 2017, I. F. da Costa *et al.* have proposed the first optically controlled reconfigurable SWAA at mm-waves in literature [57]. They have proposed a SWAA with embedded photoconductive switches for controlling the slots electrical lengths, enabling frequency tunability and radiation pattern reconfiguration. The prototype has achieved bandwidth management through two different frequency bands, namely: a 10.95% band centered at 28 GHz and a 4.25% band at 38 GHz and gains of 8 and 9 dBi at 28 and 38 GHz, respectively.

Two novel designs have been proposed by our group in 2018 [58]. Arismar Cerqueira S. Jr. *et al.* have manufactured a 28-GHz omnidirectional SWAA based on

metallic rings for disturbing a traveling wave inside a dielectric waveguide. Furthermore, dual-band and dual-coverage SWAA for simultaneous operation at 28 and 38 GHz is also proposed, based on two groups of slots with different electrical lengths on the opposite faces of a waveguide. The first one provides bandwidth from 26.85 to 29 GHz, with a considerable high-gain for omnidirectional antennas of approximately 12 dBi, whereas the second one has been able to operate from 24.7 to 32.2 GHz and 35.5 to 39.15 GHz simultaneously, providing gains of 12.6 and 15.6 dBi at 28 and 38 GHz, respectively.

The dual-band SWAA proposed in [58] has been applied on a switched-beam application by E. C. Vilas Boas *et al.* in 2019 [59]. They have arranged four SWAA elements, rotated of 30° between them, for creating a dual-band and switchable four-beam antenna array. The prototype applicability for MIMO systems has been evaluated as a function of mutual coupling among SWAAs, which has been kept lower than -35 dB throughout the entire evaluated bandwidth (24 to 40 GHz).

E. C. Vilas Boas *et al.* have further investigated SWAA antennas at mm-waves in 2020 [60]. In this new research, a low-profile and high-gain SWAA at 26 GHz is proposed for point-to-point links and a potential solution for self-backhaul applications. The prototype has been composed of 27 slots, milled into a standard WR28 waveguide wall, with six pairs of metal grooved structures located in parallel to the array axis. The slot array has been able to decrease beamwidth in the *H*-plane to 3° and the grooved pairs have reduced the beamwidth to 10° in the *E*-plane, reaching a remarkable gain of 27.7 dBi with no need for metallic reflectors. The prototype has provided a bandwidth from 25.88 to 26.78 GHz.

A second approach for point-to-point link has been proposed in 2019 [21]. Our group has implemented a dual-band wireless fronthaul using a frequency selective surface (FSS)-based focal-point/Cassegrain antenna assisted by an optical midhaul. It consists of concept, implementation and experimental performance analysis of innovative fiber-wireless architecture for 5G-Xhaul networks. The main contribution was regarding the integration of optical backhauls and midhauls with a dual-band wireless fronthaul based on the use of an antenna modeled according to the previous one proposed by T. H. Brandão *et al.* in [24] for dual-use radar applications. The

antenna consists of two feeders, one operating at 7.5 GHz and the second at 28 GHz, a main reflector and a FSS-based sub-reflector. The last one acts as a conductor at 28 GHz and is electromagnetic transparent at 7.5 GHz, enabling the dual-band feature using a unique main reflector. We have been able to reach up to 18 Gbit/s with root mean square error vector magnitude ($EMV_{RMS\%}$) in accordance with the 3GPP Release 15 requirements over a 25 km optical midhaul followed by a 20-m wireless fronthaul operating simultaneously in both frequency bands. Posteriorly, in [61], the same antenna has been applied on a novel system topology with an enhanced optical midhaul, in which the RF signal is photonically amplified using non-linear optical effects.

Finally, in [62], we have proposed an omnidirectional SWAA operating at 24 GHz for femtocell applications. We have proposed a novel approach for designing wideband omnidirectional SWAAs, which has been based on trapezoidal-shaped slots with two different electrical lengths, as well as a twisted distribution of slot groups along the array longitudinal axis. The trapezoidal slot is formed by gradually increasing the slot length between the waveguide interior and exterior surfaces. In this way, a smoother impedance transition between waveguide and air is provided to enhance the array operating bandwidth. In addition, we have proposed a twisting technique, responsible to improve the omnidirectional pattern, for reducing the gain ripple in the azimuth plane. Experimental results have demonstrated 1.09 GHz bandwidth centered at 24 GHz (4.54% fractional bandwidth), gain up to 14.71 dBi over the operating bandwidth, and only 2.7 dB gain variation in the azimuth plane. The proposed antenna array and its enabling techniques have presented themselves as promising solutions for mm-waves application, including 5G eMBB communications on indoor scenarios, which has been proved in 2021 [63].

The omnidirectional SWAA has been installed on an indoor femtocell operating at 24.15 GHz. A 91-m^2 indoor coverage has been demonstrated and its coverage map estimated by measurements of EVM_{RMS} parameter at 36-spatially distributed reception points throughout the laboratory [63]. The 5G NR femtocell has been set with 50-MHz bandwidth and 30 kHz-spaced subcarriers, giving rise to 104.8 Mbit/s data rate, whose signal quality is analyzed accordingly to the 3GPP Release 15 recommendations. LOS

and NLOS propagation scenarios have been evaluated, implying EVM_{RMS} variation from 3.13% to 19.4%. Coverage of 94% and 89% are achieved for QPSK and 16-QAM (Quadrature Amplitude Modulation) systems, respectively, demonstrating its applicability to the deployment of 5G NR femtocell operating in mm-waves. Table 1.3 compiles the main contributions from the WOCA 5G antenna proposals.

Table 1.3 – Lab. WOCA antenna solutions applied to the 5G networks.

Ref	Technology	Number of elements	Feeding points	Bandwidth [GHz]	Application	Contribution
[57]	SWAA	4	1	27.6 to 30.8 and 36.8 to 38.4	Dual-band sectorial coverage at mm-waves	First optically controlled SWAA at mm-waves proposed in literature
[58]	Ring-based travelling wave	13	1	26.85 to 29	Omnidirectional eMBB indoor femtocell	High-gain omnidirectional antenna
	SWAA	32	1	24.7 to 32.2 and 35.5 to 39.15	Dual-band sectorial coverage at mm-waves	Simultaneous dual-band and dual-coverage SWAA at mm-waves
[59]	SWAA	128	4	24.42 to 31.58 and 36.1 to 39.9	Switched-beam	Dual-band and four-beam switchable antenna array at mm-waves
[60]	SWAA with grooves	27	1	25.88 to 26.78	Point-to-point link applied to self-backhaul	Low-profile high-gain antenna proposal
[21]	FSS-based Focal-point/ Cassegrain parabolic	2	2	6.9 to 8 and 25.85 to 30.15	Point-to-point link applied to hybrid X-haul	Concept and implementation of a dual-band wireless FH, using a FSS-based focal-point/Cassegrain antenna, assisted by an optical MH
[61]	FSS-based Focal-point/Cassegrain parabolic	2	2	6.9 to 8 and 25.85 to 30.15	Point-to-point link applied to hybrid X-haul	Implementation of a multiband and photonically amplified fiber-wireless (FiWi) Xhaul based on RoF technology and four-wave mixing (FWM) nonlinear effect
[62]	SWAA	144	1	23.45 and 24.54	Omnidirectional eMBB indoor femtocell	High-gain omnidirectional antenna
[63]	SWAA	144	1	23.45 and 24.54	Omnidirectional eMBB indoor femtocell	Implementation and coverage map estimation of a 24.15 GHz femtocell with 104.8 Mbit/s throughput

As previously discussed, our group has proposed antennas applied to 5G networks with distinct technologies and a plurality of applications operating from 6.9 to 39.9 GHz. SWAAs have been used for both omnidirectional [58][62][63] and sectorial [57][58] applications and dual-band at 28 and 38 GHz have been also explored in this antenna topology. The ring-based traveling-wave omnidirectional antenna [58] is a variation of a conventional SWAA and has been proposed for eMBB indoor femtocell environments. For X-haul applications, it has been proposed SWAA with grooves for gain enhancement and a dual-band solution for parabolic antennas, integrating both focal-point and Cassegrain systems into a unique structure with only one reflector [21][61]. Besides antenna development, our group has focused on system topology proposals based on optical and wireless convergence [21][61] and femtocell digital performance analysis [63], which prove all proposed antennas applicability under real scenarios by implementing them on operational 5G systems.

1.4. Research Contribution

The Thesis main contributions are the following ones:

1 Concept and design of the SICL-SAA, a dual-polarized 64-element antenna array for TDD-based digital mMIMO applications, which is based on printed slot antennas fed by a substrate integrated coaxial line (SICL) for reducing coupling among elements. Each slot has its own cavity for reflecting the wave in broadside direction without increasing mutual coupling.

2 Statistical and numerical analysis of the array structure under distinct multipath channel conditions, including the proposal of new metric for quantifying its operability. This evaluation is a novel method for relating the resultant radiation pattern considering channel compensation under distinct levels of correlation among received signals (paths). It is the first time in literature, to the best of our knowledge, that conclusions are made regarding the resultant radiation pattern on TDD-based digital mMIMO, in which radiating elements are spaced of at least one wavelength for decreasing channel correlation, taking advantage of multipath and no well-defined and predominant beam is expected to be formed.

1.5. Thesis Outline

The Thesis is structured in five Chapters. Chapter 2 presents the theoretical fundamentals on 5G enabling technologies including an investigation on the 5G NR standard regarding resource allocation, duplexing techniques and multiple-access solutions. Furthermore, diversity, multiplexing and mMIMO fundamentals are also explored in Chapter 2 and their consequences on the system performance. Chapter 3 is regarding the antenna array design, numerical evaluation and electromagnetic performance analysis. Chapter 4 is regarding the proposal of a new radiation pattern-based methodology for TDD-based massive MIMO array evaluation, including the introduction of a new metric for quantifying its applicability. Finally, Chapter 5 outlines the conclusions and future works regarding the research.

Chapter 2
2. 5G Enabling Technologies

This Chapter aims to present the theoretical foundations regarding 5G technologies. Section 2.1 has the purpose of discussing the features of 5G physical layer standard, 5G NR. We shall present the applied technologies which are needed to understand the research contributions. Section 2.2 will further explore the mathematical modeling and theoretical concepts of MIMO and mMIMO systems.

2.1. 5G New Radio (NR)

5G has been firstly standardized in its first release (Release 15) in 2019 [31]. In this standard, mainly the eMBB scenario has been targeted to be covered. Three classes have been proposed for meeting the challenging scenarios: energy and spectral efficiency; new frequency ranges; novel architecture topologies. Energy and spectral efficiency are related to new waveforms, resource allocation, duplexing and multiple access techniques, whereas new frequency ranges target unused, unexplored and even unlicensed bandwidths, including carrier aggregation (CA) techniques for increasing throughput. Finally, architecture topology focuses on proposing novel solutions for latency reduction and efficient network management and orchestration employing SDN, network virtualization and slicing [5][9][11][21][31]. Furthermore, Release 16 has been also announced in 2020 [64], which complements Release 15 by introducing new core and RAN resources and includes industrial IoT, URLLC, mMTC and vehicle to everything (V2X) applications and use cases.

The complete 5G NR standard document compiles a plurality of versions, technical specifications and technical reports. We envisage approaching in this thesis

only the 5G NR aspects that are concerning to the research contribution, namely: frequency range definition; numerology; duplexing techniques; resource allocation; multiple access; switched-beam.

2.1.1. Frequency Ranges

5G NR has implemented two frequency ranges for access networks, namely: Frequency Range 1 (FR 1) and Frequency Range 2 (FR 2). The first one is from 410 to 7,125 MHz [31] and the last one from 24.25 to 52.6 GHz [65]. In both FRs, the UE channel bandwidth supports a single NR RF carrier in the UL or DL. From a BS perspective, different UE channel bandwidths may be supported within the same spectrum for transmitting and receiving from UEs. Transmission of multiple carriers to the same UE or multiple carriers to different UEs within the BS channel bandwidth can be supported [31][65].

3GPP has specified in the NR standard a plurality of bandwidth allocation for attending the challenging scenarios expected for 5G networks, enabling flexibility and throughput management. Table 2.1 summarizes the bandwidth allocation for each FR. One can note even for FR 1, bandwidth up to 100 MHz, which is five times higher than the LTE technology. This feature already enables higher throughput in the sub-6 GHz bandwidth when compared to previous mobile networks. In FR 2, an unprecedented bandwidth allocation of up to 400 MHz is presented, for extremely high throughput applications in eMBB scenarios [31][65].

Table 2.1 – 5G NR bandwidth allocation [31][65].

Frequency Range	Bandwidth allocation [MHz]
FR 1 (410 to 7125 MHz)	5, 10, 15, 20, 25, 30, 40, 50, 60, 80 or 100
FR 2 (24.25 to 52.6 GHz)	50, 100, 200 or 400

2.1.2. Numerology

5G NR proposes the numerology (μ) concept for enabling flexibility in subcarrier spacing (SCS). Contrarily to previous mobile access technology, such as LTE, in which the spacing between adjacent subcarriers was fixed (at 15 kHz), 5G NR enables varying this spacing up to 60 kHz and 480 kHz in FR 1 and FR 2, respectively

[31][65]. Increasing SCS enables higher throughputs since more bandwidth can be allocated for each subcarrier. SCS, in Hz, is given by

$$\mathrm{SCS} = 2^{\mu}(15 \times 10^{3}), \qquad (2.1)$$

in which μ can assume values of 0, 1 or 2 in FR 1, giving rise to 15, 30 or 60 kHz SCS, respectively. In FR 2, μ can be set as 2, 3, 4 or 5, enabling SCS of 60, 120, 240 or 480 kHz, respectively [31][65].

A resource block (RB) is defined as the minimum resource allocation unit available for a user [66-68] and is composed of a time-frequency matrix containing the information. In the time domain, a resource block is composed of one frame period of 10 ms and, each frame is composed of ten 1-ms subframes [66][67]. Figure 2.1 presents the subframe composition and portioning in subframes and time-slots. Some conclusions can be taken by further analyzing Figure 2.1: ***i)*** a time-slot is composed of 14 OFDM symbols regardless of the numerology; ***ii)*** increasing the μ value and, consequently, SCS, entails portioning a subframe into multiple time-slots in 2^{μ} factor, i.e, for μ = 2, 4 time-slots compose a sub-frame; ***iii)*** since the subframe is fixed in 1 ms time-period and the time-slots are always composed of 14 OFDM symbols, increasing μ implicates in transmitting more symbols in the same time-period, hence, increasing throughput. Such a feature corroborates with the previous claim, which defends that the numerology concept has been proposed in the 5G NR frame structure for enabling flexibility and attending multiple and challenging scenarios [66-68].

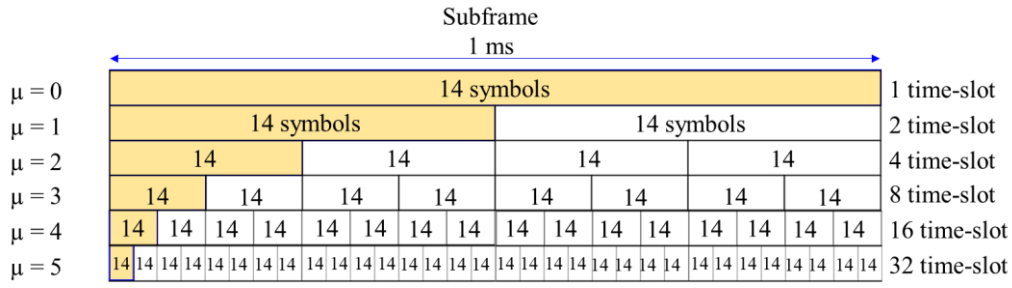

Figure 2.1. 5G NR subframe composition and portioning for distinct numerologies.

In addition, 5G NR proposes to further portioning a time-slot in two, creating the concept of a mini time-slot of 7 OFDM symbols. Reducing time-slot duration is interesting for low-latency applications in URLLC environments since the system processing time is directly related to the time duration of a slot [67][68].

2.1.3. Duplexing Techniques

Duplexing techniques are regarding the way UL and DL share the propagating environment [69]. In this research, is important to understand the differences, pros and cons between the duplexing techniques, since it is fundamental to understand the channel and the manners to estimate it for properly design a MIMO system. Duplexing scheme is one of the first features to analyze when designing a channel estimator in mobile communication networks [70]. Many important works in literature investigate the pros and cons of frequency division duplexing (FDD) and TDD, especially applied to MIMO systems [69-78].

Figure 2.2 illustrates both FDD and TDD scenarios and its inset presents the UL and DL representation in frequency and time domains. FDD systems make use of two isolated frequency bands for separating UL and DL, whereas TDD occupies a single frequency band and differs UL and DL in distinct subframes in the time domain [69]. TDD systems have an unpaired spectrum, which is suitable for mobile communication due to spectrum scarcity, whereas FDD makes use of paired spectrum. By analyzing traffic controlling, TDD tends to be more flexible and enables unbalanced traffic between DL and UL. The synchronization in FDD systems is simpler than in TDD systems since the former can provide a more efficient interference cancelation due to distinct frequency channels. TDD synchronization is a complex issue since all UL signals have to arrive at BS at the same time, for avoiding DL-to-UL interference [69].

The most important feature for this research is regarding the channel state information (CSI). CSI is used for estimating the channel and TDD has the advantage of enabling channel reciprocity [69-78]. Channel reciprocity means the same channel, without any changes, in the UL is used in DL, which is possible if a time-period between them is smaller than the channel coherence time since they share the same frequency bands. This means it is possible to estimate the DL channel via the measurement of UL signals. This enables the transmitter to efficiently collect CSI without excessive feedback overhead and complicated mobile terminal processing [69][73][74].

Channel estimation using FDD on mMIMO systems could be an issue since pilot symbols and subcarriers in DL would be used for acquiring CSI. CSI would be informed to BS in the UL, on another frequency band and, only then, DL could be compensated. The problem with this arrangement is the CSI age, which can get old and outdated [70][73][77].

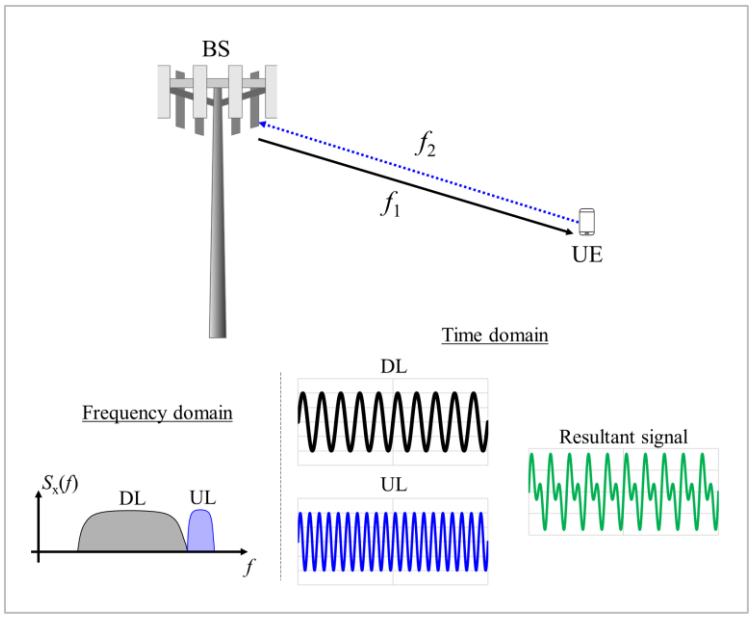

(a) FDD scheme

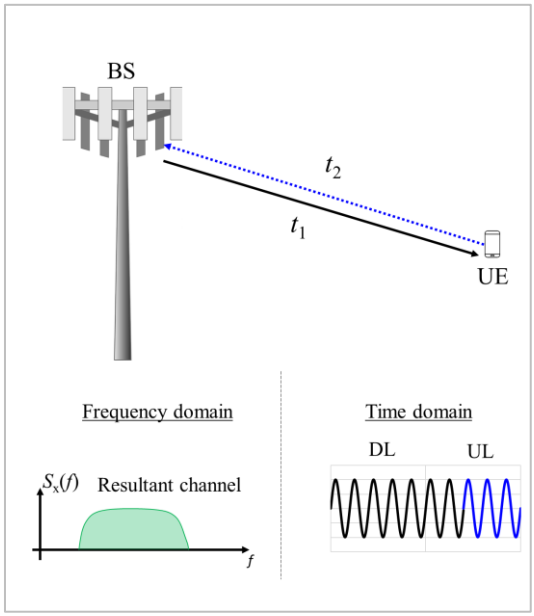

(b) TDD scheme

Figure 2.2. Duplexing techniques illustration and resultant channel in frequency and time domains.

5G NR makes use of both duplexing technologies, once again for enabling flexibility in its RAN [31][65]. Table 2.2 compiles the standardized operation

bandwidth and their adopted duplexing scheme for distinct applications in FR 1. Table 2.3 compiles the same information for FR 2. The n75 and n76 bands, in FR 1, are supplementary downlink channels and, since there is no UL in those frequencies, no duplexing technique is required. Analogously, the bands n80, n81, n82, n83, n84 and n86 are supplementary UL channels, with no DL and no duplexing mode is needed. Note that FR 2 operates in TDD mode for all available bands, enabling TDD-based digital mMIMO employment due to channel reciprocity.

Table 2.2 – 5G NR operating bandwidth in FR 1 [31].

Operating band	UL bandwidth [MHz]	DL bandwidth [MHz]	Duplexing mode
n1	1920 – 1980	2110 – 2170	FDD
n2	1850 – 1910	1930 – 1990	FDD
n3	1710 – 1785	1805 – 1880	FDD
n5	824 – 849	869 -894	FDD
n7	2500 – 2570	2620 – 2690	FDD
n8	880 – 915	925 – 960	FDD
n12	699 – 716	729 – 746	FDD
n20	832 – 862	791 – 821	FDD
n25	1850 – 1915	1930 – 1995	FDD
n28	703 – 748	758 – 803	FDD
n34	2010 – 2025	2010 – 2025	TDD
n38	2570 – 2620	2570 – 2620	TDD
n39	1880 – 1920	1880 – 1920	TDD
n40	2300 – 2400	2300 – 2400	TDD
n41	2496 – 2690	2496 – 2690	TDD
n50	1432 – 1517	1432 – 1517	TDD
n51	1427 – 1432	1427 – 1432	TDD
n66	1710 – 1780	2110 – 2200	FDD
n70	1695 – 1710	1995 – 2020	FDD
n71	663 – 698	617 – 652	FDD
n74	1427 – 1470	1475 – 1518	FDD
n75	-	1432 – 1517	-
n76	-	1427 – 1432	-
n77	3300 – 4200	3300 – 4200	TDD
n78	3300 – 3800	3300 – 3800	TDD
n79	4400 – 5000	4400 – 5000	TDD
n80	1710 – 1785	-	-
n81	880 – 915	-	-
n82	832 – 862	-	-
n83	703 – 748	-	-
n84	1920 – 1980	-	-
n86	1710 - 1780	-	-

Table 2.3 – 5G NR operating bandwidth in FR 2 [65].

Operating band	UL bandwidth [GHz]	DL bandwidth [GHz]	Duplexing mode
n257	26.5 – 29.5	26.5 – 29.5	TDD
n258	24.25 – 27.5	24.25 – 27.5	TDD
n260	37 – 40	37 – 40	TDD
n261	27.5 – 28.35	27.5 – 28.35	TDD

2.1.4. Resource Allocation

As previously mentioned, a RB is defined as the minimum resource allocation available for a user [66-68] and is composed of a time-frequency matrix containing the information. How to allocate information into a RB is the main concerning of this Section.

Figure 2.3 presents a resource allocation example in accordance with the 3GPP recommendations for FR2 UE conformance tests [65], setting μ = 3, i.e., SCS = 120 kHz. In this configuration, a 10-ms frame is composed of ten 1-ms subframes, which carriers eight 125-μs time-slots. Each time-slot is composed of 14 OFDM symbols. The TDD mode has been considered, with time-slots from 36 to 40 and from 76 to 80 set as uplink shared channels (UL-SCH). The downlink shared channels (DL-SCH) have been configured with two distinct modulations for emulating a multi-service application: the time-slots from 1 to 35 as QPSK; time-slots from 41 to 75 as 16-QAM. Additionally, the synchronization signals, namely: primary synchronization signal (PSS) and secondary synchronization signal (SSS), which enable UE to obtain the frame timing and the cell identity [65], have been properly set. Both PSS and SSS have not been given into consideration for throughput calculation, due to their lower percentage in allocation that would not significantly affect the final throughput. Finally, 12 demodulation reference signal (DMRS) symbols in each time slot, considering all 12 sub-carriers, have been considered as well.

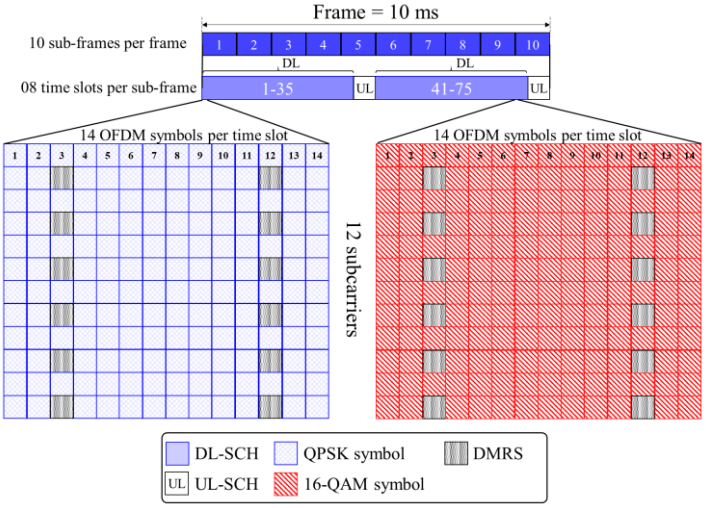

Figure 2.3. TDD mode 5G NR resource allocation in accordance with the 3GPP recommendations for FR2 UE conformance tests.

Table 2.4 summarizes the main 5G NR variables considering one frame period, aiming the total throughput (R_b) calculation using

$$R_b = \frac{(a \times N_{sc} - N_{QPSKDMRS}) \times k_{QPSK} \times N_{QPSKSCH} \times N_{RB}}{T_{frame}} + \frac{(b \times N_{sc} - N_{16DMRS}) \times k_{16QAM} \times N_{16SCH} \times N_{RB}}{T_{frame}}. \quad (2.2)$$

Table 2.4 – Main variables for the throughput calculation considering the resource allocation from Figure 2.3.

Variable	Quantity	Value
a	Number of QPSK symbols per subcarrier	14
b	Number of 16-QAM symbols per subcarrier	14
N_{sc}	Number of subcarriers	12
$N_{QPSKDMRS}$	Number of QPSK DMRS symbols per RB	12
N_{16DMRS}	Number of 16-QAM DMRS symbols per RB	12
k_{QPSK}	Number of bits per QPSK symbol	2
k_{16QAM}	Number of bits per 16-QAM symbol	4
$N_{QPSKSCH}$	Number of QPSK DL-SCH channels	35
N_{16SCH}	Number of 16-QAM DL-SCH channels	35
N_{RB}	Number of allocated RB	32
T_{frame}	Frame periodicity	10 ms

A 104.8 Mbit/s throughput in the DL has been generated using this 5G NR configuration. One can note (2.2) is basically considering the total bits of information in one frame-period and normalizing the total amount by the time in which they are transmitted. This is one of the possible resource allocations in 5G NR. Many variations could be employed, such as: modifying PSS and SSS quantities according to QoS; using FDD mode, which would entail occupying all time-slots, but consider some sub-carries for UL; modifying modulation index; dividing multi-application in the frequency-domain instead of time-domain; considering the same modulation index in the entire allocation; etc. The important concept to keep in mind is the allocation can be managed and throughput calculated considering total transmitted bits per time-period.

2.1.5. Multiple Access

Multiple access is the technology that enables multiple users to share the same RF channel [79]. On a synchronized system, each user can transmit its information on a time-period, characterizing as time-division multiple access (TDMA) [79][80]. Such multiple access mode, commonly used in 2G [69], increases synchronization

complexity since BS should be able to control all connected users considering each of their propagating channel delay spread [69].

A second approach is sharing the resource in the frequency domain, using frequency-division multiple access (FDMA) [69]. This approach is simpler than TDMA from the synchronization point-of-view, however suffers from poorer spectral efficiency, since a guard band is needed for ensuring low interference among users [69], entailing in reduced throughput. Due to simplicity, FDMA has been implemented in 1G AMPS (North American Advanced Mobile Phone System) systems. 3G has widely used a code-division multiple access scheme (CDMA) [79], which has been named as WCDMA technology (wideband CDMA). A CDMA scheme makes use of orthogonal codes for identifying each user. The information from each user is codified by their own code and, then, they can share the same time-frequency resources [79]. Among TDMA, FDMA and CDMA, the last one presents itself as the most efficient in frequency use, since the information of all users can be transmitted in the same resource, with relative complexity regarding synchronization and no interference among users is ensured due to code orthogonality [79].

Both 4G and 5G NR have applied the OFDMA (orthogonal frequency division multiple access) scheme [81]. It is important to remember the concept of the OFDM waveform before exploring the multiple-access operational principle. OFDM consists of a multi-carrier modulation for combatting frequency-selective channels, i.e., multipath channels [82]. The concept is converting this frequency-selective channel into multiple frequency-flat subchannels, with partially overlapping spectra [82]. OFDM waveform has been applied in 4G systems and 5G NR has also implemented it [31][65].

As previously said, this research is focused on TDD-based digital mMIMO applications and, only the needed theoretical fundamentals for understanding the research application and contribution shall be discussed in this document. The next paragraphs will further discuss CDMA and OFDMA technologies, which will be later used to understand the mMIMO pre-coding scheme.

Let us consider the Figure 2.4 scenario. It is a simple multiple-access scenario for understanding the CDMA operational principle. Note that BS transmits a unique signal (T_x) composed of the summation of all users pieces of information (u_i). This is possible since each user information is firstly multiplied by its own code (c_i) and, every used code inside a mobile cell should be orthogonal among each other [79][83]. These codes could be sequences generated by a classical Walsh-Hadamard matrix [83], given by (2.3) and (2.4) [83][84]. The interesting feature of Walsh-Hadamard sequences generated from the same matrix is that all of them are orthogonal among each other, i.e., the correlation between any given lines or column is zero [84].

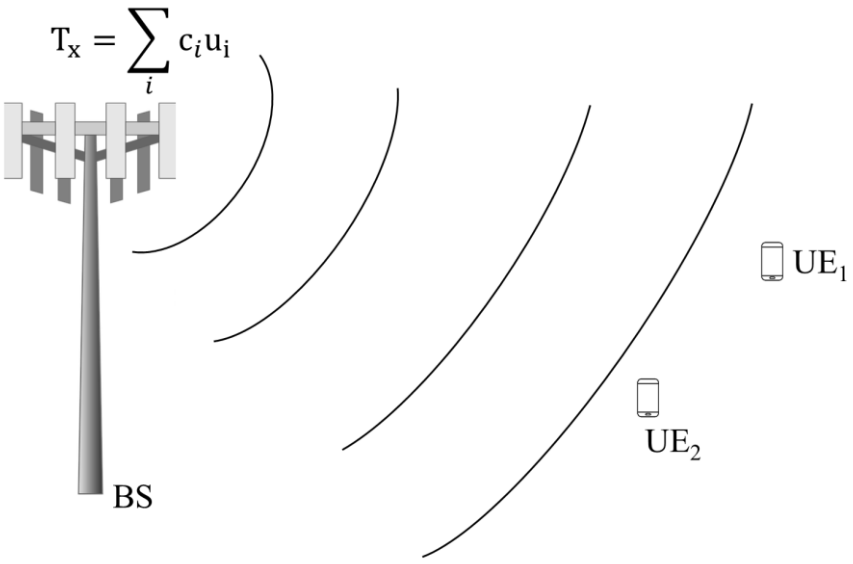

Figure 2.4. Multiple access scenario using CDMA scheme.

$$\mathbf{H}(2) = \begin{bmatrix} 1 & 1 \\ 1 & -1 \end{bmatrix} \tag{2.3}$$

$$\mathbf{H}(2n) = \begin{bmatrix} \mathbf{H}(n) & \mathbf{H}(n) \\ \mathbf{H}(n) & -\mathbf{H}(n) \end{bmatrix} \tag{2.4}$$

Let us consider a simple example for illustrating Figure 2.4 scenario: ***i***) two users are sharing the same channel; ***ii***) the information of each user is u_1 = -1 and u_2 = 1; ***iii***) the Walsh-Hadamard code for each user is c_1 = [1 -1 1 -1] and c_2 = [1 1 -1 -1]; ***iv***) each user has knowledge of its own spreading code. Considering this scenario, the transmitted signal by BS would be

$$T_x = u_1 c_1 + u_2 c_2 = [-1 \quad 1 \quad -1 \quad 1] + [1 \quad 1 \quad -1 \quad -1] = [0 \quad 2 \quad -2 \quad 0]. \tag{2.4}$$

At the receiver, each user receives the incoming signal and correlates it with its own spreading code. This is, UE_1 applies

$$R_{x1} = \sum T_x c_1 = \sum([0 \quad 2 \quad -2 \quad 0][1 \quad -1 \quad 1 \quad -1]) = -4, \tag{2.5}$$

and UE_2 applies

$$R_{x2} = \sum T_x c_2 = \sum([0 \quad 2 \quad -2 \quad 0][1 \quad 1 \quad -1 \quad -1]) = 4. \tag{2.6}$$

Note that each decoded information has the same polarity as the transmitted one, with the magnitude increased by the code energy (for times greater than the information), which could be normalized. In any case, multiple access has been ensured due to properly orthogonal-based coding. Even though the users have shared the same propagating channel, in the same time-frequency resource, no inter-user interference has been observed. An important feature to be highlighted is: the information of all users is broadcasted to all of them by the BS, but only with the correct code, UE can decode the incoming signal and receive its own information. Without the correct code, no information is received [84].

From this point forward, the OFDMA technique will be discussed. OFDMA consists of taking advantage of multi-carrier modulations for ensuring multiple access [83][85-88]. In DL, subcarriers are divided into RB and distinct ones are allocated to distinct UEs [85]. Figure 2.5(a) illustrates the concept, in which the user *i* complex envelope symbol $s_i(t) = s_{Ii}(t) + js_{Qi}(t)$ is multiplied by the complex exponential $e^{j\pi f_i t}$ and, then, added to create a baseband OFDM signal with multiple users, characterizing a multiple access scheme based on orthogonal subcarriers [83]. The OFDM signal can be up-converted by multiplying by a second complex exponential, $e^{j\pi f_c t}$, in which f_c is the passband signal final center frequency. If subcarrier spacing is an integer multiple of $1/T_{OFDM}$, in which T_{OFDM} is the OFDM symbol duration (or signaling period), it is ensured subcarriers orthogonality and, a minimum spacing of $1/T_{OFDM}$ is often adopted in practice [83]. The illustration considers each user allocating a unique subcarrier for didactic purposes, however, in practice, each user

allocates at least 12 subcarriers, which corresponds to one RB. This classic generation technique considers creating each subcarrier in time.

Classical OFDM generation is not a viable practical implementation, since time-synchronism of multiple RF generators is unfeasible and, due to electronics imprecision, a frequency shift is expected among them throughout time, which would entail in non-orthogonal subcarriers and, consequently, interferences [85][86][88]. Digital signal processing (DSP)-based OFDM generation is commonly ensured by applying an inverse fast Fourier transform (IFFT), as illustrated in Figure 2.5(b), and could be explained as follows: each symbol is represented in the frequency domain as a Fourier coefficient. By applying an IFFT operation, these symbols are mapped into distinct orthogonal-frequency subcarriers, creating an OFDM signal in the time-domain [85][86][88]. If multiple user information is mapped into the same OFDM signal, in distinct subcarriers, an OFDMA scheme is employed. Finally, Figure 2.5(c) represents the frequency-domain and RB representation of an OFDMA system.

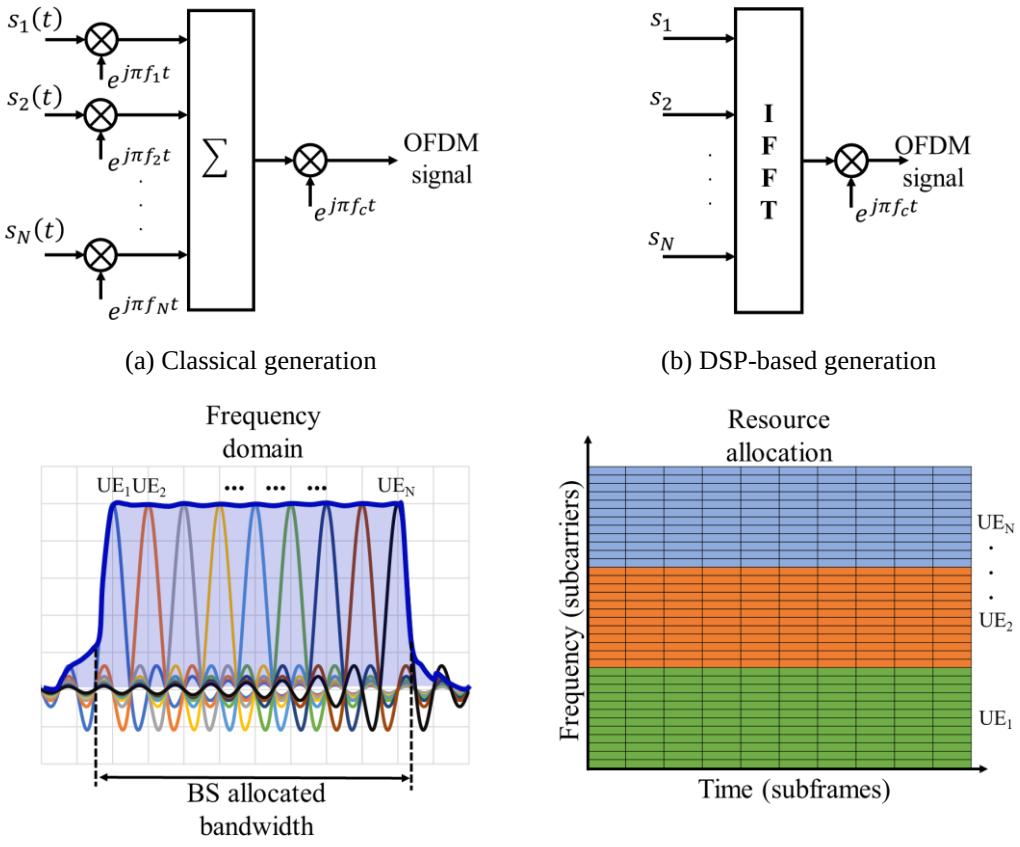

(a) Classical generation

(b) DSP-based generation

(c) Frequency and RB representation

Figure 2.5. DL OFDMA system and representation.

2.1.6. Switched-Beam

5G NR has employed the switched-beam technique in its FR 2 operation [89]. This technique is also commonly named beam selection and beam switching. The technique makes use of a synchronization signal block (SSB), composed of PSS and SSS for cell and beam selection in multiple beam operation mode [89]. The physical broadcast channel (PBCH) symbols carry their own DMRS and make use of QPSK waveform.

Switched-beam is similar to cell search, in which a UE acquires time and frequency synchronization with a cell and detects its Cell ID, using PSS, SSS and PBCH DMRS. In Radio Resource Control (RRC) connection, the UE measures multiple beams (at least one) of a cell and the results (power values) have to be averaged to cell quality estimation. In this way, UE is configured to consider a subset of the detected beams. Filtering takes place at two levels: at the physical layer to acquire beam quality and, then, at RRC level for cell quality estimation throughout multiple beams. Measurement reports may contain the results of the *X* best beams if the UE is configured to do so by the gNB (node providing NR user plane and control plane protocol terminations towards the UE, and connected via the NG interface to the 5G core network) [89].

Figure 2.6 illustrates a switched-beam mode implementation with 12 beams. From the antenna point-of-view, the array has to be able to provide simultaneous multiple beams with high gain and low-coupling among them. Each beam covers a distinct and restricted angle range for increasing gain in that direction and has its own SSB to indicate its identity. UE chooses the best beam as previously explained. The technique is not considered as a MIMO system, but a solution for increasing effective radiated power (EIRP), compensating the high propagation and penetration losses in higher frequencies, such as in FR 2 [45][48][54][59]. MIMO could be employed in each beam by using dual-polarized antennas for diversity and multiplexing gain [54], however, it would not be considered as a mMIMO system. A SS burst is composed of multiple SSBs confined on a 5-ms time-window. A set containing information of all available beams (multiple SS bursts) has a periodicity of two frames (20 ms) [89].

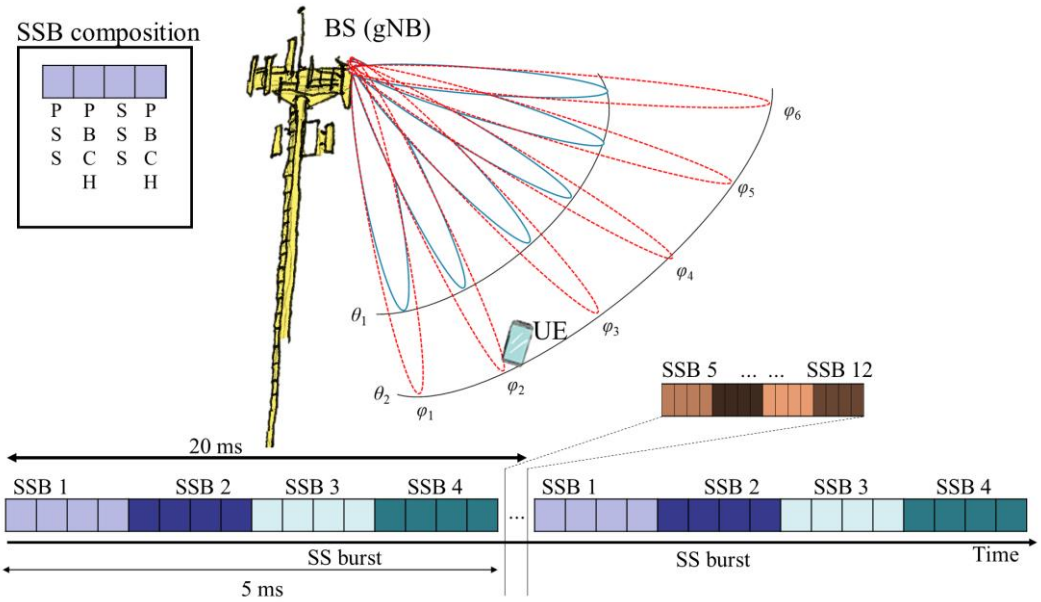

Figure 2.6. Switched-beam mode implementation and synchronization period.

2.2. MIMO for 5G

This Section outlines the mMIMO techniques applied to 5G, including diversity for enhancing SNR on the receiver side, spatial multiplexing for improving spectral efficiency and beamforming for minimizing the high losses introduced by the channel in mm-waves. In each case, it is possible to implement a fully digital system based on TDD due to channel reciprocity between UL and downlink DL, or an FDD-based, typically based on a hybrid approach (analog and digital phase compensation) [73]. The mMIMO uses a large number of radiating elements on the BS side for providing spatial multiplexing in the same time-frequency resource when compared with a unique antenna scheme [73]. Additionally, with a massive number of antennas and a reliable CSI, digital beamforming can reach a high spatial resolution and enable multiple access [90-92].

2.2.1. Channel Representation

Before studying the mMIMO techniques themselves, a brief channel representation should be approached. Figure 2.7 illustrates a general MIMO channel illustration, in which N is the number of transmitter antennas and M the number of receiver antennas. Note NxM channels are created between transmitter and receiver. In this way, the channel can be expressed as an NxM matrix given by [90-95]

$$\mathbf{H} = \begin{bmatrix} h_{00} & h_{01} & h_{02} & \dots & h_{0(N-1)} \\ h_{10} & h_{11} & h_{12} & \dots & h_{1(N-1)} \\ h_{20} & h_{21} & h_{22} & \dots & h_{2(N-1)} \\ \dots & \dots & \dots & \dots & \dots \\ h_{(M-1)0} & h_{(M-1)1} & h_{(M-1)2} & \dots & h_{(M-1)(N-1)} \end{bmatrix}. \quad (2.7)$$

Note that each channel is described by h_{ij}, in which i represents the receiver index and j the transmitter index.

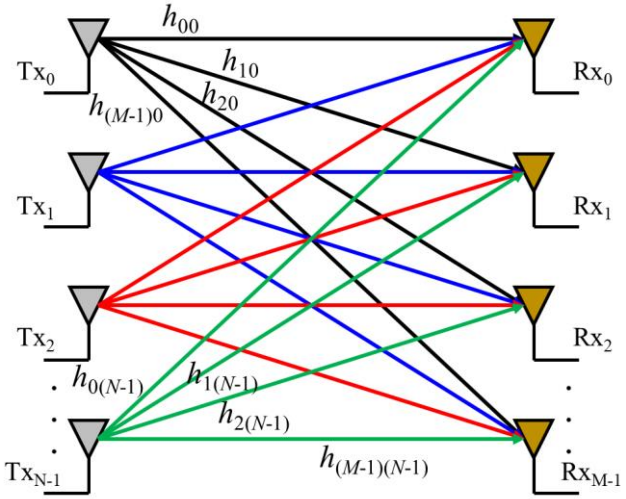

Figure 2.7. Generical MIMO channel representation.

Considering a complex baseband symbol representation ($s = A + jB$) for understanding each channel, h_{ij} itself has a complex response ($h = X + jY$) [83]. If each channel is composed of multiple paths, and the number of samples is large enough so the Central Limit Theorem is respected, one can assume that both X and Y are independent and identically distributed (iid) zero-mean Gaussian variables with the same variance (σ^2) [83][96]. By assuming two i.i.d. Gaussians in a rectangular form, the joint probability density function (PDF) of X and Y is given by

$$\begin{aligned} f_{XY}(x,y) = f_X(x) f_Y(y) &= \frac{1}{\sqrt{2\pi\sigma^2}} e^{\left[-\frac{x^2}{2\sigma^2}\right]} \times \frac{1}{\sqrt{2\pi\sigma^2}} e^{\left[-\frac{y^2}{2\sigma^2}\right]} \\ &= \frac{1}{2\pi\sigma^2} e^{\left[-\frac{x^2+y^2}{2\sigma^2}\right]}. \end{aligned} \quad (2.8)$$

One can apply the following relations for calculating h magnitude and phase PDFs:

$$|h| = R = \sqrt{X^2 + Y^2}, R \geq 0 \text{ and}$$
$$\arg(h) = \Theta = \tan^{-1}\left(\frac{Y}{X}\right), -\pi \leq \Theta \leq \pi, \tag{2.9}$$

from where it is possible to write some further relations

$$X = R\cos\Theta \Rightarrow x = r\cos\theta,$$
$$Y = R\sin\Theta \Rightarrow y = r\sin\theta \text{ and} \tag{2.10}$$
$$R^2 = X^2 + Y^2 \Rightarrow r^2 = x^2 + y^2.$$

Applying the Jacobian for base transformation, we have

$$f_{R\Theta}(r,\theta) = f_{XY}(x,y)|J(r,\theta)|, \tag{2.11}$$

in which the Jacobian is defined by

$$|J(r,\theta)| = \begin{vmatrix} \frac{\partial(x)}{\partial r} & \frac{\partial(x)}{\partial \theta} \\ \frac{\partial(y)}{\partial r} & \frac{\partial(y)}{\partial r} \end{vmatrix} = \begin{vmatrix} \frac{\partial(r\cos\theta)}{\partial r} & \frac{\partial(r\cos\theta)}{\partial \theta} \\ \frac{\partial(r\sin\theta)}{\partial r} & \frac{\partial(r\sin\theta)}{\partial r} \end{vmatrix} = \begin{vmatrix} \cos\theta & -r\sin\theta \\ \sin\theta & r\cos\theta \end{vmatrix} = \tag{2.12}$$
$$r\cos^2(\theta) + r\sin^2(\theta) = r.$$

By applying (2.8) and (2.12) in (2.11), we can reach to the joint PDF of *R* and *Θ*

$$f_{R\Theta}(r,\theta) = \frac{r}{2\pi\sigma^2} e^{\left[-\frac{r^2}{2\sigma^2}\right]},\ r \geq 0 \text{ and } -\pi \leq \theta \leq \pi\,. \tag{2.13}$$

The marginal PDF $f_R(r)$ is given by integrating $f_{R\Theta}(r,\theta)$ in θ, which yields

$$f_R(r) = \int_{-\pi}^{\pi} \frac{r}{2\pi\sigma^2} e^{\left[-\frac{r^2}{2\sigma^2}\right]} d\theta = \frac{r}{2\pi\sigma^2} e^{\left[-\frac{r^2}{2\sigma^2}\right]} \int_{-\pi}^{\pi} d\theta = \frac{r}{\sigma^2} e^{\left[-\frac{r^2}{2\sigma^2}\right]}, r \geq 0. \tag{2.14}$$

From (2.14) one can conclude *R* and *Θ* are also independent random variables, and so

$$f_{R\Theta}(r,\theta) = f_R(r) f_\Theta(\theta) = \frac{r}{\sigma^2} e^{\left[-\frac{r^2}{2\sigma^2}\right]} \times \frac{1}{2\pi} \text{ and}$$
$$f_\Theta(\theta) = \frac{1}{2\pi}, -\pi \leq \theta \leq \pi. \tag{2.15}$$

From (2.14) and (2.15), one can note that a multipath channel, with no predominant path, can be represented by a random variable with magnitude modeled

like a Rayleigh distribution and phase as a uniformly distributed variable from -π to π, which are both represented in Figure 2.8, for distinct values of σ. Note that as σ increases, the higher the channel gain (PDF mean). This concept should help us to properly understand the proposed antenna array test mechanism in Chapter 3.

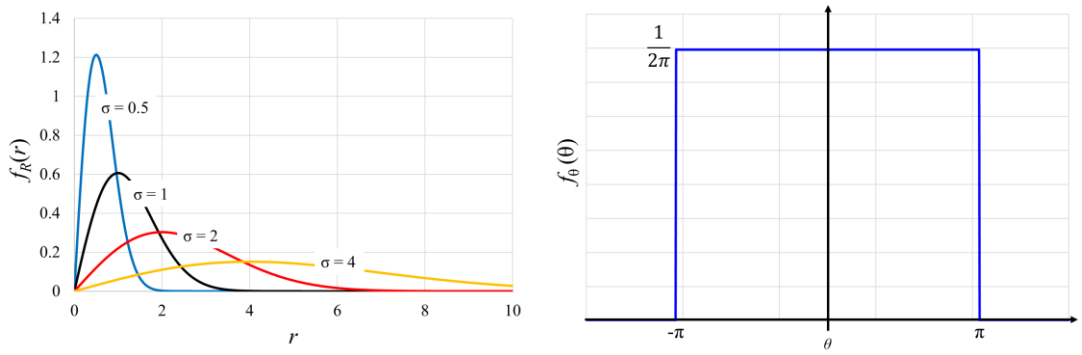

(a) Magnitude (b) Phase

Figure 2.8. Multipath channel PDF in magnitude and phase.

Furthermore, 3GPP Release 15 has proposed a system channel modeling considering a mMIMO application up to 100 GHz [97]. The procedure for modeling a channel response, i. e., each position in the channel matrix from (2.7), is organized into 12 steps as follows: **1 -** Set environment, network layout, and antenna array parameters; **2 -** Assign propagation condition (LOS/NLOS); **3 -** Calculate the log-normal-based pathloss; **4 -** Generate large scale parameters, e.g., shadow fading taking into account cross correlation; **5 -** Generate cluster delays; **6 -** Generate cluster powers; **7 -** Generate angle of departure and angle of arrival for both azimuth (AoD and AoA, repctively) and elevation (ZoD and ZoA, repctively); **8 -** Couple randomly AoD and ZoD angles ($\varphi_{n,m,AoD}$ and $\theta_{n,m,AoD}$) to AoA and ZoA angles ($\varphi_{n,m,AoA}$ and $\theta_{n,m,AoA}$) within a cluster *n*; **9 -** Generate the log-normal-distributed cross polarization power ratios (XPR) *k* for each subpath *m* of each path *n*; **10 -** Draw initial random phases for each subpath *m* of each path *n*; **11 -** Generate channel coefficients for each cluster *n* and each receiver and transmitter element pair *i*, *j*. **12 -** Apply pathloss and shadowing for the channel coefficients.

The n^{th} multipath component of the channel matrix between receiver *i* and transmitter *j* is given by (2.16), in which $F_{rx,i,\theta}$ and $F_{rx,i,\varphi}$ are the *i* antenna receiver radiation pattern in ZoA and AoA of $\hat{\theta}$ and $\hat{\varphi}$, respectively. $F_{tx,j,\theta}$ and $F_{tx,j,\varphi}$ are the *j* antenna transmitter radiation pattern in ZoD and AoD of $\hat{\theta}$ and $\hat{\varphi}$, respectively. $\hat{r}_{rx,n,m}$

is the spherical unit vector with azimuth and elevation angle of arrival $\varphi_{n,m,AoA}$ and $\theta_{n,m,ZoA}$, respectively, in which *n* corresponds to the multipath index and *m* a subpath inside the n^{th} cluster. Cluster is the given name for a set of subpaths with similar statistics features (higher correlation among themselves). $\hat{r}_{tx,n,m}$ is the spherical unit vector with azimuth and elevation angle of departure $\varphi_{n,m,AoD}$ and $\theta_{n,m,ZoD}$, respectively. Furthermore, $\bar{d}_{rx,i}$ and $\bar{d}_{tx,j}$ are the receiver antenna *i* and transmitter antenna *j* location vector, respectively. $k_{n,m}$ is the cross-polarization power ratio on a linear scale. Finally, if a single polarization is considered in the modeling, the 2x2 polarization matrix can be replaced by $e^{(j\Phi_{n,m})}$ and only vertically polarized fields are considered. The Doppler frequency component $v_{n,m}$ is given by (2.17), in which it is possible to observe a high dependence with AoA and ZoA, velocity vector $\bar{v}$ with velocity *v* and azimuth and elevation traveling angle of φ_v and θ_v, respectively [97].

$$
\begin{aligned}
h_{i,j,n}(t) = \sqrt{\frac{P_n}{M}} \sum_{m=1}^{M} \Bigg\{ & \begin{bmatrix} F_{rx,i,\theta}\left(\theta_{n,m,\text{ZoA}}, \varphi_{n,m,\text{AoA}}\right) \\ F_{rx,i,\varphi}\left(\theta_{n,m,\text{ZoA}}, \varphi_{n,m,\text{AoA}}\right) \end{bmatrix}^T \\
& \times \begin{bmatrix} e^{j\Phi_{n,m}^{\theta\theta}} & \sqrt{k_{n,m}^{-1}} e^{j\Phi_{n,m}^{\theta\varphi}} \\ \sqrt{k_{n,m}^{-1}} e^{j\Phi_{n,m}^{\varphi\theta}} & e^{j\Phi_{n,m}^{\varphi\varphi}} \end{bmatrix} \\
& \times \begin{bmatrix} F_{tx,j,\theta}\left(\theta_{n,m,\text{ZoD}}, \varphi_{n,m,\text{AoD}}\right) \\ F_{tx,j,\varphi}\left(\theta_{n,m,\text{ZoD}}, \varphi_{n,m,\text{AoD}}\right) \end{bmatrix} \times e^{\left(j2\pi\lambda^{-1}\left(\hat{r}_{rx,n,m}^T\right)\bar{d}_{rx,i}\right)} \\
& \times e^{\left(j2\pi\lambda^{-1}\left(\hat{r}_{tx,n,m}^T\right)\bar{d}_{tx,j}\right)} \times e^{\left(j2\pi v_{n,m}t\right)} \Bigg\}
\end{aligned}
\tag{2.16}
$$

where

$$
\begin{aligned}
v_{n,m} &= \frac{\hat{r}_{rx,n,m}^T \cdot \bar{v}}{\lambda} \text{ and} \\
\bar{v} &= v \cdot [\sin\theta_v \cos\varphi_v \quad \sin\theta_v \sin\varphi \quad \cos\theta_v]^T.
\end{aligned}
\tag{2.17}
$$

A possible interpretation for (2.16) goes as follows: a constant ponders the summation by the channel gain of each subpath; the transposed vector represents a receiver antenna element radiation pattern in the cluster direction, i.e., considers the AoA and ZoA at UE; the two-by-two matrix is regarding the dual-polarized gain array

feature; the second vector represents a transmitter antenna element radiation pattern in the cluster direction, i.e., considers the AoD and ZoD at BS; the first exponential is related to the phase rotation between cluster *n* and an antenna element *i* at UE; analogously, the second exponential relates the phase rotation between an antenna element *j* at BS and the cluster *n*; finally, the last exponential considers the phase rotation imposed by the Doppler effect, for accounting mobility.

The most important feature to consider when investigating the 3GPP channel model applied to mMIMO applications is that each *n* possible path between transmitter and receiver considers a unique antenna radiation pattern. Implicitly, this means 3GPP assumes coupling among radiating elements as low as possible so it can be disregarded. Furthermore, each radiation pattern is treated as an isolated antenna in the modeling, so it is not expected to create a unique and well-defined beam as in phase-array antennas, since multipath is expected to be explored in this application. Once the channel representation, magnitude, phase and modeling have been properly discussed, one can explore the opportunities from having multiple channels between BS and UE and the system enhancement possibilities in the next Sections.

2.2.2. Diversity

Diversity can be achieved on both transmitter and receiver sides. Basically, it consists of transmitting the same information over low correlated channels, which can be distinguished among them by its frequency, time, or space [93]. Both frequency and time diversity suffer from poor spectral efficiency, which means extra time-frequency resources are used for transmitting redundancy information. On the other hand, spatial diversity can reach diversity gain with the same time-frequency resource by the cost of increasing the number of antennas in the transmission and/or reception [93]. The basic idea is to increase the SNR at the reception, overcoming the fading for ensuring a more reliable communication link.

Diversity at transmission can be achieved by pre-coding schemes, in which the same symbol is transmitted over distinct antennas with some differences, e.g., one antenna transmits the symbol as it is, the second one its conjugated form. This precoding scheme has been firstly introduced by Alamouti in 1998 and is named space-

time block coding (STBC) [94]. Initially, STBC has been conceived for providing diversity gain only for two transmitting antennas and, posteriorly, it has been expanded for *N* transmitting antennas and named as space-time trellis coding (STTC) [98][99]. Both STBC and STTC make use of multiple slots of time for transmitting the same information over distinct antennas [94][98][99].

Diversity at receiver consists of using multiple antennas for receiving the same information, taking advantage of multiple channels. There is a plurality of techniques for properly decoding the multiple replicas at the receiver: pure selection (PS), which selects the information from the antenna with the best SNR; equal gain combining (EGC), which adds all the antennas outputs with the channel phase compensation; maximum ratio combining (MRC), which adds all the antennas outputs with the channel phase and magnitude compensation and yields in the best diversity performance [95][100][101].

For properly decoding transmission diversity and/or combining multiple antenna outputs in reception diversity, the system must be aware of CSI by means of accurate channel estimation. Figure 2.9 exemplifies a simple single-input multiple-output (SIMO) with order two for understanding the concept using the MRC technique. In this scenario, a unique antenna transmits the information (*c*) and two low-coupled and uncorrelated antennas receive two replicas of the same information. Each replica has experienced a distinct multipath wireless channel. Considering an appropriate channel estimation at reception, antenna 0 (Rx_0) multiplies the received information by the channel conjugated response ($\hat{h}_{00}^*$). Analogously, antenna 1 (Rx_1) multiplies by $\hat{h}_{10}^*$. Posterior, both resultant signals can be combined by a simple adding operation [95]. Finally, at the receiver, it is considered a noise addition (*n*).

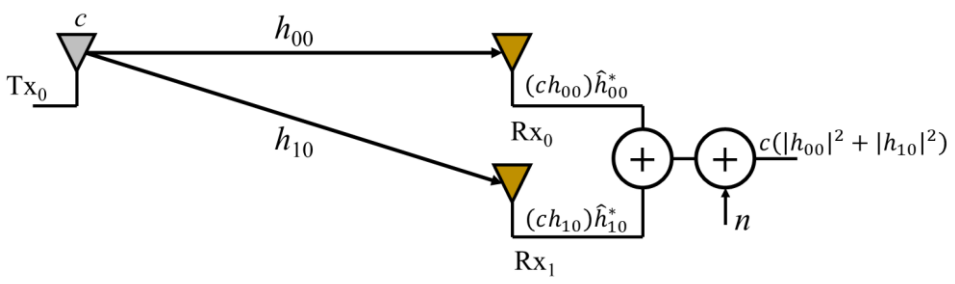

Figure 2.9. Order-two MRC example.

Multiplying by the channel conjugate response is a good strategy since the system can compensate each channel phase rotation for achieving a constructive combination in phase and, in addition, values high-gain channels and devalues low-gain ones. This means high-gain channels would contribute more to the resultant received signal than poor performing ones. Note in the decoded information in Figure 2.9, the symbol is pondered by the two channels magnitude (an average of $10\log(2) = 3$ dB gain) and the phase between Tx and Rx has been eliminated by proper compensation, which means symbols can be combined without performance degradation. Generally, the received signal (S_r) can be expressed as

$$S_r = \mathbf{H}c + n. \tag{2.18}$$

2.2.3. Multiplexing

Spatial multiplexing consists of using multiple antennas for concurrently transmitting more data over distinct propagation channels [102]. The main goal of the technique is to take advantage of multiple non-correlated propagation channels for transmitting distinct data streams and, consequently, enhancing the system total throughput. The concept can be exemplified with a simple system scenario as presented in Figure 2.10. For the multiplexing scheme, at transmission, Tx_0 transmits c_i and Tx_1 transmits c_{i+1}, simultaneously. The received signal can also be expressed by (2.18), however, it will be expanded and presented according to

$$S_{r0} = c_0 h_{00} + c_1 h_{01} + n \tag{2.19}$$

One can note that during one symbol interval, two symbols have been simultaneously received, doubling the system throughput.

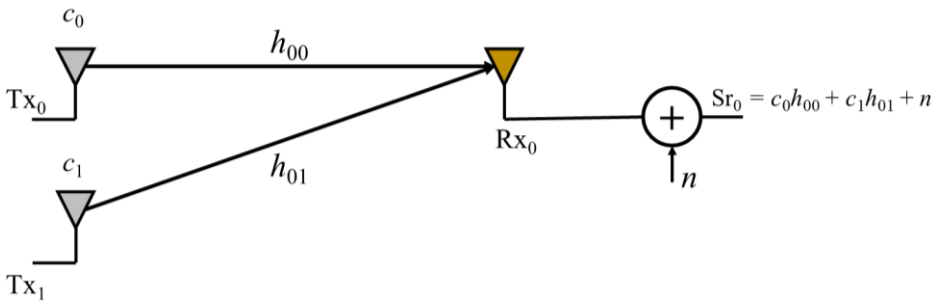

Figure 2.10. Order-two multiplexing scheme.

For properly decoding and estimating the received symbols, the decoder has to be able to estimate the channel matrix **H** and compensating it by using zero-forcing, minimum mean square error (MMSE), or other decoding technique [103]. Zero forcing consists of multiplying the receiver vector S_{ri} by the channel inverse matrix $\mathbf{H}^{-1}$. Zero forcing performs poorly in low SNR scenarios due to noise enhancement introduction [103]. MMSE can mitigate such a problem by applying a more sophisticated matrix to multiply the received signal, aiming to compensate only the channel phase deviation, with no concerns with its gain, which causes noise enhancement. Furthermore, even more sophisticated non-linear-based decoding techniques such as maximum-likelihood and vertical Bell Laboratories layered space (VBLAST) could also provide diversity gain in addition to multiplexing throughput enhancement, since there is more than one channel between Tx and Rx [103].

2.2.4. TDD-Based Digital Massive MIMO

TDD-based digital mMIMO makes use of channel reciprocity for ensuring multipath compensation and enhanced data throughput [73][77][78]. Figure 2.11 illustrates the concept in a didactic manner. At UL (Figure 2.11(a)), multiple UEs can transmit a pilot symbol and/or subcarrier. The pilot information is known by BS, so the observed differences are concerned with multipath channel fading. BS estimates the channel phase response (-α) and properly compensates it (+α) at DL (Figure 2.11(b)), ensuring in this way, all multiple paths are constructively combined at UE.

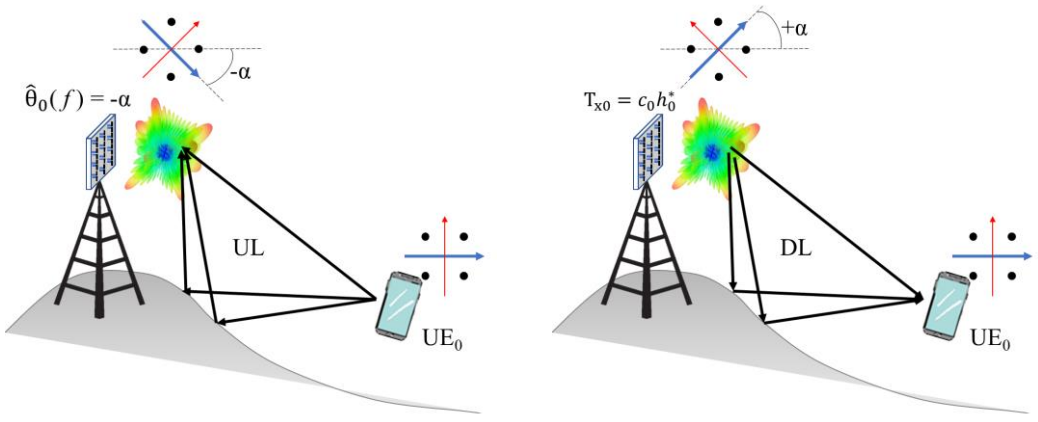

(a) UL (b) DL

Figure 2.11. mMIMO channel reciprocity concept.

No a priori assumptions on the propagation environment and no predetermined beams are needed, but CSI is measured at BS by observing UL pilots transmitted by the UEs. By virtue of TDD operation and reciprocity of propagation, the so-obtained UL CSI is also valid for the DL. The period resultant from at least one UL and DL turn should be smaller than the channel coherence time (T_c) so TDD-based digital mMIMO properly works and channel reciprocity can be considered (reciprocity calibration) [73][77][78]. T_c is defined as the minimum period in which the channel could be considered static [83] and is given by

$$T_c = \sqrt{\frac{9}{16\pi f_d^2}}, \tag{2.20}$$

in which f_d is the Doppler shift, defined as the phase variation with respect to time, which can be seen as an angular frequency variation experienced by a moving UE with velocity (v) [83]. The Doppler shift is given by

$$f_D = \frac{v}{\lambda}\cos\varphi, \tag{2.21}$$

and φ is the angle between BS and UE [83], as illustrated in Figure 2.12.

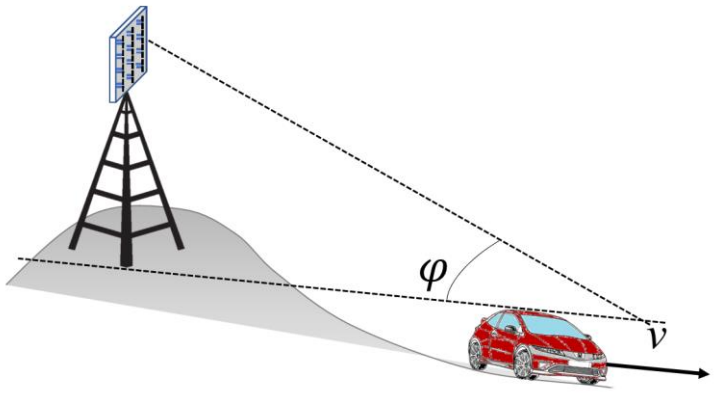

Figure 2.12. Doppler shift calculation scenario.

The main advantage of using the TDD technique is that by pre-compensating each channel, multiple paths will constructively combine in phase at a unique location [73]. Spatial resolution is enhanced by increasing the number of antennas and, consequently, number of channels [69-73]. Multiple access is also ensured in TDD-based digital mMIMO as exampled in Figure 2.13, in which the data from user 0 ($\vec{C}$)

only combines constructively at his equipment and the data from user 1 ($\vec{D}$) will not interfere with it due to the large number law [96], which establishes the distinct channels should tend to be orthogonal among themselves as the number of paths increases. At the location of user 1, the opposite occurs. One can compare the multiple access scheme with the CDMA technique, but in this case, the orthogonal code used for each user is its own channel response and, instead of UE has the knowledge for decoding, the DL channel itself is the correct decoding key. It is worth highlighting the most challenging feature is to implement an accurate precoder to properly compensate the channel with a fast response time [102]. Furthermore, spectral efficiency is massively enhanced by multiplexing information in space throughout the antenna elements, which should substantially increase data traffic by transmitting a massive number of symbols at the same time-frequency resource [101-103].

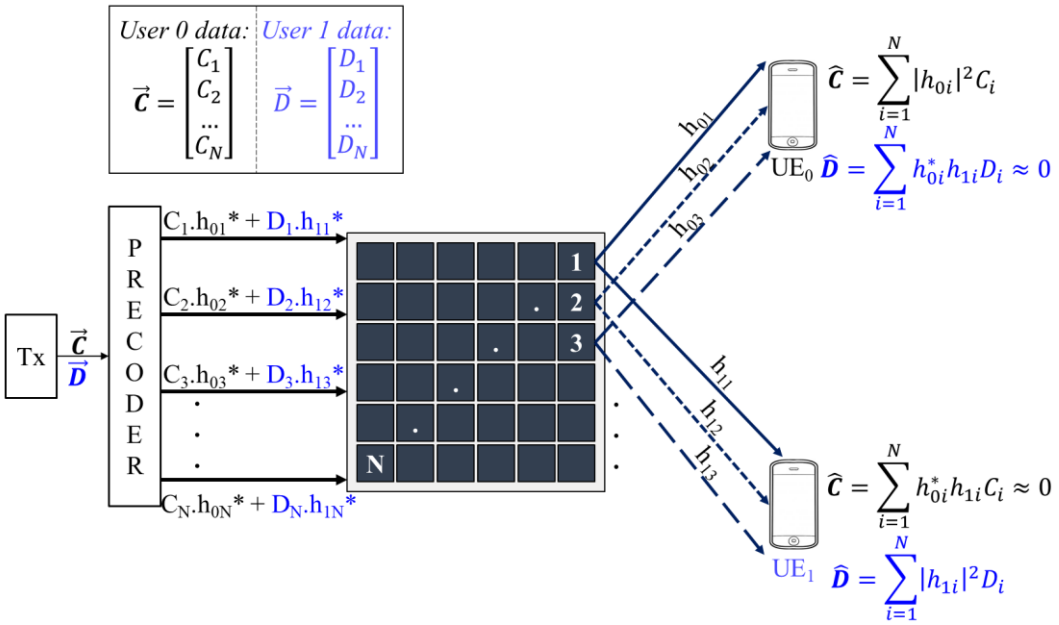

Figure 2.13. TDD-based mMIMO block diagram with multiplexing and multiple access feasibilities.

Chapter 3

3. SICL-SAA: A novel SICL-based Slot Antenna Array for TDD 5G mMIMO Systems

This Chapter aims to present the research deliverables. We shall present the applied techniques for designing the proposed antenna array, its feeding networks and array topology considerations. Posterior, numerical results should be presented and performance analysis carried out for applicability discussions.

The antenna aimed at TDD-based digital mMIMO applications has been designed considering printed techniques for easier massive antenna implementation and integration with RF front-ends [104-107]. Firstly, the feeding network has been taken into consideration due to its complexity and most challenging feature of low-coupling among distinct feeding lines [50-56]. Posteriorly, a slot antenna is proposed and coupling among elements on a dual-polarized array is investigated. Finally, a novel performance metric is proposed, in which the array resultant radiation pattern is analyzed considering the channel propagating environment. The antenna will be named SICL-SAA, which stands for SICL-fed slot antenna array.

3.1. SICL-based Antenna Array Excitation

Four feeding lines techniques have been considered in this research and illustrated in Figure 3.1: classical microstrip line [105-107]; gap waveguide [108-110]; substrate integrated waveguide (SIW) [111-114]; substrate integrated coaxial line (SICL) [115-119]. Figure 3.1(a) presents a classical microstrip line, which consists of an electrical conductor placed above a ground plane, isolated by a dielectric [105-107][120]. If an electrostatic case applies, an image of the upper conductor will

exist in the ground plane in the presence of an electric field, creating a parallel-like transmission line. The main advantage compared to parallel lines is regarding the symmetry, in which any imperfection in the microstrip will also be reflected in the imaginary image [105]. Microstrip operates in transverse electromagnetic mode (TEM), on an extremely wide bandwidth, which facilitates system integration and coaxial line transitions. Furthermore, it is easily manufacturable with a low-cost process. Their disadvantages highlight themselves when mm-waves mMIMO is taken into consideration, since microstrip lines dimensions are frequency-independent, which makes them large structures at high frequencies. Besides, this type of transmission line has no electromagnetic shielding and, coupling among multiple microstrips is extremely high, mainly due to the fringing effect. Finally, substrate loss tangent has to be considered in the antenna array design and, low-loss substrates at mm-waves are expensive, however, this feature is concerning most printed techniques [104-107][120].

Gap waveguides are structures based on metasurfaces [108-110], as illustrated in Figure 3.1(b). The operational principle is to create a perfect electrical conductor (PEC) to guide the electromagnetic wave and surround it with periodic structures which creates a metasurface-based perfect magnetic conductor (PMC), shielding the fields [109]. In printed implementations, typically a three-layer scheme is employed: the first layer is a ground plane; the second layer is a microstrip (PEC); the third layer is a metallic plate for coupling with the PEC component. Multiple metallic vias, connecting only from the first to second layer, are placed surrounding the PEC on a periodic distribution for creating the PMC component. The electromagnetic field is guided between second and third layers, above the PEC path [109]. The implementation can be done with a substrate for keeping isolation between first and second layers, but the metallic plate (third layer) can be suspended by holders, keeping isolation between second and third layers by air, which drastically reduces propagation losses and loss tangent becomes negligible [108-110]. Low coupling among multiple PEC paths is ensured by the high-shielding effect of PMCs surfaces. Their main disadvantages are regarding implementation complexity and cost and, the propagation mode is the transverse magnetic (TM) and highly frequency-dependent due to the PMC periodicity [108-110].

Figure 3.1(c) shows a SIW topology. A substrate with ground planes on both sides and two metallics via rolls for creating a waveguide. A TE mode is ensured by properly exciting the SIW and the electromagnetic wave propagates throughout the substrate [111-114]. This topology presents low coupling among multiple SIW embedded in the same substrate, low implementation costs and complexity, however, their dimensions are considerable for operating in high frequencies and on a mMIMO system, feeding a massive number of isolated radiating elements could be an issue due to lack of spacing.

Finally, SICL transmission line is exampled in Figure 3.1(d). It consists of a microstrip line, shielded by two ground planes (below and above) and two rolls of metallic vias in its both sides, creating a coaxial line integrated on a substrate [115-119]. It is needed two-layer substrate implementation for ensuring shielding in all directions and, consequently, an extremely low coupling feature is achieved [115-119]. The impedance is reduced due to the metallic connection of both ground planes through the metallic rolls, which enables reduced microstrip line width, reducing occupied spacing [115]. SICL operates in TEM mode and has a relatively low implementation cost [115]. Their main disadvantage is the need for two substrates, which increases fabrication process complexity and cost and the dielectric-depended loss due to loss tangent [115-119].

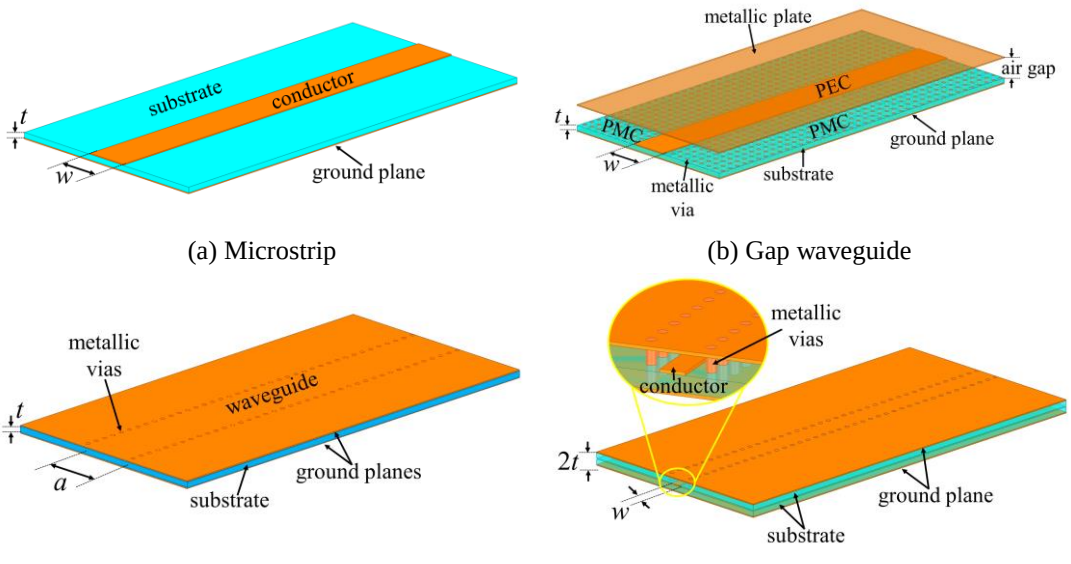

(a) Microstrip (b) Gap waveguide

(c) SIW (d) SICL

Figure 3.1. Potential transmission line techniques.

After pondering all the pros and cons of each transmission line, we have further investigated the SICL technique for the array feeding network design. A classical microstrip line has also been numerically evaluated for comparison purposes. SICL has been firstly introduced by Gatti *et al.* [115] in 2006 and then proposed for a plurality of applications such as balun design [116], feeding network with coplanar waveguide transition [117], feeding network with coaxial line transition [118] and direct antenna feeding [119]. SICL has a wide bandwidth and operates exclusively in TEM mode up to the upper mode, TE, cut-off frequency defined by

$$f_{\mathrm{TE10}} = \frac{c}{2\sqrt{e_r}}\left(A - \frac{D^2}{0.95S}\right)^{-1}, \tag{3.1}$$

in which c is the light speed in vacuum (3×10^8 m/s), ε_r is the dielectric relative electric permittivity and A, D and S are the distance between the vias rolls, via diameter and spacing, respectively [115]. Dimensions are shown in Figure 3.2.

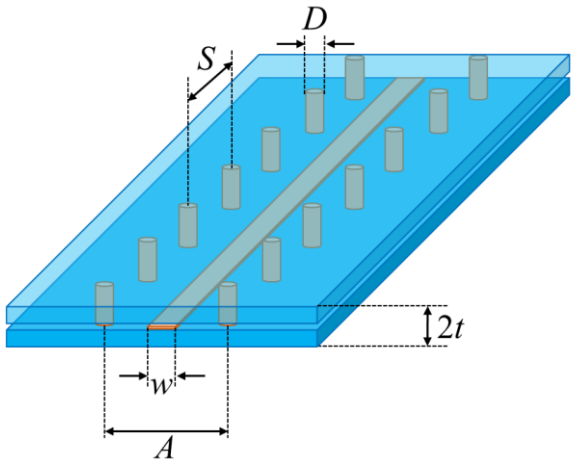

Figure 3.2. SICL main dimensions.

The central conductor width (w) is a parameter that should be optimized for reaching the desired impedance (Z), depending on predefined A, D, S, t and e_r values. Similar to conventional coaxial lines, Z can be managed by playing with the ratio between the structure height ($2t$) and w [115]. At high frequencies operation, a recommended design process goes as follows: ***i)*** select the dielectric type and thickness (t); ***ii)*** choose a manufacturable value of D; ***iii)*** choose a manufacturable value of S; ***iv)*** calculate A applying (3.1) and considering f_{TE10} higher than the design operating upper frequency; ***v)*** tune w for reaching the desired impedance value [115].

The SICL numerical tests have been firstly conducted considering the TE_{10} cut-off frequency at 48 GHz and Rogers CuClad 233 substrate, with ε_r = 2.33 and t = 0.25 mm (total model thickness of $2t$ = 0.5 mm). We have chosen 48 GHz as an initial value for ensuring TEM propagating mode and reduce the A dimension, reducing footprint. Other values could also be implemented and provide good frequency response at 26 GHz as well. Both S and D dimensions have been set with manufacturable values of 1.25 and 0.75 mm, respectively, giving rise to A = 2.5 mm. Moreover, a microstrip line has also been designed for comparison purposes with the same input parameters, but t = 0.5 mm, for ensuring the same substrate influence in both analyses. The microstrip width (w) has been defined according to the empirical formulation [120]

$$u = \frac{Z_0\sqrt{(\varepsilon_r+1)}}{120} + \frac{1}{2}\left(\frac{\varepsilon_r-1}{\varepsilon_r+1}\right)\left[\ln\left(\frac{\pi}{2}\right) + \frac{1}{\varepsilon_r}\ln\left(\frac{4}{\pi}\right)\right] \text{ and}$$
$$w = \frac{t}{\frac{e^u}{8} - \frac{1}{4e^u}}, \tag{3.2}$$

giving rise to w = 1.5 mm.

Figure 3.3 presents the SICL impedance numerical results in both real and imaginary portions. It has been noticed that for w = 0.4 mm, real impedance is closer to 50 Ω and imaginary is as minimum as possible (peak at 40 Ω), even though a high variation is still observed. Furthermore, Figure 3.4 presents the SICL magnitude reflection (S_{11}) and transmission (S_{21}) coefficients, considering a 10λ length transmission line, with λ been the free-space wavelength at 26 GHz. The SICL is well matched in the entire bandwidth, with S_{11} lower than -10 dB from 25 to 27 GHz and S_{21} of approximately -2 dB in the analyzed bandwidth.

It is important to highlight the real ($\Re$) and imaginary ($\Im$) portions of the impedance have been plotted by using the S-parameters according to [104]

$$\Re(Z) = \frac{50\left(1+\Re(S_{11})\right)}{1-\Re(S_{11})} \text{ and}$$
$$\Im(Z) = \frac{50\left(1+\Im(S_{11})\right)}{1-\Im(S_{11})} - 50, \tag{3.3}$$

since a lumped port has been used in the numerical model. The lumped port has a fixed impedance (50 Ω in our design) and HFSS plots only the port real and imaginary parts. The lumped port defines a current between two conductors (positive and negative) and it is more appropriate for excitation of transmission lines.

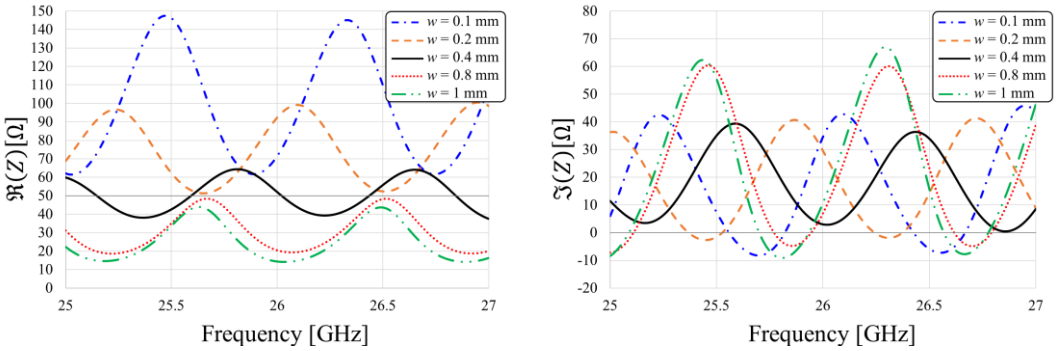

(a) Impedance real part (b) Impedance imaginary part

Figure 3.3. SICL impedance tuning by means of *w* variation.

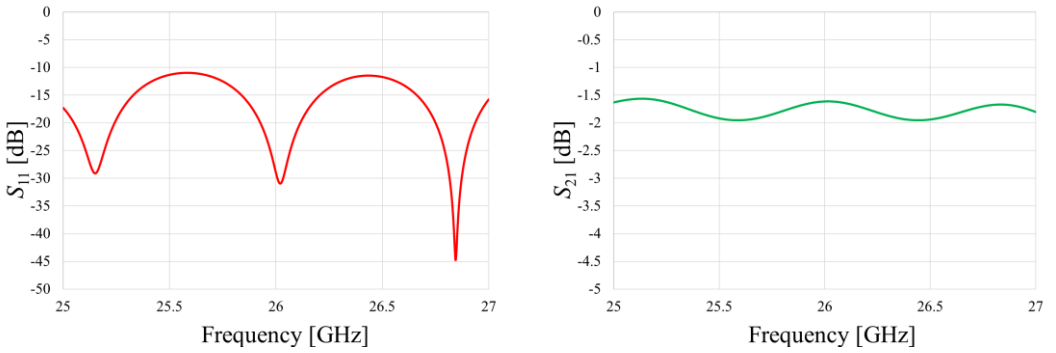

(a) S_{11} (b) S_{21}

Figure 3.4. SICL *S*-parameters numerical results for w = 0.4 mm.

The SICL transmission line has not provided a perfect matched response, in which it would cause no performance influence in the attached radiating element since high impedance variation has been observed. This high variation level in the imaginary part is mainly due to the *t*, *D* and *S* values, in which we have used standard commercial and manufacturable ones. For this high frequency, lower values for these parameters are required. However, the achieved frequency response do not invalidates our proposal, but a joint optimizations should be done posteriorly, i.e., SICL feeding line and radiating element, since they will interfere each other.However, a maximum -10 dB S_{11} is enough for a joint feeding line/antenna design, i.e., the radiating element could be designed for properly operating considering the SICL

impedance variation. Further investigation has been carried out for understanding such feature and the substrate thickness (t) is the main constraint, in which for proper tuning, t should also be managed, but is a fixed dimension and should be carefully chosen according to manufacturer availability and design requirements [115].

Furthermore, Figure 3.5 presents the classical microstrip line numerical results in terms of impedance and S-parameters. The theoretical design has provided values close to $Z_0 = 50 + j0\ \Omega$ from 25 to 27 GHz, with variations of only 2 Ω (Figures 3.5(a) and (b)), S_{11} lower than -30 dB (Figure 3.5(c)) and S_{21} of approximately 1.5 dB (Figure 3.5(d)) throughout the bandwidth.

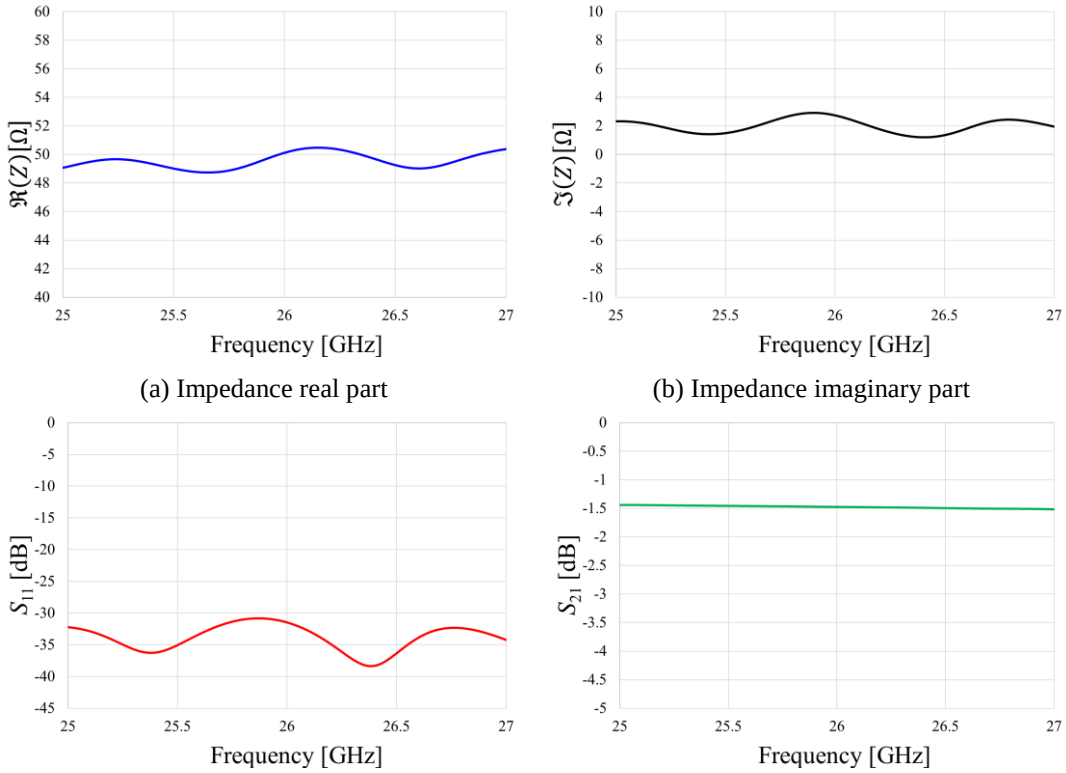

(a) Impedance real part (b) Impedance imaginary part

(c) S_{11} (d) S_{21}

Figure 3.5. Classical microstrip line numerical results.

Posterior, we have placed two microstrip lines side-by-side, also with a 10λ length and varied the distance between them (d) for observing the mutual coupling from port 1 to 4 as illustrated in Figure 3.6. Furthermore, SICL transmission lines have also been placed side-by-side at the minimum possible d value due to mechanical constraints. The minimum value of d on a SICL topology is A itself (from Figure 3.2),

in which two central conductors will share the same metallic vias roll, isolating them. The coupling numerical setup between two parallel SICL is illustrated in Figure 3.7 and has been conducted considering d = A = 2.5 mm.

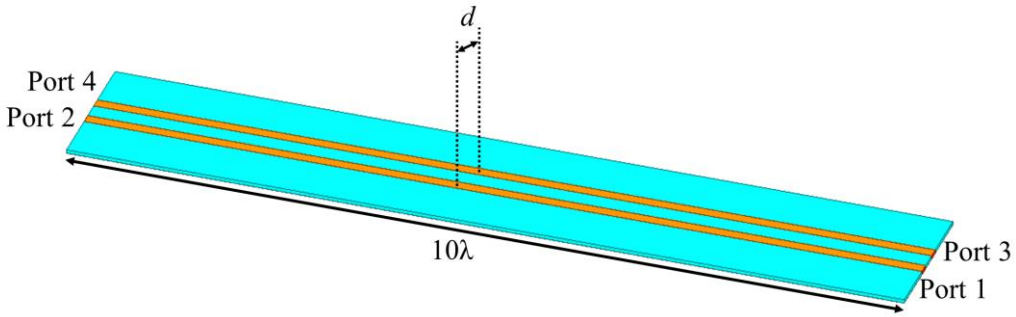

Figure 3.6. Numerical model for the microstrip line coupling analysis.

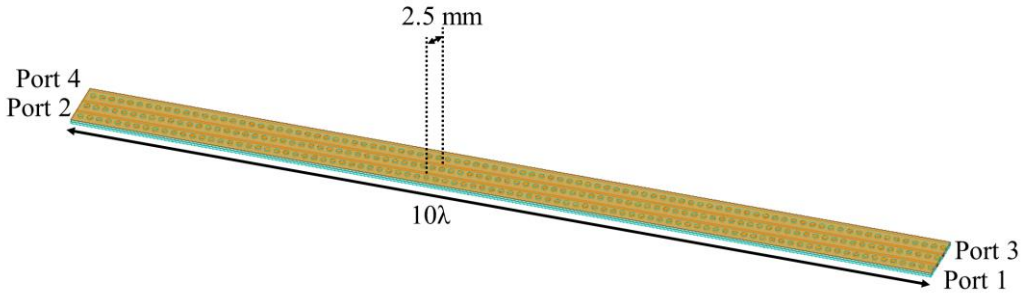

Figure 3.7. Numerical model for the SICL coupling analysis.

Figure 3.8 presents the coupling results comparing Figures 3.6 and 3.7 numerical designs as a function of *d*. For the SICL case, we have evaluated only one *d* value, *d* = 2.5 mm, which is the lower possible value, i.e., two SICL sharing one shielding wall. Let us highlight two important marks: *d* = 5.2 mm; *d* = 2.5 mm. Note the microstrip line has provided low-coupling (lower than -20 dB) only for *d* values larger than 5.2 mm. This would entail severe implementation constraints on a massive scale antenna array due to high coupling and the need for a large footprint in the feeding network, since not only *d* must be greater, but *w* is three-time larger in the microstrip compared to SICL. On the other hand, SICL in its minimum possible spacing (*d* = 2.5 mm), has proved itself with an extremely high shielding feature, with only -39.7 dB coupling between ports 1 and 4, with reduced footprint, against -5.85 dB coupling in the microstrip at the same *d* value. Figure 3.9 reinforces the conclusion by presenting the simulated electric field in each of the transmission lines for *d* = 2.5 mm. Figure 3.9(a) is regarding the microstrip line, in which the electromagnetic wave

becomes almost a common mode encompassing both conductors, resulting in high coupling between them. Figure 3.9(b) presents the electric field on the SICL transmission line and both propagating modes, one at each conductor, are clearly distinguished between themselves, ratifying the low-coupling feature due to high-effectiveness shielding.

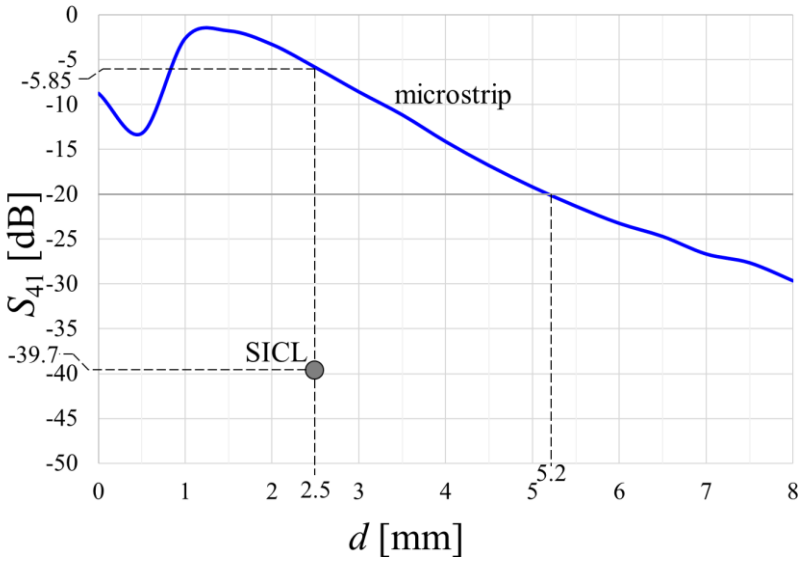

Figure 3.8. Microstrip and SICL coupling numerical results as a function of *d*.

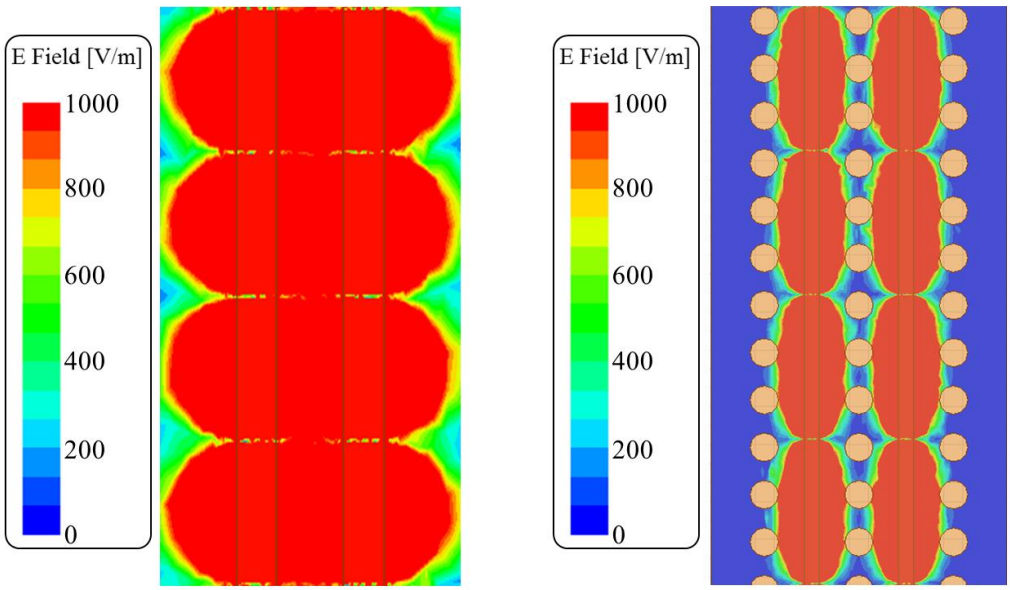

(a) Microstrip (b) SICL

Figure 3.9. Electric field numerical results for coupling analysis with d = 2.5 mm.

3.2. Antenna Array Element Design

The designed radiating element is a resonant slot-based antenna. We have chosen the slot technique due to implementation and integration with printed circuits simplicity, high gain and well-oriented polarization feature. On a base station implementation, the slot should have a reflector for boresight radiation and increased gain. A slot is a hole on the metallic ground plane for interrupting the current flow and enabling radiation [121]. Our research group has already published a plurality of papers on slot-based antennas [57-60][62][63] and this background has also been taken into consideration for the chosen technology in this research.

The primary antenna requirements were as follows: minimum 400-MHz bandwidth centered at 26 GHz; minimum gain of 6 dBi; 3-dB beamwidth of approximately 60° in both planes. Figure 3.10 presents a 26-GHz half-wavelength slot, 45° polarized and excited with a conventional microstrip line. Figure 3.10(a) is regarding the numerical model: two substrate laminates have been used in the design (Rogers Arlon CuClad 233, with $\varepsilon_r = 2.33$ and $\tan\delta = 0.0013$). The slot has been numerically evaluated and its length and width have been set as $L_s = 10$ mm and $W_s = 2.1$ mm, respectively. Between both substrates, the microstrip line excites the slot and, below the structure, a ground plane acts as a reflector. The long slot length is regarding an electric interaction with the large microstrip line (w = 1.5 mm). Figure 3.10(b) presents its radiation pattern and Figure 3.10(c) the element S_{11} response as a function of L_s. The preliminary antenna element has provided a bandwidth from 25.6 to 26.25 GHz, considering S_{11} < -10 dB and gain of 9.1 dBi at 26 GHz. The antenna beamwidth in both planes was approximately 50°.

Posteriorly, the feeding line has been changed to the SICL technique for ensuring low coupling among multiple feeding lines. The numerical design is presented in Figure 3.11(a). The same substrate has been considered (t = 0.25 mm). As previously exposed, both S and D dimensions have been set with manufacturable values of 1.25 and 0.75 mm, respectively, giving rise to A = 2.5 mm and w = 0.4 mm. New numerical evaluations have been performed for operation at 26 GHz. The updated dimensions were as follows: W_s = 2 mm; L_s = 9.4 mm.

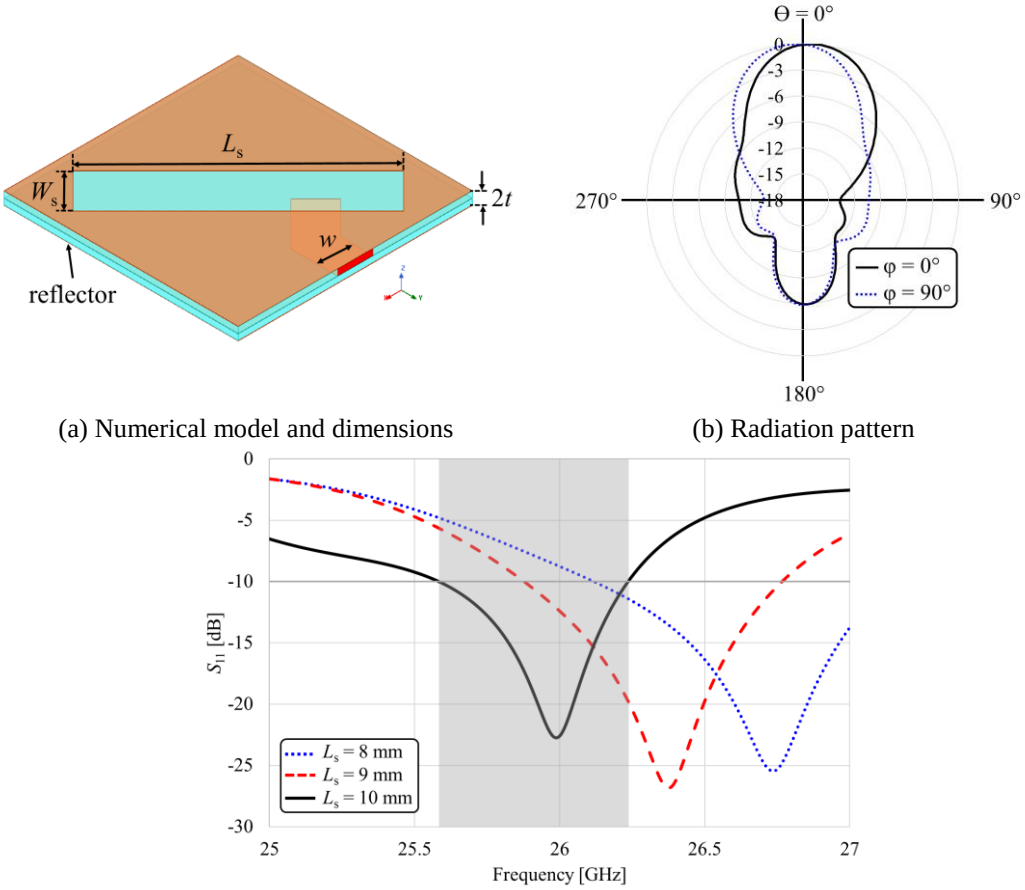

(a) Numerical model and dimensions (b) Radiation pattern

(c) Reflection coefficient as a function of L_s

Figure 3.10. Microstrip-fed slot antenna element numerical design and results.

Figure 3.11(b) presents the element radiation pattern in the *xz*- (φ = 0°) and *yz*-planes (φ = 90°). The slot has provided 7.8-dBi gain with 73° and 52° beamwidth for φ = 0° and φ = 90°, respectively. Furthermore, Figure 3.11(c) presents the element S_{11}, in which a -10 dB impedance matching is ensured from 25.73 to 26.34 GHz, i.e, 610-MHz bandwidth centered at 26 GHz (2.34%). Further investigation has been made in this numerical design, for analyzing the element performance into an array topology. Figure 3.12(a) presents an electric field simulation and it is clear the SICL shielding effectiveness, however, as the electromagnetic wave excites the slot, the energy is not only propagating to free-space, but also throughout the substrate laminates. This indicates the slots themselves must be shielded for mitigating coupling among radiating elements on an array implementation. Figure 3.12(b) proves this phenomenon with two antenna elements placed side-by-side and, only antenna 1 is active. It is possible to see the electromagnetic wave propagating all the way to port 2 (dotted line), increasing coupling prohibitively. Figure 3.12(c) presents the two-

element array *S*-parameters, with a highly degraded and asymmetric impedance matching (S_{11} and S_{22} lower than -10 dB from 26.47 to 26.62 GHz and from 26.11 to 26.78 GHz, respectively) and coupling as high as -9.5 dB in the analyzed bandwidth.

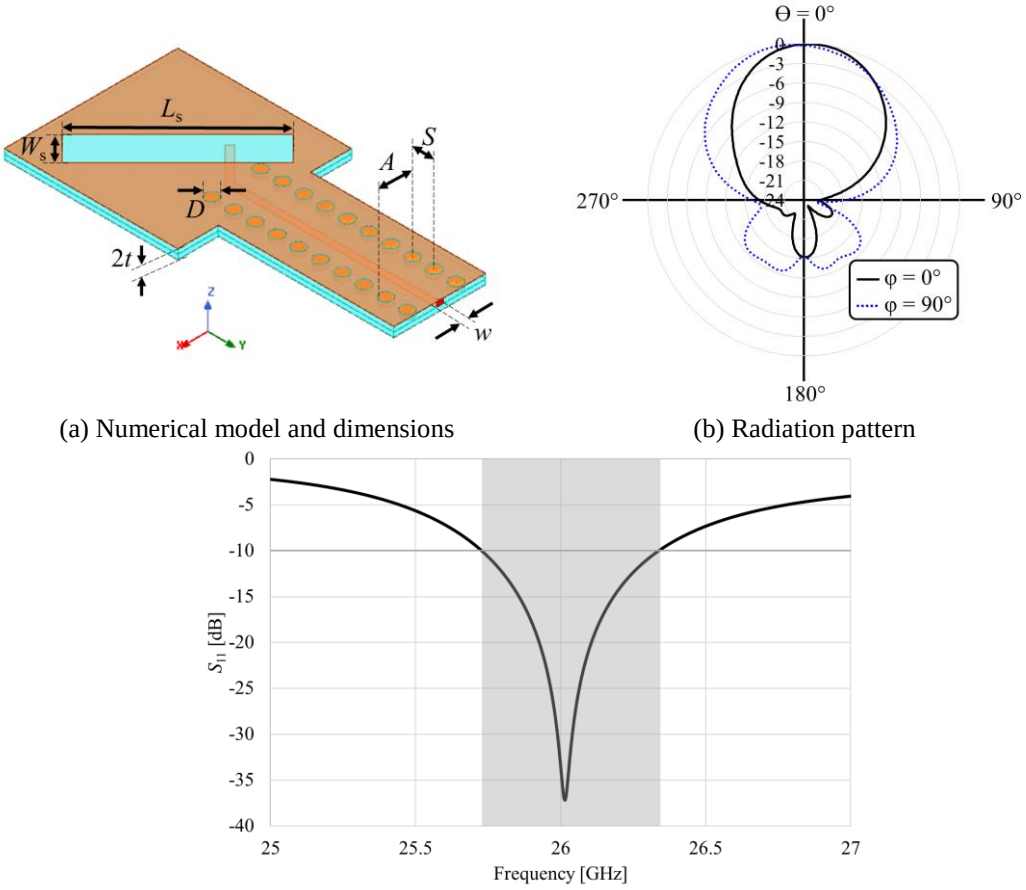

(a) Numerical model and dimensions (b) Radiation pattern

(c) S_{11}

Figure 3.11. SICL-fed slot antenna element numerical design and results.

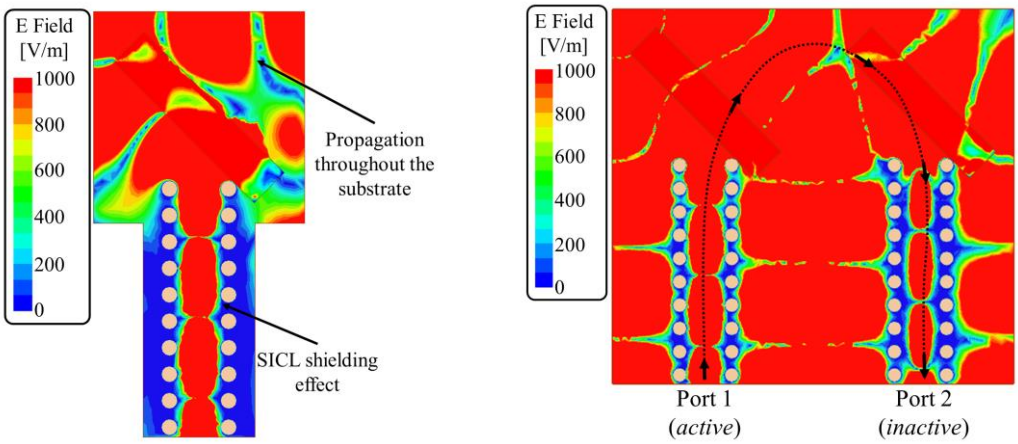

(a) Electric field of one element (b) Two-elements array electric field

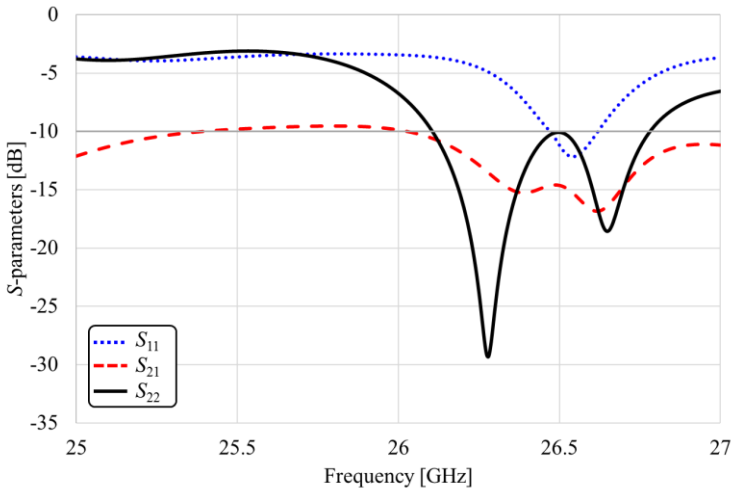

(c) Two-elements array *S*-parameters

Figure 3.12. SICL-fed slot antenna preliminary coupling analysis.

To overcome the high-coupling slot phenomena, metallic vias have been implemented for creating a cavity around each slot. Figure 3.13(a) presents the numerical design. The vias have been placed with the same diameter (D = 0.75 mm) and spacing (S = 1.25 mm) of the designed SICL feeding line. Each cavity has been set with a 10 by 10 mm dimension, creating approximately $\lambda/2$ at 26 GHz spacing from the slot center to cavity border ($G \approx 5.8$ mm). Figure 3.13(b) shows the electric field, in which the electromagnetic wave is now confined inside the cavity and should not couple with other resonating slots.

A new issue is presented, which is the electric field distribution inside the cavity presented in Figure 3.13(b), with a null in the slot center due to multiple reflections inside of it. This feature entails poor radiation pattern performance and impedance matching, as presented in Figure 3.14(a) and Figure 3.14(b), respectively.

The used approach for manipulating the electric field distribution within the cavity is presented in Figure 3.15 and goes as follows: ***i)*** open an aperture in the bottom ground plane with the same cavity size; ***ii)*** create a metallic cavity for managing its height (h_{cav}) and controlling the electric field distribution due to multiple reflections; ***iii)*** install the metallic cavity below the substrate, aligned with the created square hole in the bottom ground plane.

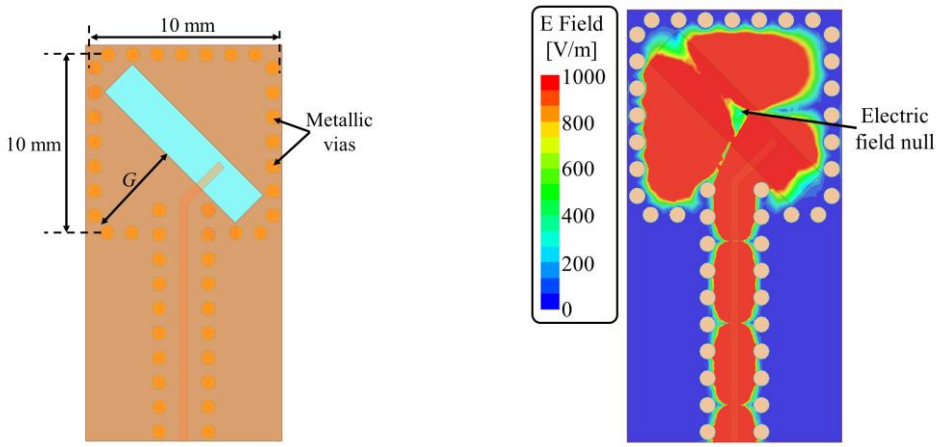

(a) Numerical design and dimensions (b) Electric field

Figure 3.13. SICL-fed slot antenna element within a cavity for mutual coupling reduction.

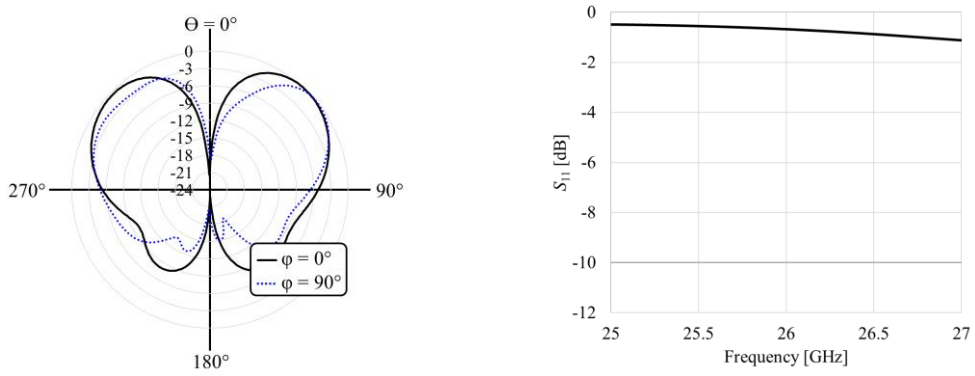

(a) Radiation Pattern (b) S_{11}

Figure 3.14. Numerical results of the SICL-fed slot antenna element within a cavity.

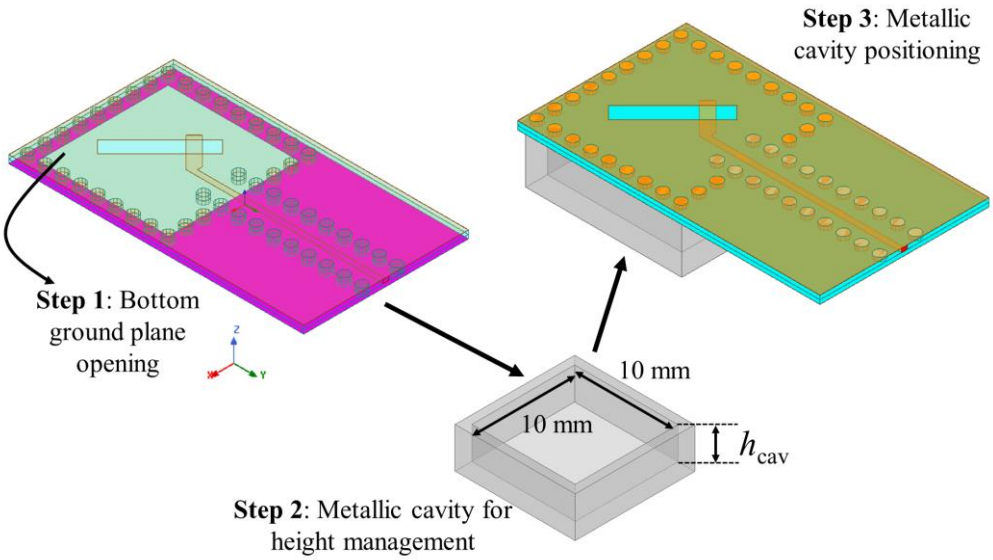

Figure 3.15. Three-dimensional cavity design.

Furthermore, new parameters have been evaluated to properly tune the antenna in the desired frequency band. By varying the feeding strip line width (w_f), length (l_f) and height (h_f) just below the slot, it is possible to properly tune the antenna impedance and electric field distribution in the slot itself. Figure 3.16 present the parameters definitions. Note that by managing h_f, the feeding positioning is being changed in the slot, which is related to the slot excitation and impedance. We have used the x dimension auxiliary variable, note that as h_f increases, x decreases ($x_1>x_2>x_3>x_4$). By managing l_f and w_f, a matching component is created and it is possible to manipulate the line impedance. It is important to highlight those parameters have to be jointly adjusted since by manipulating one of them, the other will be directly affected.

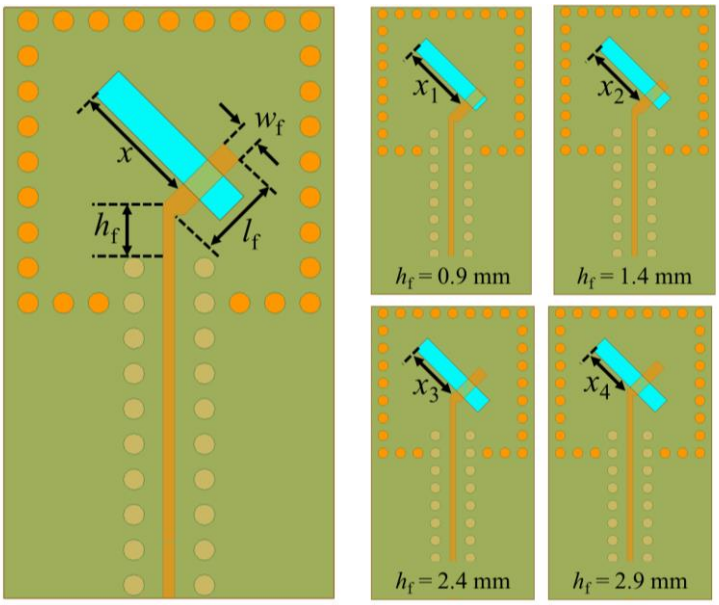

Figure 3.16. Feeding line additional matching parameters.

Figure 3.17 presents the electric field distribution considering h_{cav} = 2.88 mm, which corresponds to exactly $\lambda/4$ at 26 GHz. This has been made so the cavity could be treated as a conventional reflector, in which the reflected wave could be phase-matched with the transmitted wave in far-field [104]. It is possible to observe a well-behaved electric field distribution throughout the slot and, the desired shielding is still effective, which entails low mutual coupling among multiple slots.

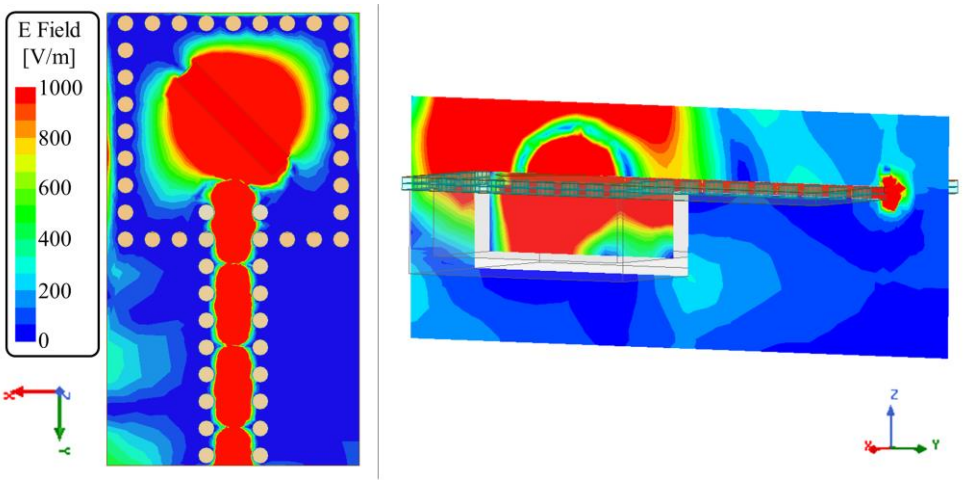

Figure 3.17. Electric field of the SICL-fed slot element with h_{cav} = 2.88 mm.

Figure 3.18(a) presents the S_{11} magnitude results for distinct values of h_f, Figure 3.18(b) and Figure 3.18(c) present the S_{11} smith chart for distinct values of l_f and w_s, respectively. It is possible to observe all the parameters have an important influence on the antenna impedance matching. Particularly, h_f is related to the antenna resonance, which increases with higher values of h_f due to x reduction and, consequently, the slot electric length reduction as well. The parameter l_f mostly controls the structure inductance, which increases with l_f values (curves tend to the upper part of the Smith Chart). Finally, w_f presents a majority influence in the antenna real portion of the impedance. The antenna impedance increases for higher values of w_f due to the increased coupling with the slot right side as the parameter increases (curves tend to the right part of the Smith Chart). With these three parameters, it is possible to manage both real and imaginary parts of the structure's impedance.

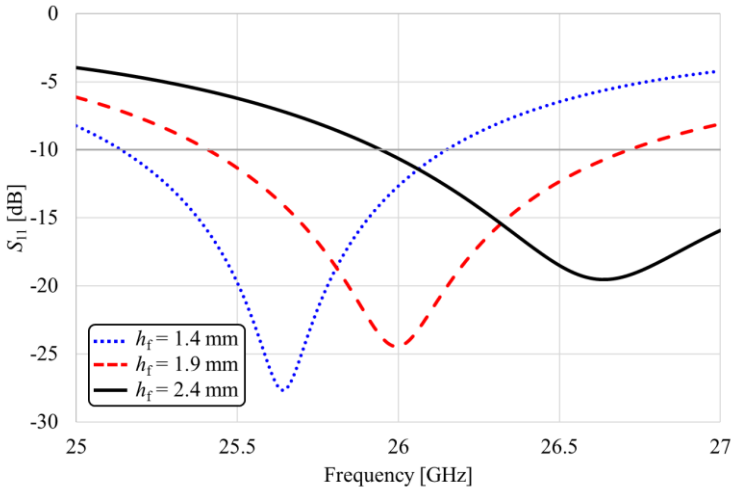

(a) S_{11} magnitude as a function of h_f

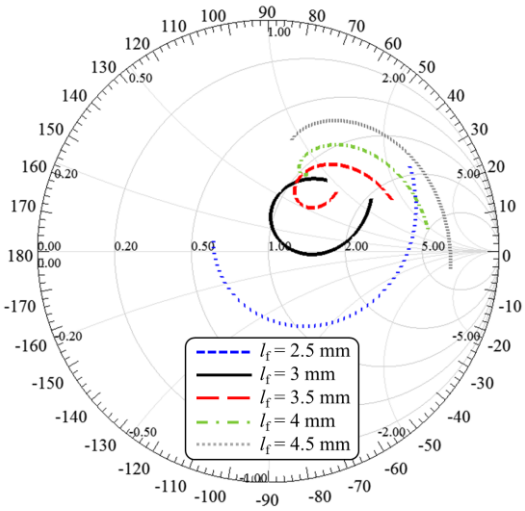

(b) S_{11} Smith Chart as a function of l_f

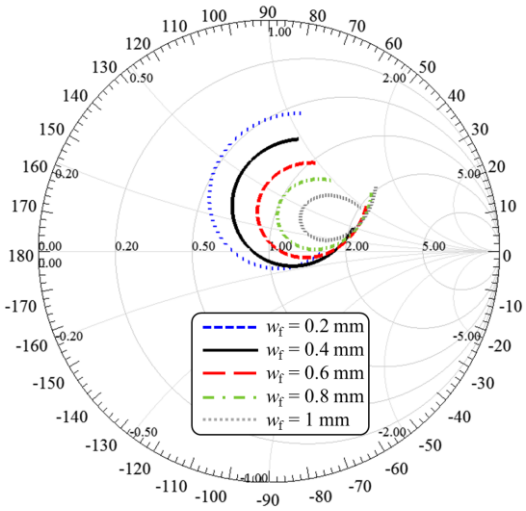

(c) S_{11} Smith Chart as a function of w_f

Figure 3.18. Antenna element numerical analysis as a function of matching parameters variation.

Furthermore, the slot itself could be re-tuned so the interaction between feeding line and slot could be managed and, in this way, it is possible to approximate the slot length with the theoretical value of $L_s = \lambda/2 = 5.77$ mm (at 26 GHz). By conducting a joint evaluation using ANSYS HFSS, we have reached in $h_f = 1.9$ mm, $l_f = 3$ mm, $w_f = 0.8$ mm, $L_s = 6.3$ mm and $W_s = 1.2$ mm for providing the best performance. Figure 3.19 presents the antenna element numerical radiation pattern and S_{11} response. The antenna has provided a 1.31 GHz bandwidth, centered at 26 GHz, in which it provides a 6.4 dBi gain and beamwidth of approximately 70° and 80° at φ = 0° and φ = 90°, respectively.

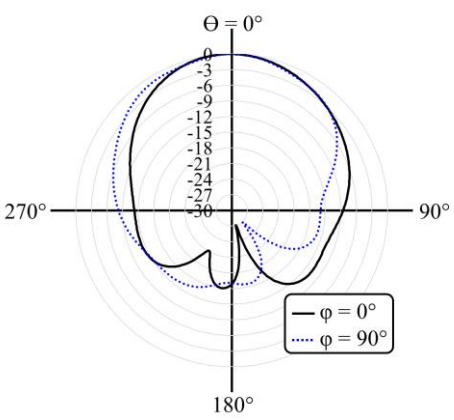

(a) 2D radiation pattern

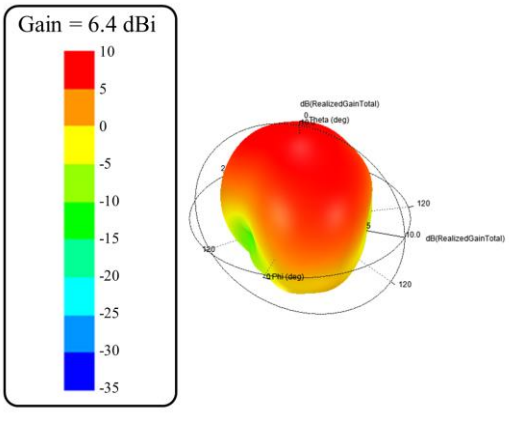

(b) 3D radiation pattern

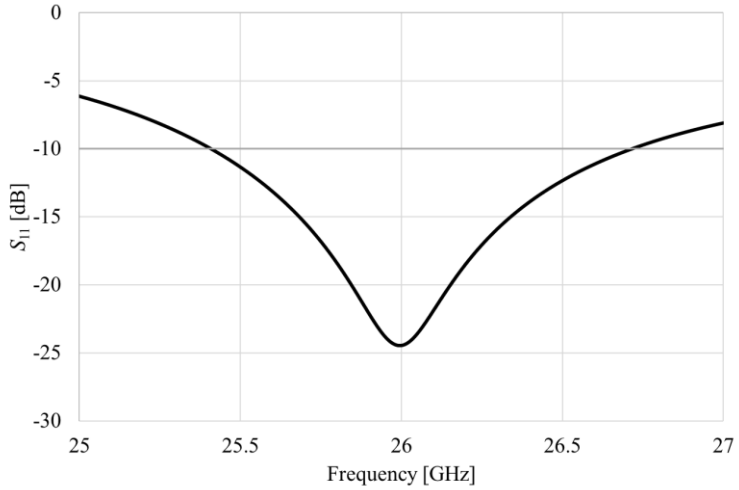

(c) S_{11}

Figure 3.19. Slot antenna numerical results after the optimization process.

The next design step has been regarding the transition design. It is necessary to develop a transition between a *K*-connector and the SICL feeding line so experimental characterization could be posteriorly performed. It is quite challenging designing a transition to feeding a SICL transmission line since the inner conductor is placed in the middle layer. Figure 3.20 presents the proposed solution. In the bottom layer (layer 1), a ground plane circular opening is implemented, so the connector probe and ground would not be short-circuited. The connection between the connector probe and SICL inner conductor is ensured in the second layer. Finally, another ground plane circular opening is implemented at layer 3, and, in its middle, a metallic top hat, or a metal island, is applied for soldering the connector probe. From a practical point of view, this implementation can be achieved by a simple metallic via connecting layers 1 to 3, without short-connecting with ground planes from both top and bottom layers.

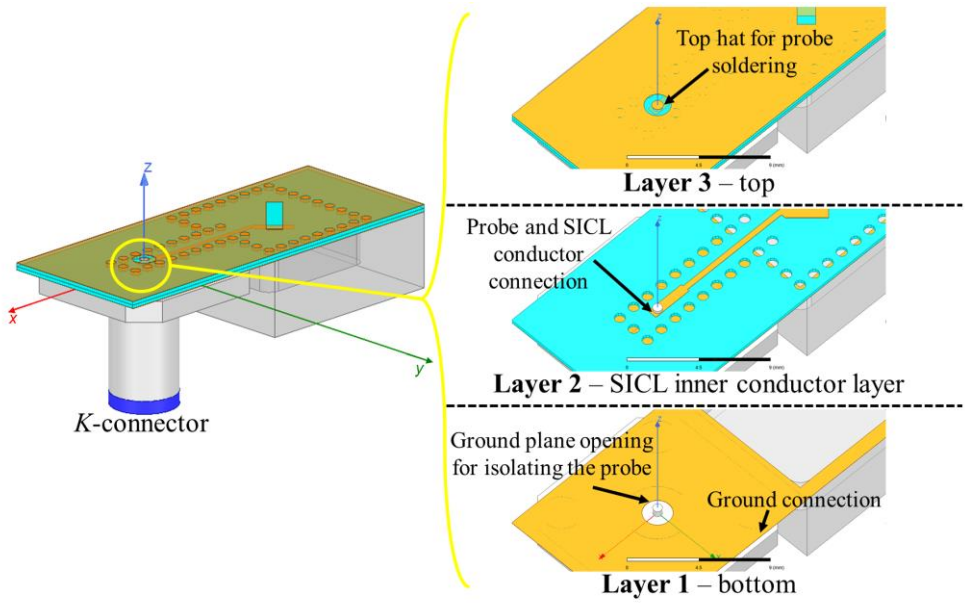

Figure 3.20. *K*-connector to SICL transition solution.

Figure 3.21(a) presents the transition numerical design and its features, whereas Figure 3.21(b) its S-parameters considering a lumped port in the SICL output for transmission coefficient analysis (Port 2). In this design, we have set $r_{hat} = {}^{D}/_{2} = 0.375$ mm since it would be manufactured as a metallic via as the SICL. Additionally, r_{bottom} has been set as 1 mm, $r_{top} = 0.875$ mm and $l_b = 0.5$ mm as initially and manufacturable values. We have then evaluated l_t and w_t for providing the lower S_{11} at the *K*-connector and increase the power transfer between ports 1 and 2 (S_{21}). The numerical procedure has shown itself as a good solution. S_{11} lower than -15 dB and loss lower than 0.5 dB have been ensured in the entire analyzed bandwidth for $l_t = 2.5$ mm and $w_t = 0.7$ mm.

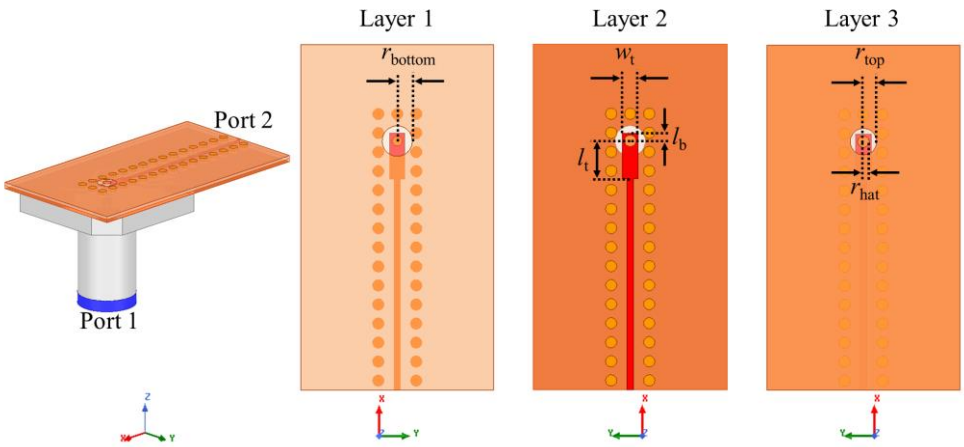

(a) Main features

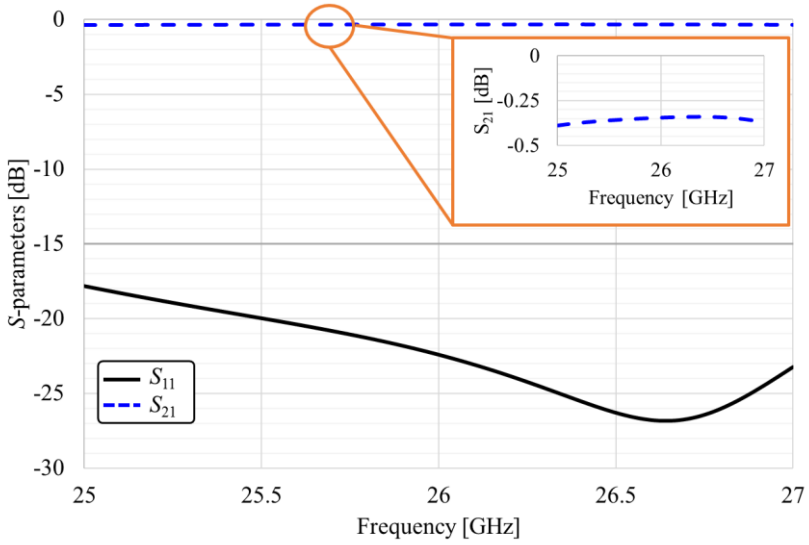

(b) *S*-parameters

Figure 3.21. *K*-connector to SICL transition design and numerical results.

3.3. Antenna Array Development

In the array topology, we have first considered placing 32 elements 45° polarized, on a uniform planar 2x16 arrangement as presented in Figure 3.22. The array is then mirrored for creating a final 64-element dual-polarized array. The spacing between adjacent elements ($d_{elements}$) has been set to accommodate a SICL conductor among them, i. e., we have used the metallic vias in the slot shielding for creating the SICL feeding network by guaranteeing spacing between adjacent cavities' borders equal A = 2.5 mm (from Figure 3.2). In this way, $d_{elements}$ = 12.5 mm ≈ λ at 26 GHz.

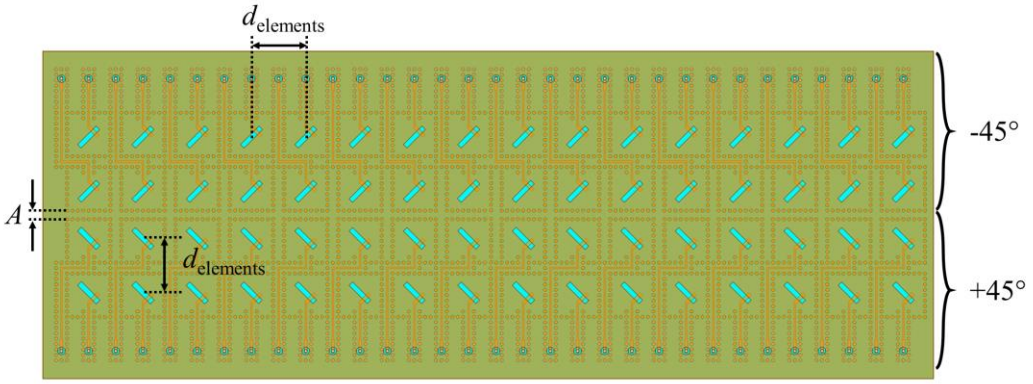

Figure 3.22. Preliminary 64-element array topology.

Figure 3.23(a) presents a 2-element numerical design for reducing the computational effort in the preliminary simulations. If the coupling between two

elements is low enough for considering that the elements do not influence each other, it is expected the reflection coefficient response will not change on any array order. We have chosen the 2-element topology for representing the distinct possible arrangement into the complete array. Figure 3.23(b) presents the numerical *S*-parameters, in which the coupling between the elements is kept lower than -29 dB from 25 to 27 GHz, proving the high-effectiveness shielding effect of both SICL and cavity around the slots. However, it is possible to observe a considerable difference between S_{11} and S_{22}. Element 1 presents a -10 dB reflection coefficient bandwidth from 25.7 to 26.55 GHz, whereas element 2 from 25.3 to 26.5 GHz.

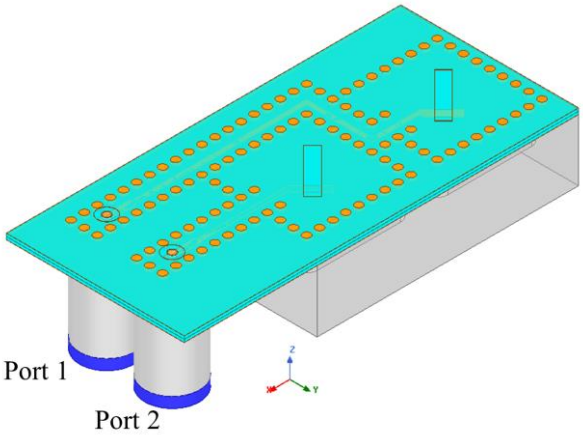

(a) Numerical model

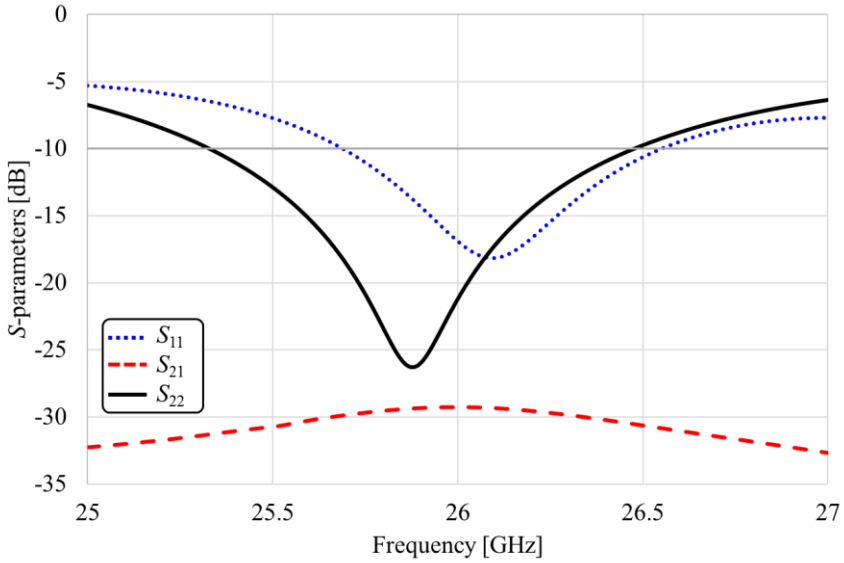

(b) *S*-parameters

Figure 3.23. Simplified investigation of the preliminary 64-element array topology, using two elements.

We have considered further evaluating a second array topology, as presented in Figure 3.24 since the only difference between the two elements is their feeding line length and path. In this new topology, we have shifted lines of the array on a triangular-shaped arrangement. This approach reduces the feeding line complexity, since they are all straight, reduces even more the coupling among elements, since d_{elements} is now increased to 14 mm and $d_{\text{elements\_}h}$ = 12.5 mm and, according to [55], decreases channel correlation when compared with conventional planar square-shaped arrays.

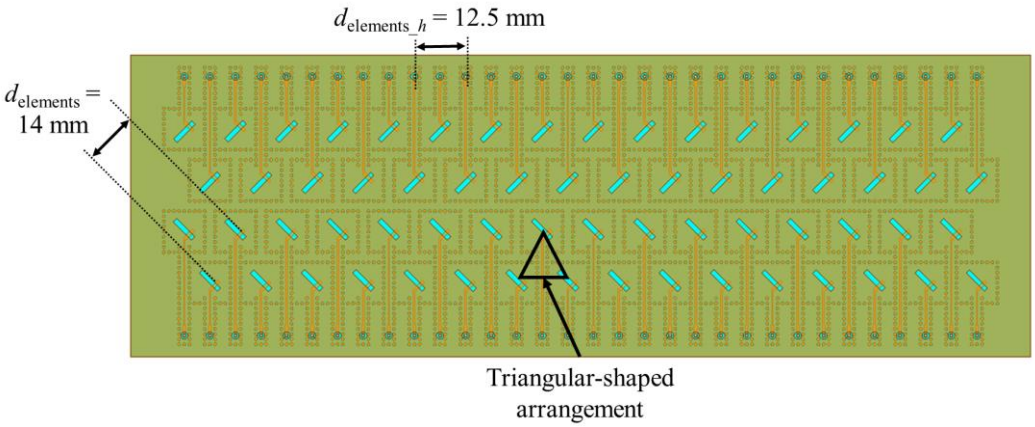

Figure 3.24. The second 64-element antenna array topology, using triangular-shaped arrangement.

Once again, we have firstly simulated a 2-element array for simplicity purposes. Figure 3.25(a) presents the numerical design and Figure 3.25(b) the *S*-parameters results. As expected, coupling between both elements has been kept lower than 40 dB in the entire analyzed bandwidth. However, the reflection coefficient has still presented considerable differences between the elements. Note S_{11} has provided bandwidth from 25.25 to 27 GHz (and beyond), whereas S_{22} has been kept lower than -10 dB from 25.35 to 26.5 GHz. At this point, it became clear the SICL length has a significant influence on the antenna response, which makes sense, since the line design itself has presented high impedance variations throughout the bandwidth as exposed in Figure 3.3 and Figure 3.4, with S_{11} close to -10 dB in some frequencies. Furthermore, it has been possible to conclude the antenna element wideband potential by jointly manipulating the antenna parameters with the SICL length. This numerical design has been the first indication that exactly equal feeding lines in all elements could provide the best array performance in terms of wide bandwidth and frequency response uniformity among all elements.

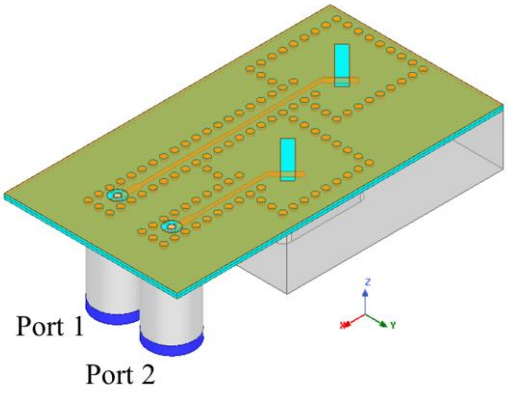

(a) Numerical model

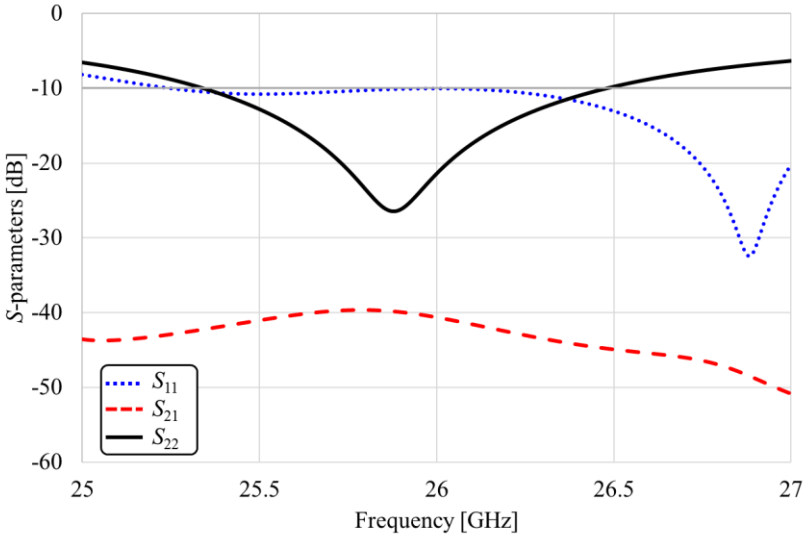

(b) *S*-parameters

Figure 3.25. Simplified investigation of the second 64-element array topology, using two elements.

A step back has been made to confirm the SICL length influence. Figure 3.26(a) presents the numerical design and Figure 3.26(b) the S_{11} magnitude and Smith Chart for multiple values of *l*. Even though the S_{11} magnitude has been kept lower than -10 dB for all evaluated values of *l*, one can note a significant variation in the SICL impedance from the Smith Chart plot, which entails distinct antenna frequency response if they are fed with different SICL lengths. These results prove the SICL length influence in the antenna design, which means the antenna element and SICL should be jointly designed for providing the desired frequency response. From this point forward, we have considered all the elements exactly the same, including the SICL feeding line length and path between slot and *K*-connector.

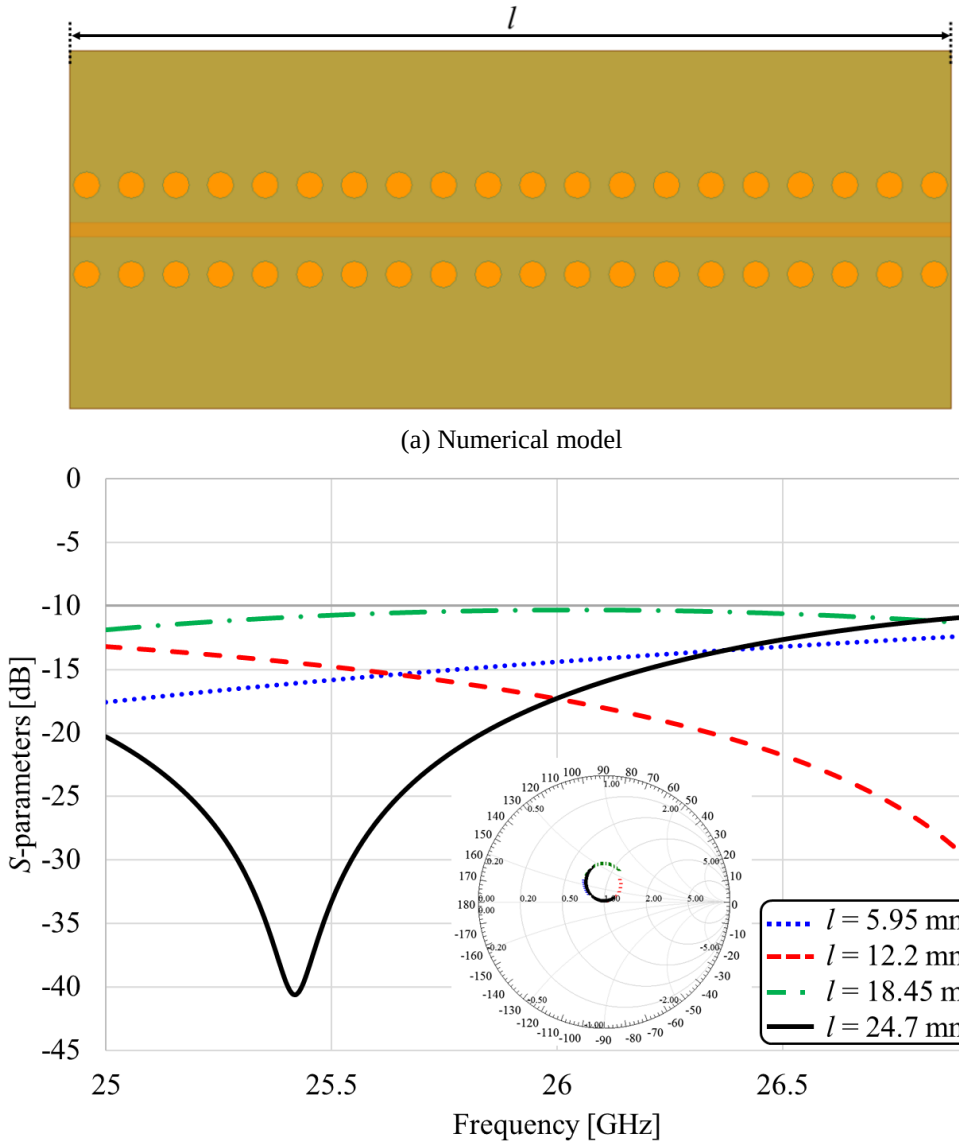

(a) Numerical model

(b) *S*-parameters

Figure 3.26. SICL length evaluation.

Figure 3.27 presents the third 64-element array topology proposal. Basically respects the same arrangement from the one presented in Figure 3.24, but with the SICL extended in the extreme array lines for providing the same length in all 64 elements, considering l_{SICL} = 21.375 mm. Figure 3.28(a) presents the 2-elements array for numerical preliminary evaluation and Figure 3.28(b) its *S*-parameters. The coupling between the elements has been further enhanced and kept lower than -48 dB from 25 to 27 dB and both S_{11} and S_{22} have presented the same behavior, providing a 2-GHz bandwidth, from 25 to 27 GHz. Note the extremely wide bandwidth, reached by properly tuning the antenna jointly with the SICL length and transition parameters.

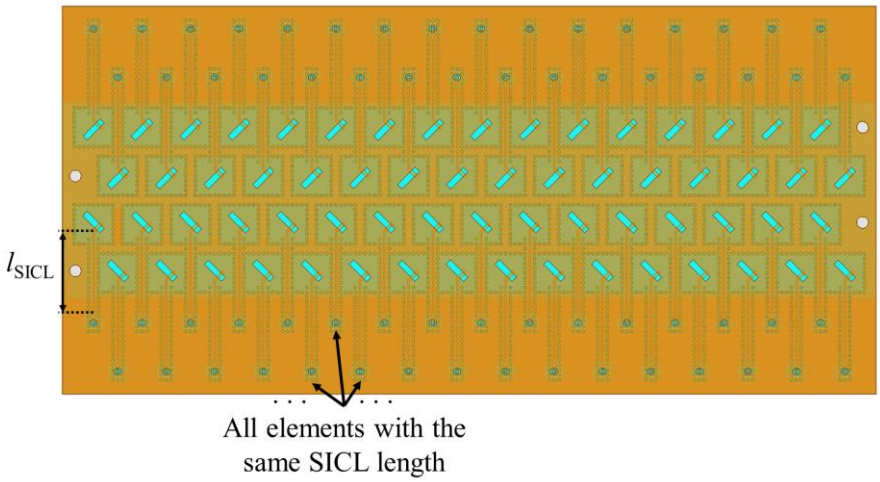

Figure 3.27. The second 64-element antenna array topology, using triangular-shaped arrangement and extended feeding lines.

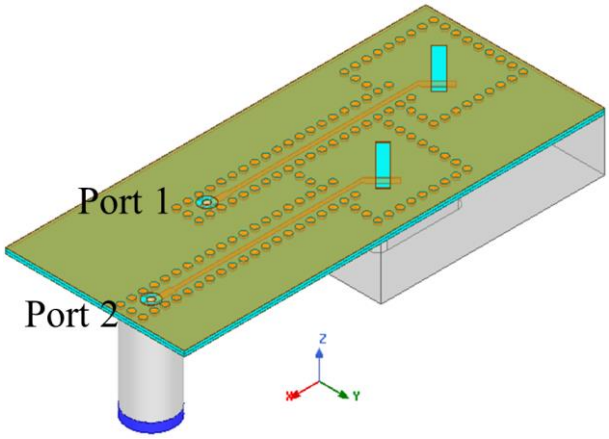

(a) Numerical model

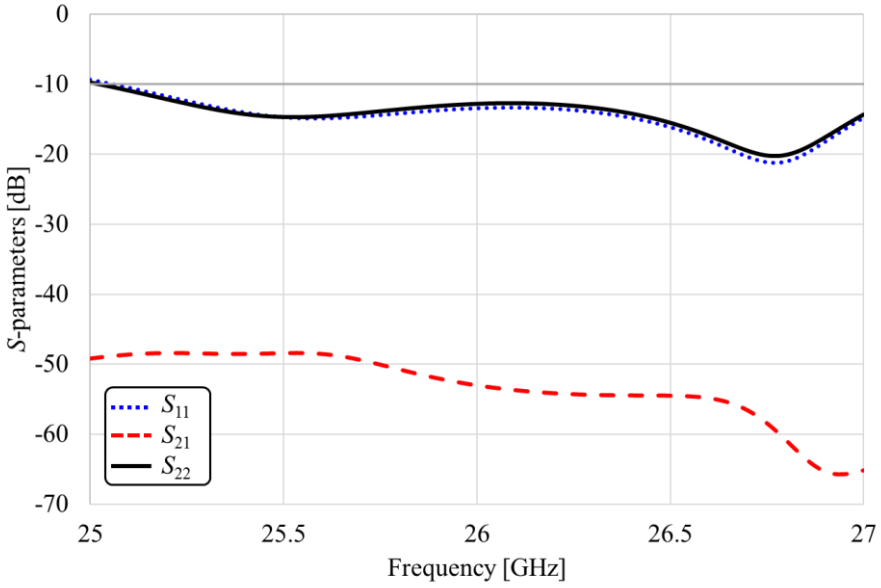

(b) *S*-parameters

Figure 3.28. Simplified investigation of the third 64-element array topology, using two elements.

Since a good performance has been achieved, a manufacturing company has been contacted for adapting the antenna numerical design considering mechanical constraints. From the printed point of view, the company Lauquen Printed Circuits has included a prepreg laminate between the two substrate layers for gluing the two Rogers Arlon CuClad 233 laminates on multi-layer employment. We have chosen the Rogers RO4450F prepreg, with $\varepsilon_r = 3.52$, $\tan\delta = 0.004$ and $t = 0.1$ mm. At this point, we have considered the prepreg in the numerical simulations according to Figure 3.29(a), ensuring the slot and feeding network would be separated only by a CuClad substrate as initially designed. Figure 3.29(b) presents the numerical S_{11} comparison between two identical antennas in terms of dimension, the only difference is regarding the prepreg employment. One can note a severe impedance matching degradation, in which the prepreg implementation resulted in approximately 50% bandwidth reduction, operating now from 25 to 26 GHz.

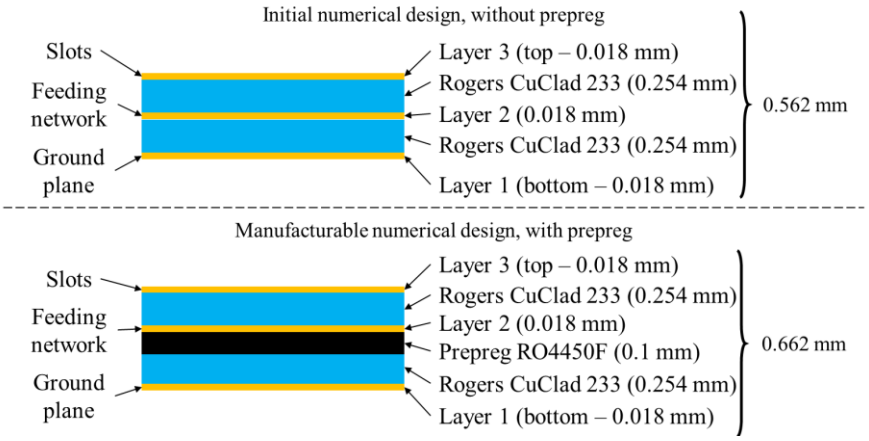

(a) Numerical multi-layer design

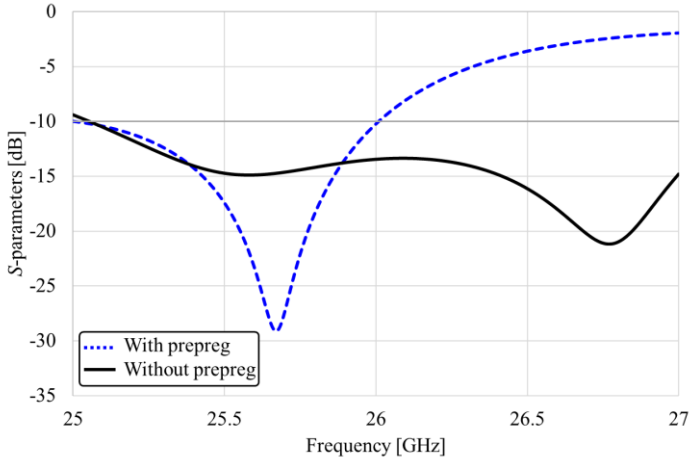

(b) *S*-parameters

Figure 3.29. Prepreg analysis.

The impedance mismatch was expected since the structure resultant electric permittivity and tangent loss have been changed. However, increasing the substrate thickness brings out the potential of increasing impedance matching in a wider frequency range [104]. In this case, re-tune the antenna has consisted of a fine adjustment in the transition line and slot dimensions for re-matching the antenna. We have used the "derivative" solution from HFSS, in which it is possible to select some variables for a post-processing tuning. If the desired response is achieved, a full-wave simulation is conducted to confirm the results. Table 3.1 presents all the antenna previous explained parameters with their respective values for optimized performance with and without prepreg employment. Nine variables have been changed after tune refinement, besides h_{cav}, which has been redesigned for considering the prepreg height and ensuring a λ/4 distance from its bottom to the slots, all the other eight parameters have been related to feeding line and slot.

Table 3.1 – Antenna main dimensions for optimized performance with and without prepreg.

Parameter	Without prepreg [mm]	With prepreg [mm]
h	0.254	0.254
A	2.5	2.5
D	0.75	0.75
S	1.25	1.25
w	0.4	0.67
L_s	6.3	5.2
W_s	1.2	2.01
h_{cav}	2.88	2.272
h_f	1.9	1.51
l_f	3	3.4
w_f	0.8	0.64
r_{hat}	0.375	0.375
r_{top}	0.875	0.875
r_{bottom}	1	1
l_b	0.5	0.5
l_t	2.5	2.5
w_t	0.7	1.11
l_{SICL}	21.375	20.985

Figure 3.30 presents a 2-element array numerical design and the simulated electric field with both ports activated, in which it is possible to see good electromagnetic isolation. Figure 3.31 presents the antenna element main electromagnetic results. It has provided a 1.8-GHz bandwidth, from 25 to 26.8 GHz (6.9%) considering S_{11} lower than -10 dB and a 1-GHz bandwidth for S_{11} lower than -20 dB. Furthermore, it has achieved a beamwidth of approximately 85° in both planes and gain of 7 dBi at 26 GHz. Coupling between the elements has been kept

lower than -44 dB throughout the entire antenna operating bandwidth, ensuring outstanding performance.

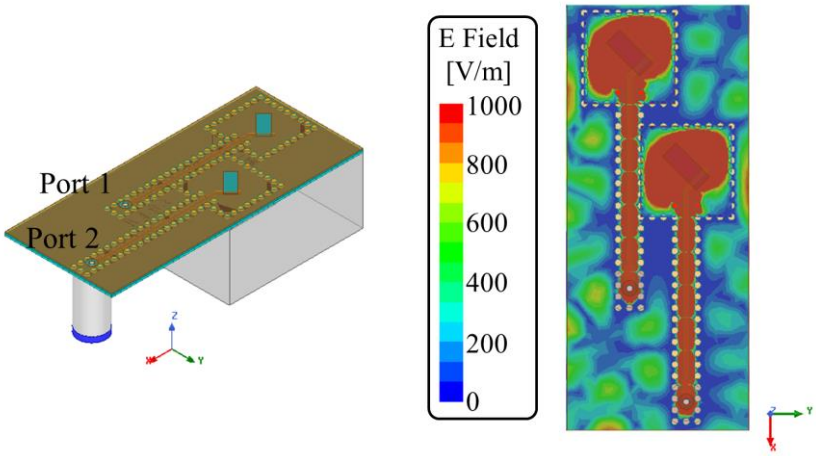

Figure 3.30. 2-element array final design with prepreg.

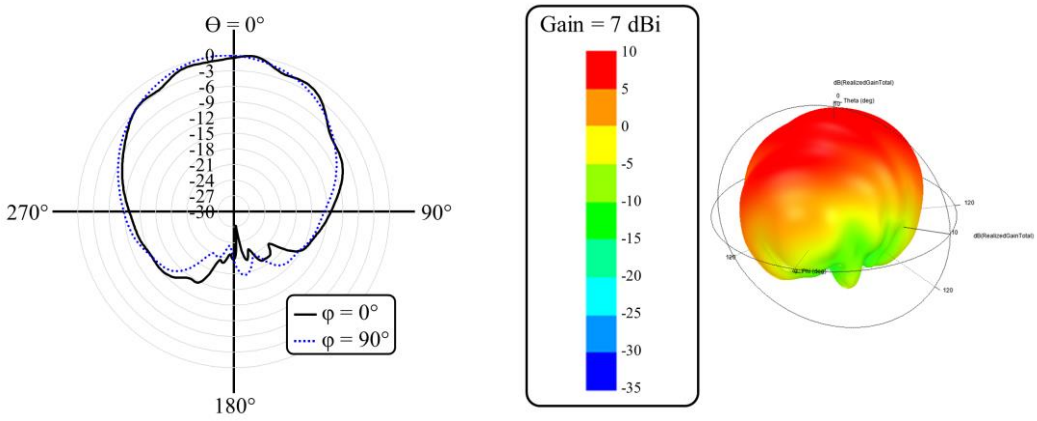

(a) 2D radiation pattern (b) 3D radiation pattern

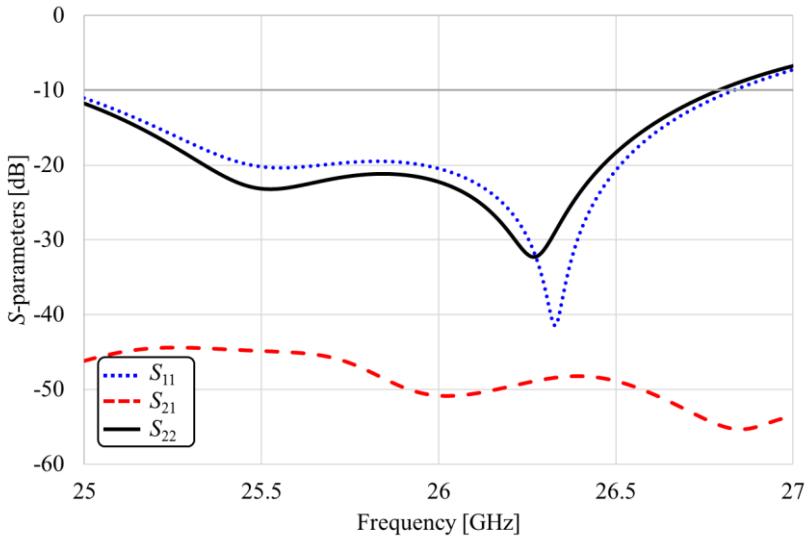

(c) S_{11}

Figure 3.31. Slot antenna numerical results after the optimization process.

A full-wave complete simulation has been conducted for analyzing the 64-element array performance. Figure 3.32(a) presents the electric field plotted in the structure with all the ports activated, with the same magnitude and phase. It is possible to see the propagating mode inside each element shielding, without coupling among themselves. Figure 3.32(b) presents some transmission coefficients between two ports, in which all of them are kept lower than -45 dB from 25 to 27 GHz. Figure 3.32(c) reports the 64 active reflection coefficients (all ports), in which it is possible to evaluate the antenna bandwidth considering the coupling among elements when they are all activated. It is possible to see in the worst-case scenario a bandwidth from 25 to 26.6 GHz.

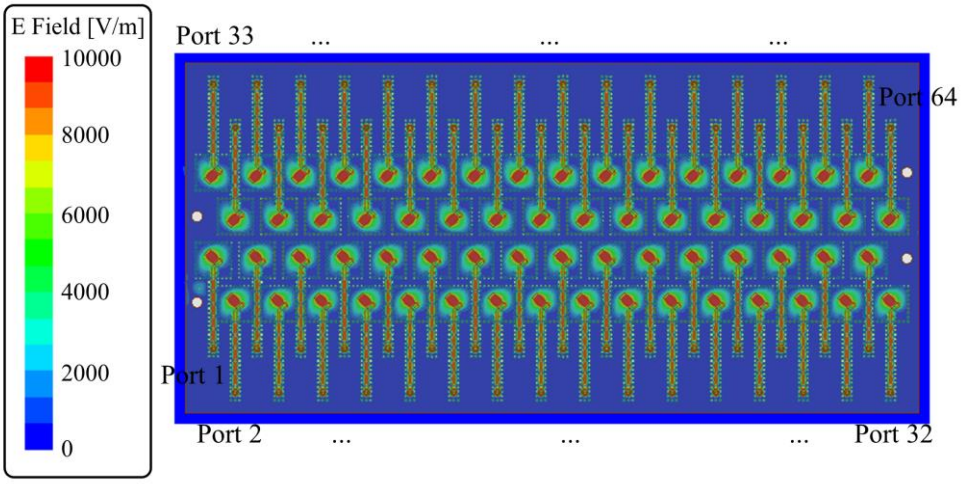

(a) Electric field

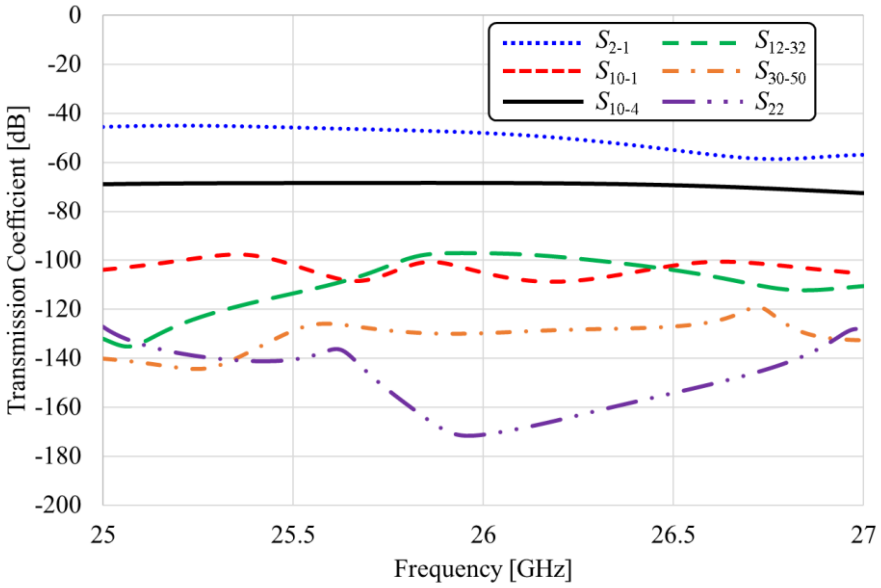

(b) Transmission coefficient

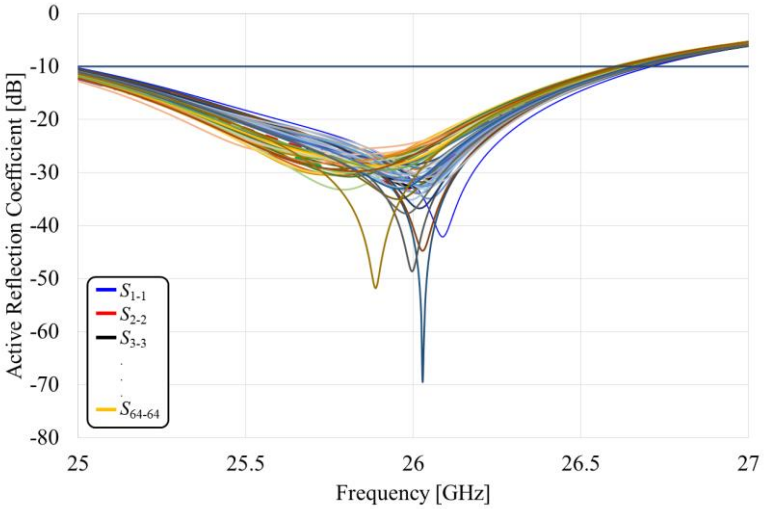

(c) Active reflection coefficient, proving that all antenna array elements provide the same bandwidth

Figure 3.32. 64-element antenna array numerical results.

Figure 3.33 presents the array radiation pattern considering a unique active element, in which it is possible to observe the element does not suffer from interference from the array structure and keeps its 7-dBi gain. This result proves the element capability of independently operating into a 64-element and dual-polarized array, without compromising its performance.

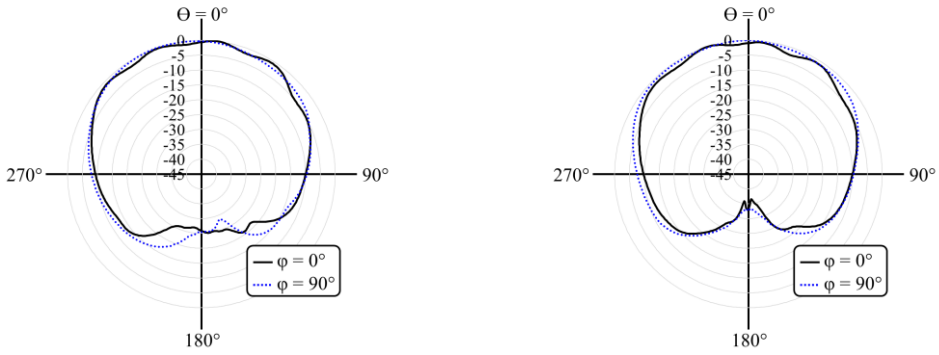

(a) Element 1 (b) Element 16

(c) Element 35 (d) Element 64

Figure 3.33. Numerical radiation pattern of an element into the 64-element array.

An eleven-step design process has been made throughout the research and explained in this document. Figure 3.34 presents the evolution from the first concept all the way to the final design, which highlights the complexity of designing low-coupling and high order antenna arrays aimed at mMIMO applications. Furthermore, the printed part from the prototype has been manufactured and Figure 3.35 presents some photographs, including a total top and bottom view, a unique element close, the feeding line shadow in the intermediate layer (possible to view it by properly illuminating from below the structure), the probe connection in the transition line and the *K*-connector employment. The back cavities have been defined to be milled in stainless steel by our group partner Prodmec Engineering. Their engineers have confirmed there were no mechanical constraints and the prototype is also presented in Figure 3.35. The next steps are regarding characterization.

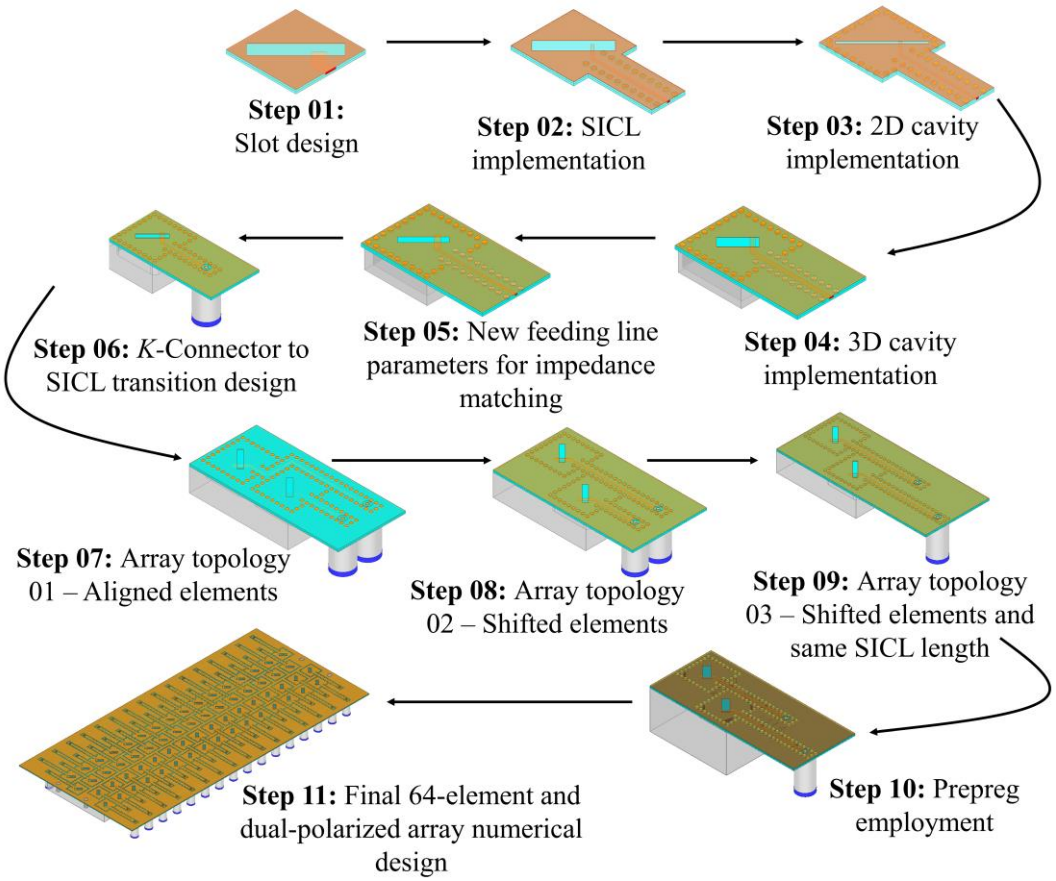

Figure 3.34. SICL-SAA eleven-step development process.

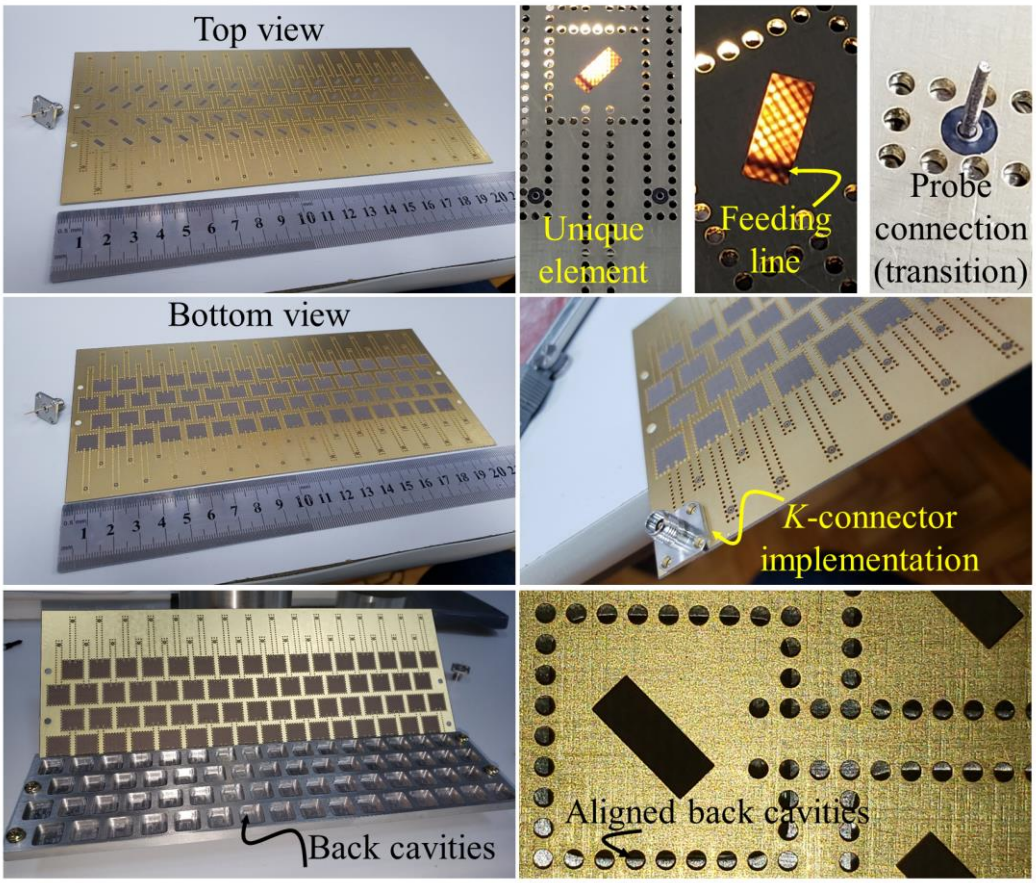

Figure 3.35. SICL-SAA prototype photographs.

Chapter 4

4. SICL-SAA Performance Analysis and Characterization

4.1. New Methodology for Evaluating Large-Scale MIMO Antenna Arrays Radiation Pattern

It has been previously explained in Chapter 2 the antenna elements into an antenna array applied to TDD-based mMIMO are independently treated. From a RF point of view, exciting the multiple antennas with distinct phases and magnitudes will entail a resultant radiation pattern. This Section intends to evaluate the resultant array radiation pattern considering some channel scenarios.

We have firstly investigated a dipole-based array for better understanding these radiation features under multipath channel conditions. The dipole has been chosen since it has a well-known radiation behavior and reduces the computational effort. Furthermore, it is expected to be used as a reference for comparing with our prototype. Figure 4.1 presents the main properties of a half-wavelength dipole antenna, designed for the 26 GHz band and the used linear array in our proof-of-concept, considering a BS with omnidirectional coverage. The element has provided a 4.48 GHz bandwidth from 24.18 to 28.66 GHz (Figure 4.1(a)) and 2.5 dBi gain at 26 GHz, with an omnidirectional radiation pattern in the *H*-plane (Figure 4.1(b)). Multiple elements have been arranged into a linear array along its *H*-plane, as presented in Figure 4.1(c), and spaced by one wavelength to take advantage of uncorrelated channels.

Figure 4.2(a) is related to a 64-element dipole-based array normalized radiation pattern when its elements are excited in phase, i.e. all elements with the same magnitude (1W) and phase (0°). This radiation pattern would be created if no multipath is considered and a clear line of sight (LOS) is defined between the 64 transmitting antennas and UE as illustrated in Figure 4.2(b). One can note the array capability of creating directive beams pointed to well-defined directions, even though high grating lobes have been created, as expected by the array factor theory [104], since the spacing between adjacent elements is close to λ. It is important to highlight this antenna array has not been designed to operate in this scenario, so its performance is poorer if compared to half-wavelength-spaced phased arrays.

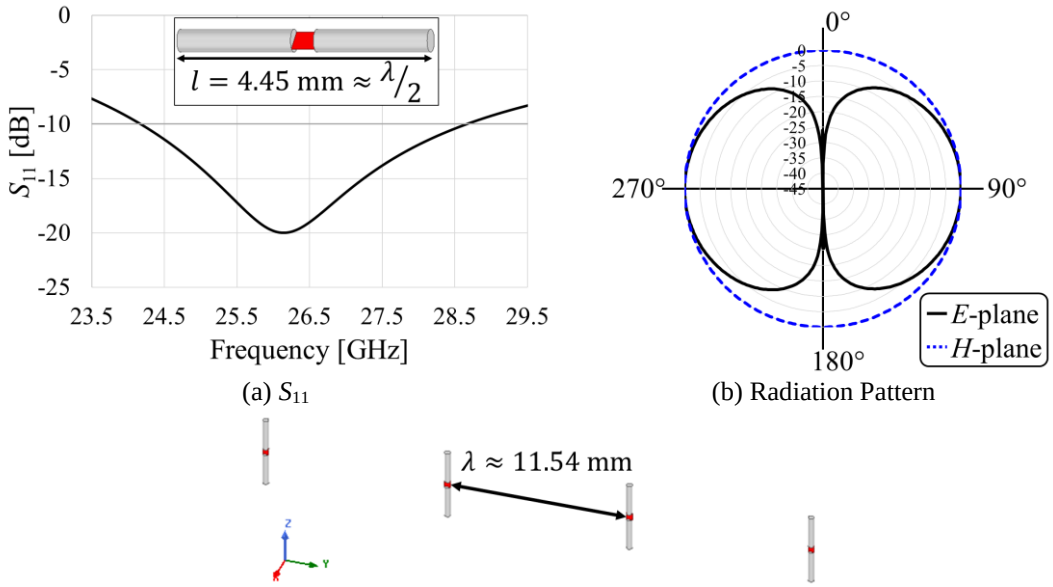

(a) S_{11} (b) Radiation Pattern

(c) Linear array topology

Figure 4.1. Half-wavelength dipole element and the used linear array in our proof-of-concept, considering a base station with omnidirectional coverage.

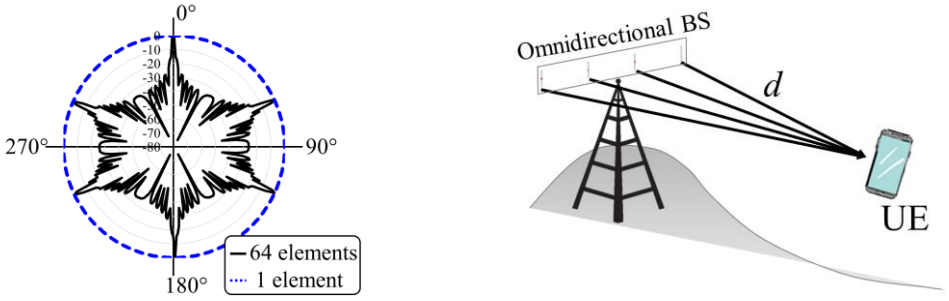

(a) *H*-plane radiation pattern (b) Scenario

Figure 4.2. 64-element antenna array analysis under LOS condition.

From this point and on, we perform our evaluation in multipath environments. Figure 4.3(a) illustrates a multipath scenario under non line of sight (NLOS) conditions. Remembering a TDD based digital mMIMO system allows to compensate each channel response directly in the antenna element, in such a way we could excite the antenna array with a Rayleigh distributed vector in magnitude and uniformly distributed vector in phase, as previously explained in Chapter II. Each position from the vector, with 64 positions, excites one radiating element. Numerically, we could apply this excitation by using the post-processing tool from the full-wave simulator ANSYS HFSS, in which we could stablish the magnitude and phase of each port as desired. We have created arbitrary and completely uncorrelated samples for emulating an uncorrelated channel environment. Figure 4.3(b) presents the resultant radiation pattern considering the channel scattering. One can note the antenna array is capable of covering a wider area in the Azimuth plane (H-plane), with maxima and nulls ruled by the channel multipath, when compared to the LOS case from Figure 4.2(a). This feature is deeply confirmed by the evaluation of the resultant array radiation pattern under the influence of channel variation considering 4, 16 and 64 elements. Figure 4.4 displays the 4 element array normalized resultant radiation pattern, whereas Figures 4.5 and 4.6 report the results of the 16- and 64 element antenna arrays, respectively; in all cases compared to the one half-wavelength dipole. Particularly, Figures 4.4(a), 4.5(a) and 4.6(a) are under the same channel influence, named channel 1, whereas Figures 4.4(b), 4.5(b) and 4.6(b) are under a second channel influence (channel 2). The difference between the two considered channels is only their generation, maintaining the same statistical parameters ($\sigma = 4$), i.e. two distinct events of the same stochastic process, which could represent two periods with different coherence time.

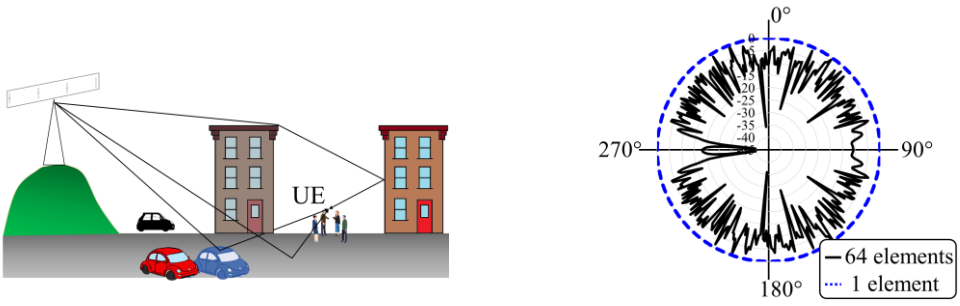

(a) Scenario (b) *H*-plane radiation pattern

Figure 4.3. 64-element analysis under a Rayleigh channel.

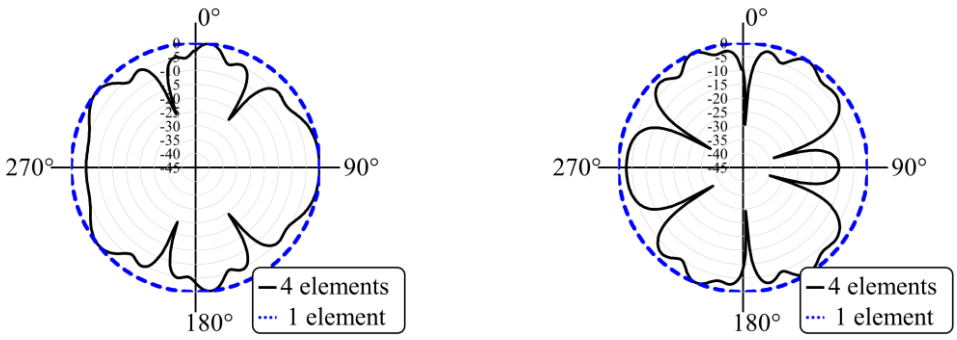

(a) Channel 1 (b) Channel 2

Figure 4.4. Radiation pattern analysis for 4 elements, under the influence of two identically distributed and independent Rayleigh channels.

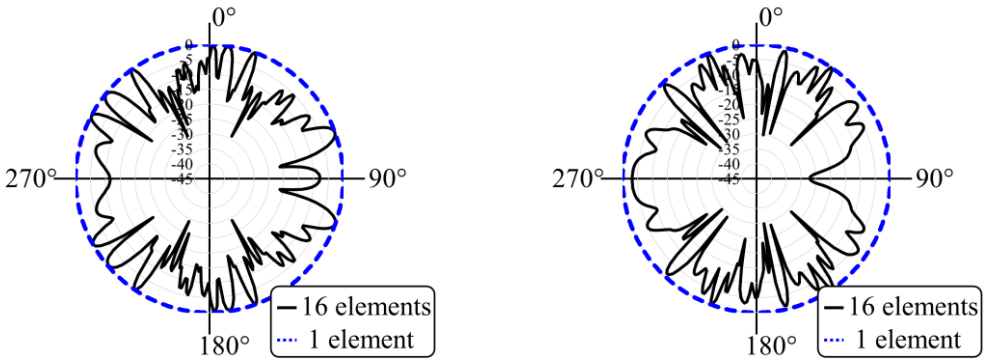

(a) Channel 1 (b) Channel 2

Figure 4.5. Radiation pattern analysis for 16 elements, under the influence of two identically distributed and independent Rayleigh channels.

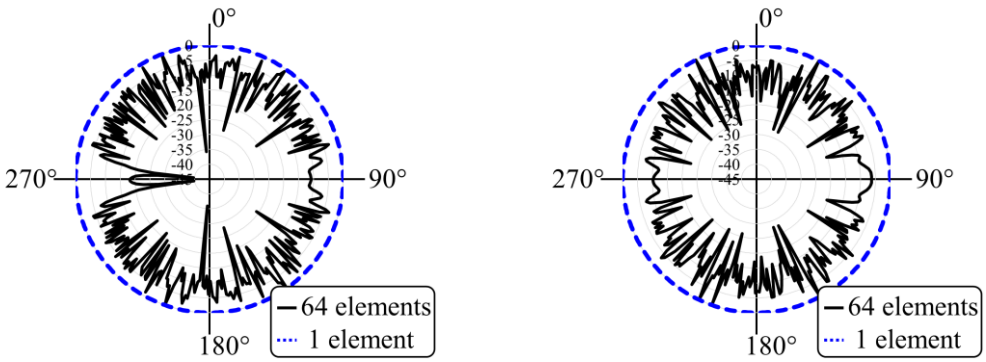

(a) Channel 1 (b) Channel 2

Figure 4.6. Radiation pattern analysis for 64 elements, under the influence of two identically distributed and independent Rayleigh channels.

The analyses of Figures 4.4, 4.5 and 4.6 allowed us to demonstrate two well-stablished achievements from mMIMO systems, using the proposed methodology: ***i)*** increasing the number of elements enables to cover a wider area in the *H*-plane with more prominent maxima in the radiation pattern, thus enhancing the mMIMO spatial resolution (as expected by the mMIMO theory), since each mini-lobe has narrower

beam; ***ii*)** by comparing the results of two identically distributed and independent Rayleigh channels, it becomes clear the radiation pattern maxima and nulls are ruled by the wireless channel variations. The latter one implies in radiation pattern adaptation according to the channel, i.e. the RF signal angle of arrival and correspondent excitation for each array element. Differently from the mMIMO theory [43][78], which typically takes use of capacity and codification features, we innovate by demonstrating the same principles by only evaluating the digitally-beamformed radiation pattern.

Posteriorly, we have also evaluated the influence of channel correlation on the antenna array resultant radiation pattern. In this context, we have considered multiple environments, in which the multiple channels between transmitter and receiver, different matrix elements from (2.7), have a controlled correlation. Figure 4.7(a) describes the proposed scenario with multiple channels correlated by the correlation coefficient ρ, in which each antenna element has its own independently controlled RF chain, as predicted in the mMIMO theory [52][55][56][78][97][102]. Each channel correlation is regarded to a specific environment, in which the $\rho = 0$ represents a non-correlated NLOS multipath environment. Whilst ρ increases, distinct channel correlation scenarios are observed, which implies reducing the number of independent paths between transmitter and receiver. The correlation might be managed by implementing a low-pass spatial filtering process [96], as illustrated in Figure 4.7(b). This method introduces correlation to adjacent channels, previously non-correlated, for emulating the wireless propagation environment variation. Figure 4.7(c) displays the spatial filter impulse response considering four channel scenarios. Therefore, the adjacent channel correlation is managed by varying the factor α from the spatial filter impulse response, described as $g(x) = \text{sinc}(\alpha x)$.

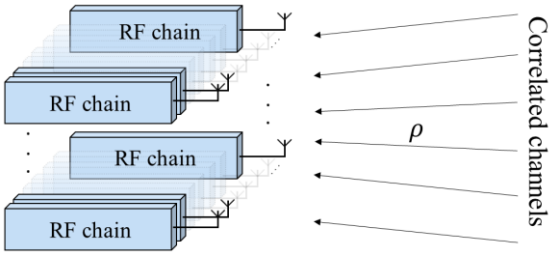

(a) Scenario with correlated channels

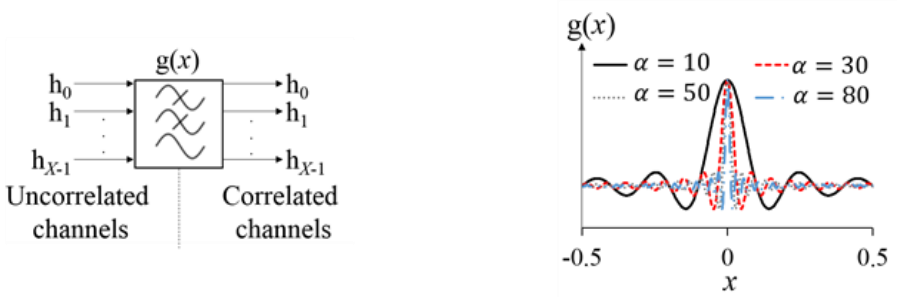

(b) Spatial filtering (c) Filter response

Figure 4.7. Proposed approach to investigate channel correlation influence on the resultant array radiation pattern.

Figure 4.8 depicts the channel correlation factor ρ, as a function of α. We have used Matlab for implementing a Monte Carlo simulation to estimate ρ between samples from the filtered vector. The algorithm returns a matrix of correlation factors, in which the calculated coefficients, above and below the main diagonal, represent the correlation factor between each pair of adjacent channels. It is worth mentioning the observed ρ values have been obtained by taking the mean of all adjacent channel pairs. As expected, ρ decreases as α increases, in light of the filter response.

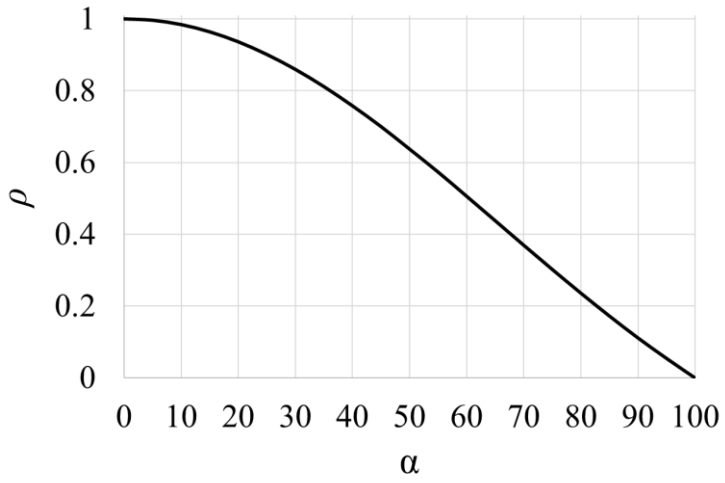

Figure 4.8. Correlation coefficient as a function of the filter factor.

We have chosen four channel scenarios, whose the correlation coefficient values are defined in Table 4.1. Figure 4.9 reports the array resultant radiation patterns considering ρ varying from 0.24 to 0.98. Highly correlated channels (ρ = 0.98), demonstrated in Figure 4.9(a), provide a directive beam at boresight direction, implying in less independent paths between BS and UE, due to the linear dependence between the samples. As ρ reduces, it is possible to observe a dynamic change in the

radiation pattern, in which Figure 4.9(b), 4.9(c) and 4.9(d) present a progressive increase in the number of lobes and nulls, enhancing the mMIMO spatial resolution by means of taking advantage of more paths. As a conclusion, we demonstrate that the radiation pattern is highly-dependent on the correlation level of the channel response, coming from Figure 4.2(b) to Figure 4.3(b), i.e., completely correlated to uncorrelated channel samples, respectively. This investigation ratifies the need for uncorrelated channels for proper mMIMO operation [102]. As a consequence, large antenna arrays operating at low correlation levels provide many narrow beams, enabling to cover a wider area in the Azimuth plane, similar to that of a unique element.

Table 4.1 – Relation between the filter response and channel correlation for the four evaluated scenarios.

α	ρ
10	0.98
30	0.86
50	0.64
80	0.24

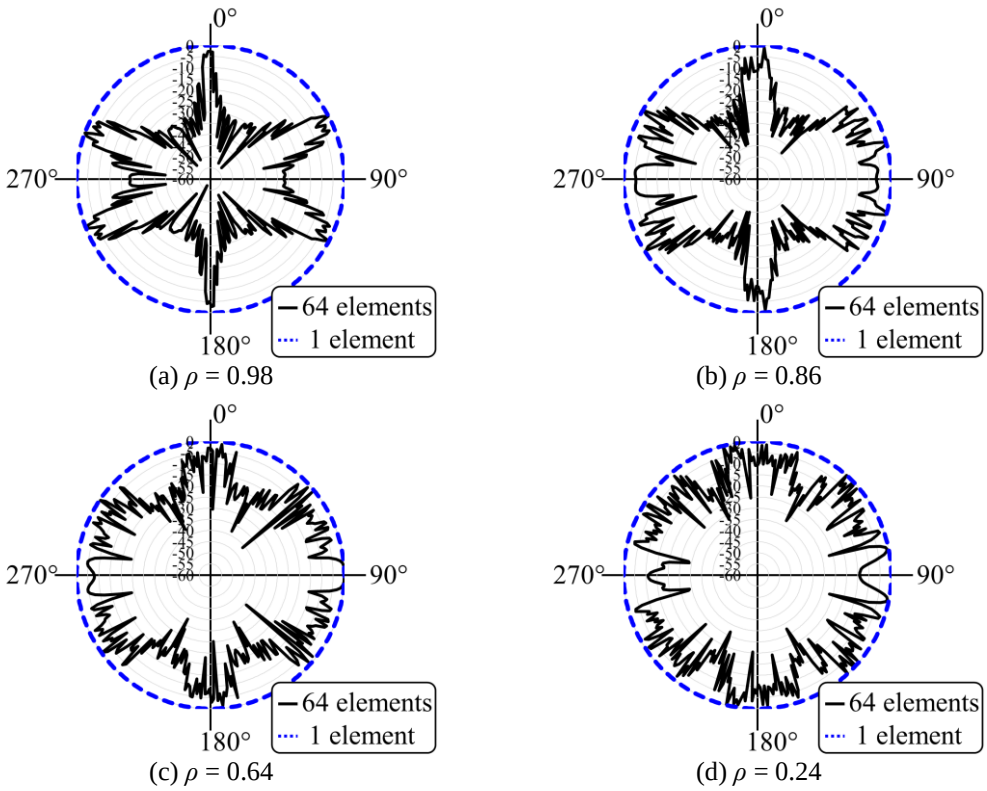

Figure 4.9. Radiation pattern analysis for 64 elements, under the influence of correlated channels as a function of ρ.

Finally, we introduce the concept and the initial application on a novel figure of merit, which has been idealized for obtaining the resultant antenna array radiation

pattern from digitally-processed-based beamforming systems. By considering a digital beamforming approach, one might infer the minimum gain contribution from an antenna array is the gain from a single antenna array element. This means any gain lower than the gain from a unique antenna may be resultant from the overlapped secondary lobes and not from a predominant channel path. In this way, we have conceived the Λ factor, by computing the number of lobes with gain higher than the one-element antenna (N_{Lh}) divided by the one-element antenna beamwidth in the analyzed plane ($\theta_{\mathrm{ab\_element}}$ or $\phi_{\mathrm{ab\_element}}$) in radians. For instance, the Λ factor for the antenna array from Figure 4.1(c), in which the array elements are disposed along the *y*-axis, in the *H*-plane is given by

$$\Lambda = \frac{NL_h}{\emptyset_{ab\_element}} [\mathrm{lobes/rad}]. \tag{4.1}$$

Figure 4.10 presents the radiation pattern from 4, 16 and 64 dipole-based antenna arrays compared to that of one half-wavelength dipole antenna. We have created a Matlab code for properly counting the lobes and calculating the proposed figure of merit. From Figure 4.10(a), one can observe 5 lobes crossing the radiation pattern from the one half-wavelength dipole, giving rise to Λ = 0.79 lobes/rad from (4.1) considering $\phi_{\mathrm{ab\_element}} = 2\pi$. Analogously, there are 24 and 72 lobes with gain higher than one array element in Figures 4.10(b) and 4.10(c) respectively, resulting in Λ = 3.82 lobes/rad and Λ = 11.46 lobes/rad for 16 and 64 dipole-based antenna arrays, correspondingly. As a conclusion, the higher is the number of elements, higher is Λ, corroborating with the conclusions made from the analyses of Figures 4.4, 4.5 and 4.6.

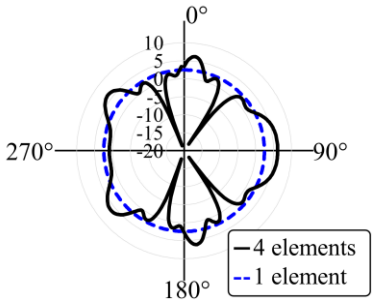

(a) 4 elements

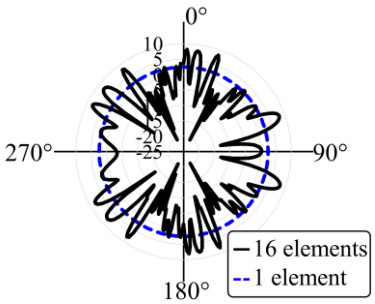

(b) 16 elements

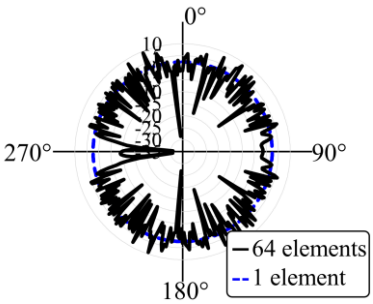

(c) 64 elements

Figure 4.10. Non-normalized radiation pattern analysis for Λ calculation.

We have also evaluated the Λ factor variation in correlated channel environments, using the parameters from Table 4.1 and the radiation pattern properties from Figure 4.11, as reported in Table 4.2. One can conclude the Λ factor increases as the correlation among channels decreases, which is also expected, since low channel correlation means high diversity environment with more lobes for covering diverse paths. Moreover, Figure 4.11 shows more crossed beams, when compared to one-element dipole, as the correlation decreases.

Table 4.2 – Relation among the filter response, channel correlation and Λ parameter for the four evaluated scenarios considering a 64-element dipole-based antenna array.

α	ρ	Λ [lobes/rad]
10	0.98	1.91
30	0.86	4.14
50	0.64	7.32
80	0.24	10.50

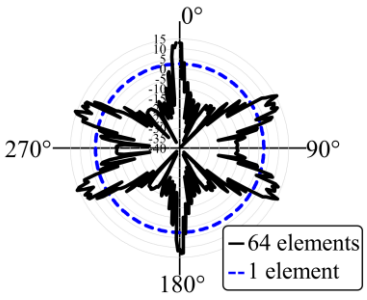

(a) ρ = 0.98

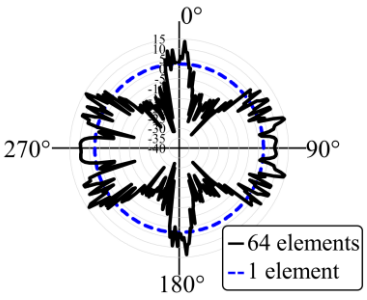

(b) ρ = 0.86

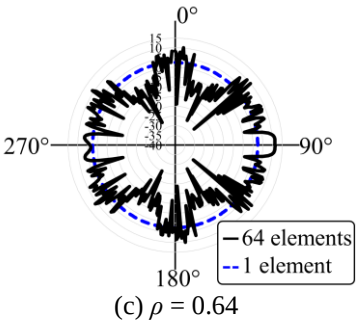

(c) ρ = 0.64

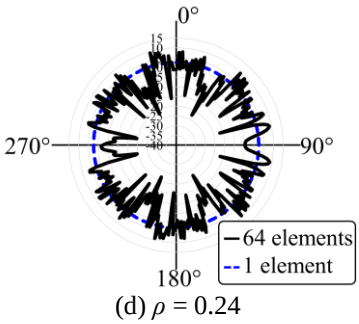

(d) ρ = 0.24

Figure 4.11. Non-normalized radiation pattern analysis for Λ calculation considering 64 elements under the influence of correlated channels as a function of ρ.

It is important to highlight that the proposed figure of merit could contribute to define the most appropriate array element and/or topology, since it allows to evaluate different antenna arrays performance under the same wireless channel influence. In other words, the Λ factor might be considered potential as the first investigation of a real wireless deployment for numerically testing diverse radiating elements (patch, slot, dipole or others) and array topologies (linear, squared, triangular, hexagonal, etc) considering the channel distribution. The proposed figure of merit empowers an additional and efficient radiation pattern analysis mechanism for antenna designers from mMIMO systems. Its major advantage is the mentioned professionals do not need to have a background on the system-level features, since our methodology considers only the RF level.

4.2. SICL-SAA Performance Analysis

The SICL-SAA complete full-wave simulation has been further investigated on a post-processing setup, in which the phase and magnitude of each antenna element could be managed. The first scenario is illustrated in Figure 4.12(a), in which no multipath is considered and a clear line of sight is defined between each transmitter antenna and UE. If *d* is long enough so each link could be considered parallel among themselves, it is fair to assume all the channels would experience the same magnitude and phase. In this case, we could apply in the HFSS post-processing tool all the 64 elements magnitude equal to 1 W and phase equal to 0°. The resultant radiation pattern is given in Figure 4.12(b).

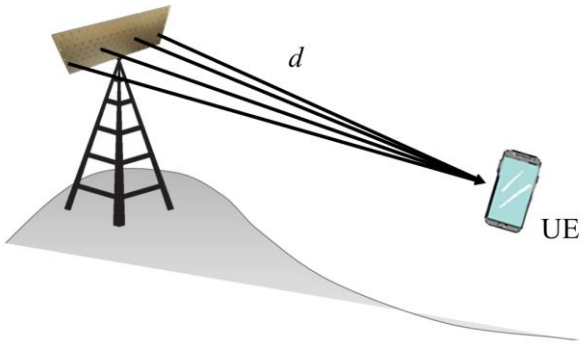

(a) Propagation environment

Antenna port	Magnitude [W]	Phase [°]
1	1	0
2	1	0
3	1	0
4	1	0
5	1	0
…	1	0
64	1	0

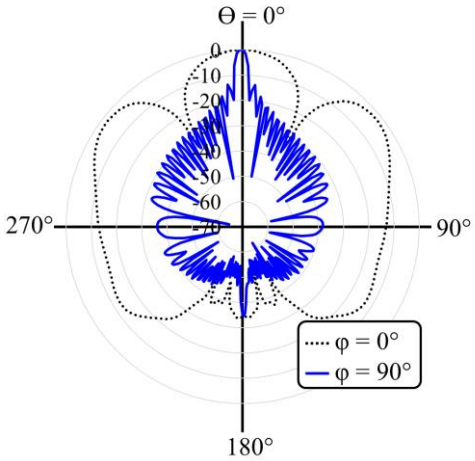

(b) Radiation pattern and excitation

Figure 4.12. Array radiation pattern analysis under a multipath-free and LOS propagation environment.

One can note the SICL-SAA has the capacity of creating a directive beam pointed to a unique direction in φ = 90° (horizontal plane). High grating lobes have been created in φ = 0° (vertical plane) since the spacing between adjacent elements is close to one wavelength. It is important to highlight this antenna array has not been designed for operating in this scenario, so its performance is poorer when compared with conventional phased arrays, half-wavelength spaced. In any case, we have initially evaluated this scenario to prove the concept the antenna can compensate the channel phase rotation and magnitude and properly point the main beam to UE.

Similar to that presented in Section 4.1, we could also excite the SICL-SAA with uncorrelated samples. In Figure 4.13(a), multiple obstacles are founded between BS and UE, in the way no line-of-sight is created. Multiple paths are created between each antenna from the BS array and UE, so each channel is Rayleigh distributed. Note in Figure 4.13(b) the resultant radiation pattern when excited by uncorrelated channels. The antenna array is capable of covering a wide-angle area, with maximums and nulls ruled by the channel multipath.

The next step has been regarding the evaluation of the SICL-SAA radiation pattern under the influence of channel variation. Furthermore, we have evaluated the resultant dual-polarized radiation pattern considering all 64 elements activated and just one-quarter of them (16 elements) to analyze the influence. It is important to highlight the radiation pattern and gain are the same for all active 64 dual-polarized elements

and just 32 single polarized ones since orthogonal polarization should not interfere between themselves.

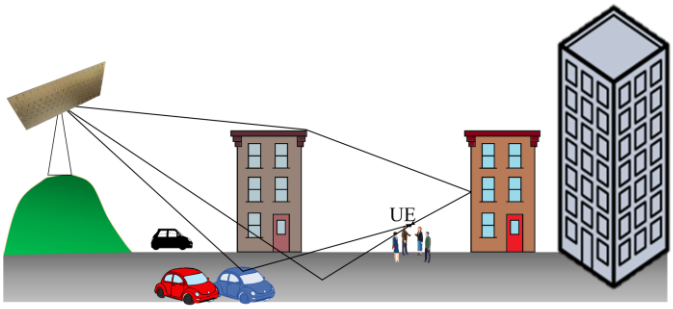

(a) Propagation environment

Rayleigh distribution

Uniform distribution

Antenna port	Magnitude [W]	Phase [°]
1	0.44	150
2	0.62	33
3	0.52	-12
4	0.37	13
5	1	-30
…	…	…
64	0.19	-120

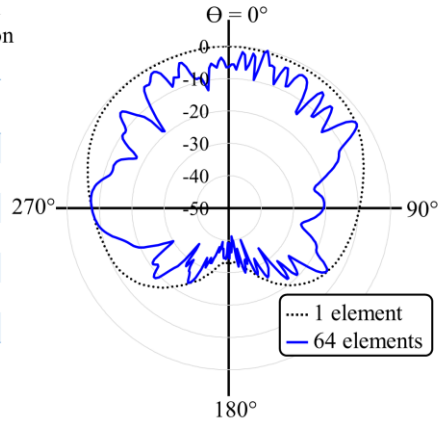

(b) Radiation pattern and excitation

Figure 4.13. Array radiation pattern analysis under a Rayleigh propagation environment.

Figure 4.14 presents the 16 dual-polarized active elements resultant radiation pattern, whereas Figure 4.15 the complete 64 dual-polarized antenna array. Moreover, Figure 4.14(a) and Figure 4.15(a) are under the same channel influence and Figure 4.14(b) and Figure 4.15(b) under a second channel influence. The difference between the two considered channels is just their generation, but under the same statistical parameters, i.e., Rayleigh distribution in magnitude and uniform distribution in phase resulted from a complex channel with zero-mean Gaussian distribution in both real and complex parts. We have considered the Gaussians with $\sigma = 4$. So they are two uncorrelated multipath channels with the same distribution, i.e, two events of the same stochastic process.

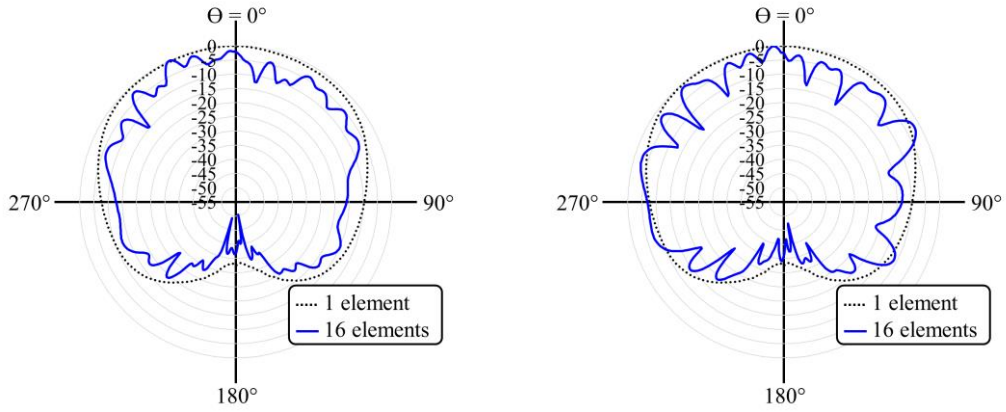

(a) Channel 1 (b) Channel 2

Figure 4.14. Radiation pattern analysis for 16 active elements under the influence of two identically distributed and independent Rayleigh channels.

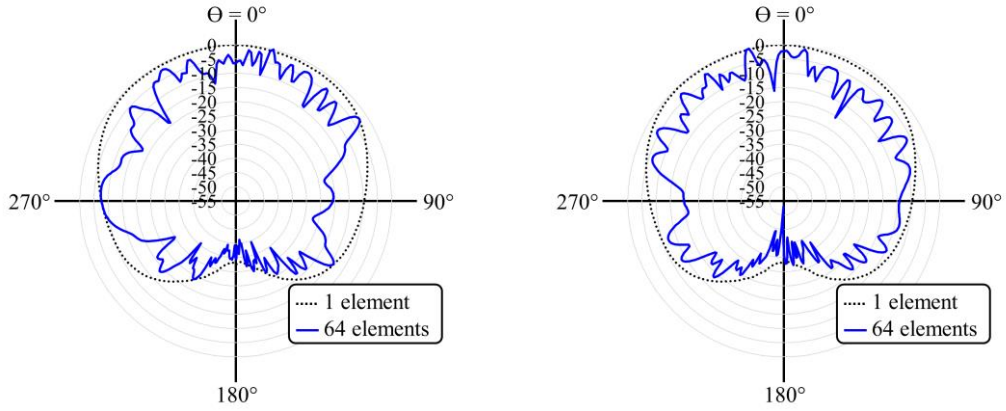

(a) Channel 1 (b) Channel 2

Figure 4.15. Radiation pattern analysis for 64 active elements under the influence of two identically distributed and independent Rayleigh channels.

One more time the two achievements from mMIMO systems are proved by applying our radiation pattern analysis to the SICL-SAA, as reported in Figures 4.14 and 4.15. Consequently, this study of case with a 64-element antenna array prototype validates the analysis of the theoretical dipole-based array from Section III. In other words, increasing the mMIMO array number of elements implies in enhancing the radiation pattern maxima and nulls and they are ruled by the channel variations.

The final step was regarding the Λ factor calculation for the SICL-SAA prototype, applying the Channel 1 conditions, as in dipole array case, and its radiation patterns reported in Figure 4.16. By applying (4.1), it is obtained Λ = 5.64 lobes/rad for $\theta_{ab\_element}$ = 122°. By reducing the analyzed coverage, i.e., the considered beamwidth (θ_{ab}) in Equation (4.1), the new values of our figure of merit are displayed

in Table 4.3. It is important to highlight that we are not proposing to change the radiating element, but only evaluating the Λ factor for diferrent angular locations from the same antenna array. One can observe that as θ_{ab} reduces and the antenna array element provides a flatter gain, the Λ factor tends to be to the theoretical value from the dipole analysis, i.e. Λ = 11.46 lobes/rad for the Channel 1. This behavior indicates that the dipole Λ factor is the upper limit, which is mostly related to the channel variation itself, since the element radiation is constant.

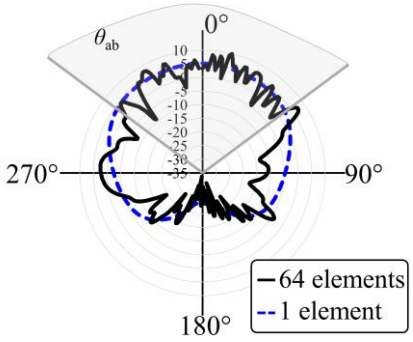

Figure 4.16. Non-normalized SICL-SAA radiation pattern analysis for 64 active elements under the influence of a Rayleigh channel.

Table 4.3 – Relation between the analyzed coverage area and Λ value.

θ_{ab} [°]	Λ [lobes/rad]
122	5.64
85	5.99
40	7.16
20	8.6
10	11.46
5	11.46

4.3. SICL-SAA characterization

We have manufactured a prototype using printed circuit board (PCB) technology for the slots and SICL feeding line, and milling process for the aluminum back cavities. Figure 4.17 shows the SICL-SAA prototype photograph, in which the ports numbering is identified. Six array elements positioned at different strategic positions have been connectorized for initial evaluation, named as ports 1, 16, 17, 22, 35 and 64. We have used a PNA N5224A Network Analyzer from Keysight for evaluating the proposed antenna array frequency response in terms of the *S*-parameters, presented in Figure 4.18. One can notice an excellent agreement between the numerical and experimental results in terms of bandwidth. Moreover, all antenna elements have the same bandwidth, i.e., 2 GHz from 24.5 to 26.5 GHz (7.8%) considering S_{11} < 10 dB,

and a 1 GHz bandwidth for a tougher impedance matching requirement of S_{11} < 15 dB. A resonance frequency shift of only 1.2% has been observed between the simulated and measured results, which can be considered acceptable considering the design and fabrication complexity. The mutual coupling between the adjacent elements has been kept lower than -23 dB throughout the entire antenna operating bandwidth, even for the measured worst-case, $S_{16\text{-}17}$, ensuring reliable mMIMO performance. Finally, we have computed the ECC value between ports 16 and 17, for establishing the correlation level between them. ECC should be as low as possible for mMIMO applications [122] and our prototype has provided ECC < 60 dB, i.e, < 0.001 in linear format, throughout its entire operating bandwidth (Figure 4.18), which is an outstanding value. We have computed the ECC value by using *S* parameters, which is simpler to obtain compared to the 3-dimensional radiation pattern method and provide similar results if the antennas have radiation efficiency ≥ 50% [122].

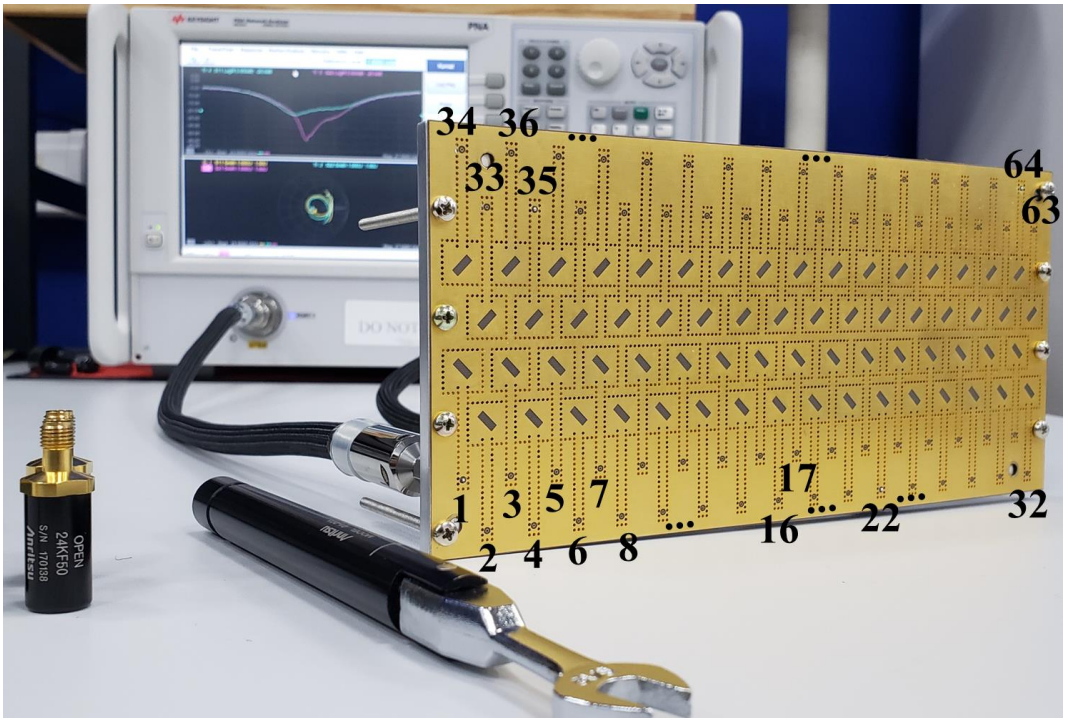

Figure 4.17. 64-element SICL-SAA prototype, with port identification, under characterization.

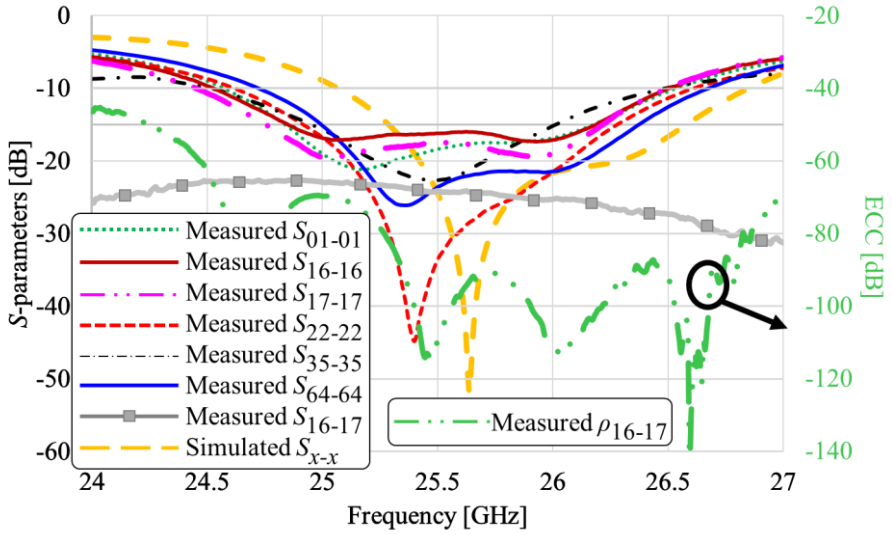

Figure 4.18. SICL-SAA *S*- and ρ parameters: measurements of the six chosen ports; a curve representing all simulated ports ($S_{x\text{-}x}$), which are approximately equal; measured ECC value in the worst-case scenario ($\rho_{16\text{-}17}$).

Figure 4.19 reports comparisons between the SICL-SAA simulated and measured radiation pattern at 26 GHz, considering a unique active element, for the two main orthogonal planes (φ = 0° and φ = 90°). Furthermore, we present the slots simulated cross-polarization discrimination (cross-pol), which have been always kept lower than -20 dB. It is possible to observe all array elements provide approximately the same radiation pattern, which means they suffer interference neither from each other nor the array structure. This result proves the element capability of independently operating into a 64-element and dual-polarized array, as desired for the 5G NR fully-digital TDD-based mMIMO applications. All array elements provide 85° beamwidth in both planes and 7.4 dBi gain, which is also in agreement with the simulations.

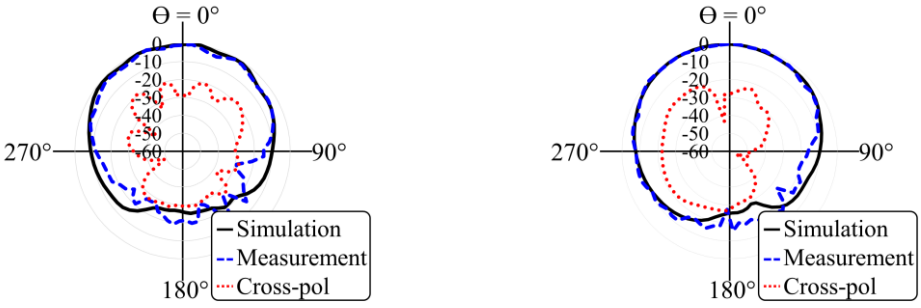

(a) Port 1: φ = 0° (b) Port 1: φ = 90°

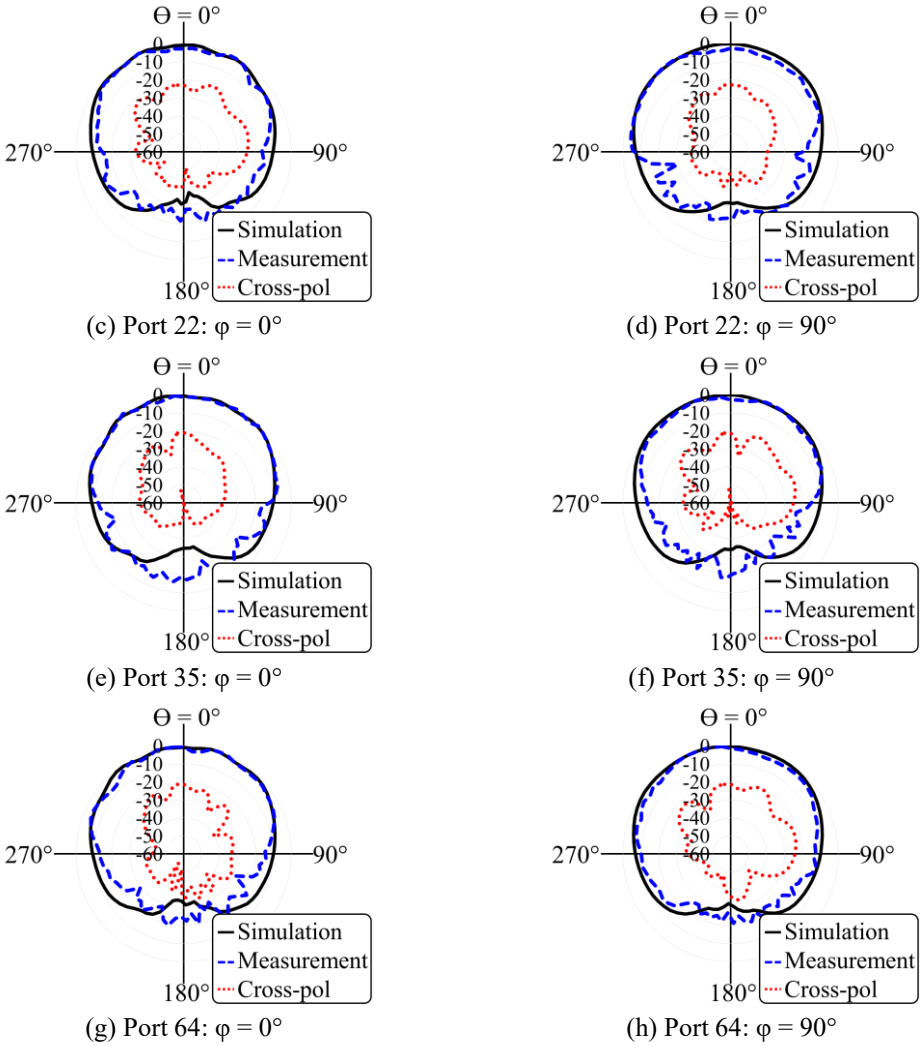

(c) Port 22: φ = 0°

(d) Port 22: φ = 90°

(e) Port 35: φ = 0°

(f) Port 35: φ = 90°

(g) Port 64: φ = 0°

(h) Port 64: φ = 90°

Figure 4.19. SICL-SAA radiation pattern at 26 GHz.

With the antenna elements properly characterized in terms of radiation pattern and gain, it is possible to estimate their radiation efficiency. By considering the elements gain in liner scale, i.e, G = 5.5, and the beamwidth in both planes $\phi_{ab} = \theta_{ab} = 85°$ from the characterization experiments, we could calculate the antenna elements directivity by applying

$$D = \frac{41253}{\emptyset_{ab}\theta_{ab}} \tag{4.2}$$

from [104], resulting on D = 5.71. As we know, the radiation efficiency (k) can be obtained by the relation between directivity and gain, i.e., $k = G/D$ [104]. Our antenna element has provided k = 96.3%, which is an excellent efficiency value.

Finally, a comparison among our proposal and other papers from literature can be obtained by revisting Tables 1.1, 1.2 and 1.3, from Chapter 1. Our array provides one of the widest bandwidth, more indepenedent feeded elements with dual-polarization and its mutual coupling in the worst-case scenario ($S_{16\text{-}17}$) is at the same level of the literature. Any other coupling analysis returns lower values.

Chapter 5
5. Conclusions and Future Works

This Thesis was focused on two main goals: ***i*)** reporting the concept and development of a 64 element and dual polarized slot based antenna array, fed by a substrate integrated coaxial line and applied to TDD-based digital mMIMO antenna array operating in the 26 GHz band; ***ii*)** presenting a new methodology based on a novel figure of merit for evaluating large-scale antenna arrays from TDD-based fully-digital MIMO systems, taking into account the channel response impact on the antenna array radiation pattern. The manuscript was structured in five Chapters, whose the main conclusions are described in sequence, as well as proposal of future works.

In Chapter 1, a brief contextualization on the evolution of mobile communication systems was presented. We have discussed the increased data demand and 5G NR solutions from the 3GPP Release 15 to fulfill the 5G scenarios requirements. Furthermore, the state-of-the-art on access networks and technologies has been described into details, including mm-waves, massive MIMO and radio-over-fiber and even THz communications that have been proposed for future generations of mobile communications, including 6G. Moreover, we have reported the state-of-the-art on antenna solutions aimed at mm-waves and mMIMO applications, dividing into two research categories: antenna element design for mm-waves; antenna array design aimed at MIMO and mMIMO applications. The antenna array research was categorized on manufacturing technology, operating bandwidth, array order and topology, and mutual coupling response.

Chapter 2 was regarding the system enabling technologies and their theoretical fundamentals. We have discussed the 5G NR Release 15 main access network

technologies for understanding its solutions to provide the expected massive amount of data to be demanded by the user in the following years. Particularly, we have focused on discussing the most important topics for understanding the research areas of study and contributions, including: frequency range definition; numerology; duplexing techniques; resource allocation; multiple access; switched beam; MIMO channel representation; diversity techniques; multiplexing scheme; TDD based digital massive MIMO systems.

The SICL-SAA development has been reported in Chapter 3. Iniatially, we have conducted a deep evaluation of the feeding networks applied to massive MIMO antenna array excitation and opted for the SICL technique for ensuring low mutual coupling among distinct feeding lines. Posterior, we have evolved into the slot antenna element design through 6 steps, including the slot design, SICL integration, cavity employment for reducing coupling between adjacent slots, feeding line adjustment for impedance matching and *K* connector to SICL transition design. Afterward, we have proposed and analyzed the 64-element and dual polarized antenna array arrangement over 5 steps: aligned elements and distinct feeding lines; shifted elements and distinct feeding lines; shifted elements and with the same SICL length; prepreg employment; final 64 element full-wave numerical model. The numerical SICL-SAA model provided a 1.8 GHz bandwidth, from 25 to 26.8 GHz (6.9%), considering S_{11} < -10 dB and a 1 GHz bandwidth for S_{11} < -20 dB. Furthermore, it has achieved a beamwidth of approximately 85° in both planes and 7 dBi gain at 26 GHz. Coupling among the array elements has been kept lower than -44 dB throughout the entire antenna operating bandwidth, ensuring outstanding performance. The SICL-SAA numerical investigation was also based on the active reflection coefficient, considering the coupling among elements when they are all activated, implying in a bandwidth from 25 to 26.6 GHz.

Finally, Chapter 4 has presented the research main achievements. We presented, for the first time in literature, a methodology for evaluating large-scale antenna arrays from TDD-based fully-digital massive multiple-input multiple-output systems, taking into account the channel response impact on the antenna array radiation pattern. Our methodology differs from the conventional antenna array analysis by evaluating the

spatial resolution and diversity performance, exclusively interpreting the digitally-beamformed resultant radiation pattern. Specifically, the proposed approach enables to investigate the impact on the mMIMO spatial resolution, as a function of the channel correlation, by simply using a RF approach, with the advantage of not considering the system-level features. In addition, a new figure of merit, named Λ factor, has been created for investigating the performance of the resultant antenna array radiation pattern, which is governed by the array elements phase and magnitude that are defined by the wireless channel response.

The Λ factor has been applied to a theoretical dipole-based array for properly understanding the array coverage capability under a multipath channel. It has been proved that as Λ increases, the antenna array becomes capable to cover a wider area, using more prominent and narrow beams, i.e. higher spatial resolution. As a consequence, the higher is the array number of elements, higher the Λ factor is. Additionally, it has been observed the radiation pattern maxima and nulls are ruled by the channel multipath, which means it is constantly adjusted as the wireless channel changes. The proposed methodology could be considered useful for analyzing the resultant antenna array radiation pattern from TDD-based mMIMO systems, as well as potential for evaluating the advantages of using different antenna types as the array elements (crossed dipoles, patches, slots and others) and array topologies for different wireless environments.

The last results were concerning the SICL-SAA prototype characterization and the proposed figure of merit results. Experimental results demonstrated a 2 GHz bandwidth in the lowest range of the 5G NR FR2, around 26 GHz, mutual coupling between adjacent elements lower than -23 dB, 85º beamwidth in both orthogonal planes, 7.4 dBi gain and ECC < -60 dB. In spite of being conceived for TDD-based applications, our array might also be utilized in frequency division duplexing (FDD)-based MIMO systems. The SICL-SAA study of case demonstrated that Λ factor tends to that of the dipole-based antenna array with the same number of elements, under the same wireless channel conditions, as the antenna element gain gets flatter, which has showed that the dipole-based antenna array Λ factor might be used as an upper limit.

Two research paths can be highlighted for future works. The first one is related to the SICL-SAA application in real 5G deployments. Carrying out system-level experiments with multiple RF chains to validate its applicability and system capacity enhancement. The second line of future research consists of further exploring the new figure of merit, in which we could apply it to different antenna array elements and topologies, distinct channel distributions and even carrying out experiments considering real wireless environments. Furthermore, analytical investigations could be performed to correlate the Λ factor with known metrics such as ECC, TARC and mutual coupling. Finally, statistical evaluation on array factor theory could be applied to estimate the array radiation pattern without the need for full-wave simulations of the entire array.

References

[1] R. Agrawal and A. Bedekar, “Network Architectures for 4G: Cost Considerations [Wireless Broadband Access],” *IEEE Commun. Mag.*, vol. 45, no. 12, pp. 76-81, Dec. 2007.

[2] China Mobile Research Institute, “C-RAN The Road Towards Green RAN”, White Paper, Oct. 2011.

[3] E. Westerberg, “4G/5G RAN Architecture: How a Split Can Make the Difference,” *Ericsson Technology Review*, vol. 93, no. 6, p. 1-16, Jul. 2016.

[4] A. D. La Oliva *et al*., “Xhaul: toward an integrated fronthaul/backhaul architecture in 5G networks,” *IEEE Wireless Commun.*, vol. 22, no. 5, pp. 32-40, Oct. 2015.

[5] Cisco Systems, “Cisco 5G Vision Series: Laying the Foundation for New Technologies, Use Cases, and Business Models,” White Paper, Apr. 2016.

[6] DMC R&D Center, Samsung Electronics Co., Ltd., “5G Vision,” White Paper, 2015.

[7] 3GPP, “5G; Study on Scenarios and Requirements for Next Generation Access Technologies,” 3GPP TR 38.913 version 14.2.0 Release 14, 2017.

[8] I. Philbeck, “Connecting the Unconnected; Working together to achieve Connect 2020 Agenda Targets,” ITU White Paper, 2017.

[9] M. C. Parker *et al*., “CHARISMA: Converged heterogeneous advanced 5G cloud-RAN architecture for intelligent and secure media access,” in *European Conference on Networks and Communications (EuCNC)*, Athens, Greece, 2016, pp. 240-244.

[10] M. C. Parker *et al.*, "Ultra-low latency 5G CHARISMA architecture for secure intelligent transportation verticals," in *19th International Conference on Transparent Optical Networks (ICTON)*, Girona, Spain, 2017, pp. 1-4.

[11] M. Mueck *et al*., "5G CHAMPION - Rolling out 5G in 2018," in *IEEE Globecom Workshops (GC Wkshps)*, Washington DC, United States of America, 2016, pp. 1-6.

[12] S. H. Won *et al*., "Development of 5G CHAMPION testbeds for 5G services at the 2018 Winter Olympic Games," in *IEEE 18th International Workshop on Signal Processing Advances in Wireless Communications (SPAWC)*, Sapporo, Japan, 2017, pp. 1-5.

[13] Radiocommunications Reference Center (CRR) from Inatel. Accessed May 12th, 2021. [Online]. Available: https://inatel.br/crr/.

[14] W. Dias *et al*., "Performance Analysis of a 5G Transceiver Implementation for Remote Areas Scenarios," *2018 European Conference on Networks and Communications (EuCNC)*, 2018, pp. 363-367.

[15] W. Dias, A. Ferreira, R. Kagami, J. S. Ferreira, D. Silva and L. Mendes, "5G-RANGE: A transceiver for remote areas based on software-defined radio," *2020 European Conference on Networks and Communications (EuCNC)*, 2020, pp. 100-104.

[16] 5G Range. Accessed May 12th, 2021. [Online]. Available: http://5g-range.eu/.

[17] I. B. F. de Almeida, L. L. Mendes, J. J. P. C. Rodrigues and M. A. A. da Cruz, "5G Waveforms for IoT Applications," in *IEEE Communications Surveys & Tutorials*, vol. 21, no. 3, pp. 2554-2567, third quarter 2019.

[18] Evoluindo com as Telecomunicações, Inatel integra grupo pioneiro no mundo de pesquisas sobre 6G. Accessed May 12th, 2021. [Online]. Available: https://inatel.br/imprensa/noticias/pesquisa-e-inovacao/3426-inatel-integra-grupo-pioneiro-no-mundo-de-pesquisas-sobre-6g.

[19] 6G Brasil Workshop. Accessed May 12th, 2021. [Online]. Available: https://cursos.inatel.br/lp-workshop-de-6g.

[20] 6G Flagship. Accessed May 12th, 2021. [Online]. Available: https://www.oulu.fi/6gflagship/.

[21] H. R. D. Filgueiras, R. M. Borges, M. Caldano Melo, T. H. Brandão and Arismar Cerqueira S. Jr., "Dual-Band Wireless Fronthaul Using a FSS-Based Focal-Point/Cassegrain Antenna Assisted by an Optical Midhaul," in *IEEE Access*, vol. 7, pp. 112578-112587, 2019.

[22] A. Tzanakaki *et al*., "Wireless-Optical Network Convergence: Enabling the 5G Architecture to Support Operational and End-User Services," *IEEE Commun. Mag.*, vol. 55, no. 10, pp. 184-192, Oct. 2017.

[23] G. Kalfas *et al*., "Next Generation Fiber-Wireless Fronthaul for 5G mmWave Networks," *IEEE Commun. Mag.*, vol. 57, no. 3, pp. 138-144, Mar. 2019.

[24] T. H. Brandão *et al*., "Coherent dual-band radar system based on a unique antenna and a photonics-based transceiver," *IET Radar, Sonar & Navigation*, vol. 13, no. 4, pp. 505-511, Apr. 2019.

[25] R. M. Borges *et al*., "Integration of a GFDM-Based 5G Transceiver in a GPON Using Radio Over Fiber Technology," *J. Lightw. Technol.*, vol. 36, no. 19, pp. 4468-4477, Oct. 2018.

[26] C. Lim, Y. Tian, C. Ranaweera, T. A. Nirmalathas, E. Wong, and K. Lee, "Evolution of Radio-Over-Fiber Technology," *J. Lightw. Technol.*, vol. 37, no. 6, pp. 1647-1656, Mar. 2019.

[27] R. M. Borges *et al*., "DSP-Based Flexible-Waveform and Multi-Application 5G Fiber-Wireless System," in *Journal of Lightwave Technology*, vol. 38, no. 3, pp. 642-653, 1 Feb.1, 2020.

[28] G. Brown, "Exploring the Potential of mmWave for 5G Mobile Access," Qualcomm White Paper, 2016.

[29] C. Wallace, "Bringing 5G networks indoors," Ericsson White Paper, 2019.

[30] HKT, GSA and Huawei, "Indoor 5G Scenario Oriented White Paper," version 3.0, White Paper, 2019.

[31] 3GPP, “Group Radio Access Network; NR; User Equipment (UE) radio transmission and reception; Part 1: Range 1 Standalone,” 3GPP TS 38.101-1 version 15.5.0 Release 15, 2019-03.

[32] M. L. K. Latva-aho, “Key drivers and research challenges for 6G ubiquitous wireless intelligence”, White Paper, University of Oulu, 2019. [Online]. Available: http://urn.fi/urn:isbn:9789526223544.

[33] Z. Zhang *et al*., “6G Wireless Networks: Vision, Requirements, Architecture, and Key Technologies,” in *IEEE Vehicular Technology Magazine*, vol. 14, no. 3, pp. 28-41, Sept. 2019.

[34] T. S. Rappaport *et al*., “Wireless Communications and Applications Above 100 GHz: Opportunities and Challenges for 6G and Beyond,” in *IEEE Access*, vol. 7, pp. 78729-78757, 2019.

[35] T. S. Rappaport *et al*., “Millimeter Wave Mobile Communications for 5G Cellular: It Will Work!,” in *IEEE Access*, vol. 1, pp. 335-349, 2013.

[36] C. Wang, J. Bian, J. Sun, W. Zhang and M. Zhang, “A Survey of 5G Channel Measurements and Models,’ in *IEEE Communications Surveys & Tutorials*, vol. 20, no. 4, pp. 3142-3168, 2018.

[37] S. Kutty and D. Sen, “Beamforming for Millimeter Wave Communications: An Inclusive Survey,” in *IEEE Communications Surveys & Tutorials*, vol. 18, no. 2, pp. 949-973, 2016.

[38] E. G. Larsson, O. Edfors, F. Tufvesson and T. L. Marzetta, “Massive MIMO for next generation wireless systems,” in *IEEE Communications Magazine*, vol. 52, no. 2, pp. 186-195, 2014.

[39] F. Rusek *et al*., “Scaling Up MIMO: Opportunities and Challenges with Very Large Arrays,” in *IEEE Signal Processing Magazine*, vol. 30, no. 1, pp. 40-60, 2013.

[40] T. S. Rappaport, G. R. MacCartney, M. K. Samimi and S. Sun, “Wideband Millimeter-Wave Propagation Measurements and Channel Models for Future Wireless Communication System Design,” in *IEEE Transactions on Communications*, vol. 63, no. 9, pp. 3029-3056, Sept. 2015.

[41] S. Pratschner *et al.*, "A Spatially Consistent MIMO Channel Model With Adjustable K Factor," in *IEEE Access*, vol. 7, pp. 110174-110186, 2019.

[42] H. Q. Ngo, E. G. Larsson and T. L. Marzetta, "Aspects of favorable propagation in Massive MIMO," *2014 22nd European Signal Processing Conference (EUSIPCO)*, Lisbon, 2014, pp. 76-80.

[43] E. Björnson, E. G. Larsson and T. L. Marzetta, "Massive MIMO: ten myths and one critical question," in *IEEE Communications Magazine*, vol. 54, no. 2, pp. 114-123, February 2016.

[44] J. Park, J. Ko, H. Kwon, B. Kang, B. Park and D. Kim, "A Tilted Combined Beam Antenna for 5G Communications Using a 28-GHz Band," in *IEEE Antennas and Wireless Propagation Letters*, vol. 15, pp. 1685-1688, 2016.

[45] Y. Yashchyshyn *et al.*, "28 GHz Switched-Beam Antenna Based on S-PIN Diodes for 5G Mobile Communications," in *IEEE Antennas and Wireless Propagation Letters*, vol. 17, no. 2, pp. 225-228, Feb. 2018.

[46] C. Mao, M. Khalily, P. Xiao, T. W. C. Brown and S. Gao, "Planar Sub-Millimeter-Wave Array Antenna With Enhanced Gain and Reduced Sidelobes for 5G Broadcast Applications," in *IEEE Transactions on Antennas and Propagation*, vol. 67, no. 1, pp. 160-168, Jan. 2019.

[47] Y. Zhang, J. Deng, M. Li, D. Sun and L. Guo, "A MIMO Dielectric Resonator Antenna With Improved Isolation for 5G mm-Wave Applications," in *IEEE Antennas and Wireless Propagation Letters*, vol. 18, no. 4, pp. 747-751, April 2019.

[48] X. Wang, Y. Cheng and Y. Dong, "A Wideband PCB-Stacked Air-Filled Luneburg Lens Antenna for 5G Millimeter-Wave Applications," in *IEEE Antennas and Wireless Propagation Letters*, Early Access, 2021.

[49] M. Xue, W. Wan, Q. Wang and L. Cao, "Low-Profile Millimeter-Wave Broadband Metasurface Antenna with Four Resonances," in *IEEE Antennas and Wireless Propagation Letters*, Early Access, 2021.

[50] Y. Gao, R. Ma, Y. Wang, Q. Zhang and C. Parini, “Stacked Patch Antenna With Dual-Polarization and Low Mutual Coupling for Massive MIMO,” in *IEEE Transactions on Antennas and Propagation*, vol. 64, no. 10, pp. 4544-4549, Oct. 2016.

[51] M. V. Komandla, G. Mishra and S. K. Sharma, “Investigations on Dual Slant Polarized Cavity-Backed Massive MIMO Antenna Panel With Beamforming,” in *IEEE Transactions on Antennas and Propagation*, vol. 65, no. 12, pp. 6794-6799, Dec. 2017.

[52] X. Yang *et al*., “Design and implementation of a TDD-based 128-antenna massive MIMO prototype system,” in *China Communications*, vol. 14, no. 12, pp. 162-187, December 2017.

[53] Y. Hu *et al*., “A Digital Multibeam Array With Wide Scanning Angle and Enhanced Beam Gain for Millimeter-Wave Massive MIMO Applications,” in *IEEE Transactions on Antennas and Propagation*, vol. 66, no. 11, pp. 5827-5837, Nov. 2018.

[54] S. Li, Z. N. Chen, T. Li, F. H. Lin and X. Yin, “Characterization of Metasurface Lens Antenna for Sub-6 GHz Dual-Polarization Full-Dimension Massive MIMO and Multibeam Systems,” in *IEEE Transactions on Antennas and Propagation*, vol. 68, no. 3, pp. 1366-1377, March 2020.

[55] M. Temiz, E. Alsusa, L. Danoon and Y. Zhang, “On the Impact of Antenna Array Geometry on Indoor Wideband Massive MIMO Networks,” in *IEEE Transactions on Antennas and Propagation*, vol. 69, no. 1, pp. 406-416, Jan. 2021.

[56] Y. Aslan, A. Roederer and A. Yarovoy, “System Advantages of Using Large-Scale Aperiodic Array Topologies in Future mm-Wave 5G/6G Base Stations: An Interdisciplinary Look,” in *IEEE Systems Journal*, Early Access, 2021.

[57] I. F. da Costa, A. Cerqueira S., D. H. Spadoti, L. G. da Silva, J. A. J. Ribeiro and S. E. Barbin, “Optically Controlled Reconfigurable Antenna Array for mm-Wave Applications,” in *IEEE Antennas and Wireless Propagation Letters*, vol. 16, pp. 2142-2145, 2017.

[58] Arismar Cerqueira S. Jr., I. F. da Costa, R. A. dos Santos, H.R.D. Filgueiras and D. H. Spadoti, "Waveguide-Based Antenna Arrays for 5G Networks," in *International Journal of Antennas and Propagation*, vol. 2018, pp. 1-10, 2018.

[59] E. C. Vilas Boas, H.R.D. Filgueiras, I. F. da Costa, J. A. J. Ribeiro and Arismar Cerqueira S. Jr., "Dual-band switched-beam antenna array for MIMO systems," in *IET Microwaves, Antennas & Propagation*, vol. 14, no. 1, pp. 82-87, 2020.

[60] E. C. Vilas Boas, R. Mittra and Arismar Cerqueira S. Jr., "A Low-Profile High-Gain Slotted Waveguide Antenna Array With Grooved Structures," in *IEEE Antennas and Wireless Propagation Letters*, vol. 19, no. 12, pp. 2107-2111, 2020.

[61] E. S. Lima, R. M. Borges, L. A. Melo Pereira, H. R. D. Filgueiras, A. M. Alberti and Arismar Cerqueira S. Jr., "Multiband and Photonically Amplified Fiber-Wireless Xhaul," in *IEEE Access*, vol. 8, pp. 44381-44390, 2020.

[62] H.R.D. Filgueiras, J. R. Kelly, Pei Xiao, I. F. da Costa and Arismar Cerqueira S. Jr., "Wideband Omnidirectional Slotted-Waveguide Antenna Array Based on Trapezoidal Slots," in *International Journal of Antennas and Propagation*, vol. 2019, pp. 1-8, 2019.

[63] H. R. D. Filgueiras, E. S. Lima, T. H. Brandão and A. Cerqueira S., "5G NR FR2 Femtocell Coverage Map Using an Omnidirectional Twisted SWAA," in *IEEE Open Journal of Antennas and Propagation*, vol. 2, pp. 72-78, 2021.

[64] 3GPP, "3GPP-Study on New Radio (NR) access technology," 3GPP TR 38.912 version 16.0.0 Release 16, 2020-07.

[65] 3GPP, "5G; NR; User Equipment (UE) radio transmission and reception; Part 2: Range 2 Standalone," 3GPP TS 38.101-2 version 15.2.0 Release 15, 2018-07.

[66] P. K. Korrai, E. Lagunas, A. Bandi, S. K. Sharma and S. Chatzinotas, "Joint Power and Resource Block Allocation for Mixed-Numerology-Based 5G Downlink Under Imperfect CSI" in *IEEE Open Journal of the Communications Society*, vol. 1, pp. 1583-1601, 2020.

[67] H. Yin, L. Zhang and S. Roy, “Multiplexing URLLC Traffic Within eMBB Services in 5G NR: Fair Scheduling,” in *IEEE Transactions on Communications*, vol. 69, no. 2, pp. 1080-1093, Feb. 2021.

[68] A. K. Bairagi *et al.*, “Coexistence Mechanism between eMBB and uRLLC in 5G Wireless Networks,” in *IEEE Transactions on Communications*, 2021, Early Access.

[69] S. Chen, S. Sun, Y. Wang, G. Xiao and R. Tamrakar, “A comprehensive survey of TDD-based mobile communication systems from TD-SCDMA 3G to TD-LTE(A) 4G and 5G directions,” in *China Communications*, vol. 12, no. 2, pp. 40-60, Feb. 2015.

[70] H. Xie, F. Gao, S. Zhang and S. Jin, “A Unified Transmission Strategy for TDD/FDD Massive MIMO Systems with Spatial Basis Expansion Model,” in *IEEE Transactions on Vehicular Technology*, vol. 66, no. 4, pp. 3170-3184, April 2017.

[71] H. Xie, F. Gao, S. Jin, J. Fang and Y. -C. Liang, “Channel Estimation for TDD/FDD Massive MIMO Systems with Channel Covariance Computing,” in *IEEE Transactions on Wireless Communications*, vol. 17, no. 6, pp. 4206-4218, June 2018.

[72] H. Taha and E. Alsusa, “Secret Key Exchange Using Private Random Precoding in MIMO FDD and TDD Systems,” in *IEEE Transactions on Vehicular Technology*, vol. 66, no. 6, pp. 4823-4833, June 2017.

[73] J. Flordelis, F. Rusek, F. Tufvesson, E. G. Larsson and O. Edfors, “Massive MIMO Performance—TDD Versus FDD: What Do Measurements Say?,” in *IEEE Transactions on Wireless Communications*, vol. 17, no. 4, pp. 2247-2261, April 2018.

[74] W. Peng, W. Li, W. Wang, X. Wei and T. Jiang, “Downlink Channel Prediction for Time-Varying FDD Massive MIMO Systems,” in *IEEE Journal of Selected Topics in Signal Processing*, vol. 13, no. 5, pp. 1090-1102, Sept. 2019.

[75] F. Rottenberg, T. Choi, P. Luo, C. J. Zhang and A. F. Molisch, “Performance Analysis of Channel Extrapolation in FDD Massive MIMO Systems,” in *IEEE*

Transactions on Wireless Communications, vol. 19, no. 4, pp. 2728-2741, April 2020.

[76] E. Zeydan, O. Dedeoglu and Y. Turk, "Experimental Evaluations of TDD-Based Massive MIMO Deployment for Mobile Network Operators," in *IEEE Access*, vol. 8, pp. 33202-33214, 2020.

[77] A. Sheikhi, S. M. Razavizadeh and I. Lee, "A Comparison of TDD and FDD Massive MIMO Systems Against Smart Jamming," in *IEEE Access*, vol. 8, pp. 72068-72077, 2020.

[78] J. Ø. Nielsen, A. Karstensen, P. C. F. Eggers, E. De Carvalho, G. Steinböck and M. Alm, "Precoding for TDD and FDD in Measured Massive MIMO Channels," in *IEEE Access*, vol. 8, pp. 193644-193654, 2020.

[79] J. Chuang and N. Sollenberger, "Beyond 3G: wideband wireless data access based on OFDM and dynamic packet assignment," in *IEEE Communications Magazine*, vol. 38, no. 7, pp. 78-87, July 2000.

[80] J. Lee, H. Noh and J. Lim, "Dynamic Cooperative Retransmission Scheme for TDMA Systems," in *IEEE Communications Letters*, vol. 16, no. 12, pp. 2000-2003, December 2012.

[81] J. Zhang, L. Yang, L. Hanzo and H. Gharavi, "Advances in Cooperative Single-Carrier FDMA Communications: Beyond LTE-Advanced," in *IEEE Communications Surveys & Tutorials*, vol. 17, no. 2, pp. 730-756, Second quarter 2015.

[82] M. Morelli, C. -. J. Kuo and M. Pun, "Synchronization Techniques for Orthogonal Frequency Division Multiple Access (OFDMA): A Tutorial Review," in *Proceedings of the IEEE*, vol. 95, no. 7, pp. 1394-1427, July 2007.

[83] D. A. Guimarães, *Digital Transmission – A Simulation-Aided Introduction with VisSim/Comm*, Springer, Berlin: Berlin/Heidelberg: Springer Verlag, vol. 1, pp. 585-688, 2009.

[84] M. Bossert, *Hadamard Matrices and Codes*, Wiley Encyclopedia of Telecommunications, Hoboken, New Jersey, USA: John Wiley & Sons, Inc., vol. 2, pp. 929–935, 2003.

[85] S. Ahmadi, *5G NR Architecture, technology, implementation, and operation of 3GPP New Radio Standards*, Elsevier Academia Press, London Wall, London, England, vol. 1, pp. 285-409, 2019.

[86] Y. Yang, J. Xu, G. Shi and C. X. Wang, *5G Wireless Systems: Simulations and Evaluations Techniques*, Springer, Gewerbestrasse 11, 6330 Cham, Switzerland, vol. 1, pp. 585-688, 2018.

[87] D. Lopez-Perez, A. Valcarce, G. de la Roche and J. Zhang, "OFDMA femtocells: A roadmap on interference avoidance," in *IEEE Communications Magazine*, vol. 47, no. 9, pp. 41-48, September 2009.

[88] H. Zhu and J. Wang, "Chunk-based resource allocation in OFDMA systems - part I: chunk allocation," in *IEEE Transactions on Communications*, vol. 57, no. 9, pp. 2734-2744, September 2009.

[89] 3GPP, "5G; NR; Overall Description; Stage-2," 3GPP TS 38.300 version 15.3.1 Release 15, 2018-10.

[90] B. Wang, F. Gao, S. Jin, H. Lin and G. Y. Li, "Spatial and Frequency Wideband Effects in Millimeter-Wave Massive MIMO Systems," in *IEEE Transactions on Signal Processing*, vol. 66, no. 13, pp. 3393–3406, 2018.

[91] J. Brady, N. Behdad and A. M. Sayeed, "Beamspace MIMO for Millimeter-Wave Communications: System Architecture, Modeling, Analysis, and Measurements," in *IEEE Transactions on Antennas and Propagation*, vol. 61, no. 7, pp. 3814–3827, 2013.

[92] A. Adhikary, E. Al Safadi, M. K. Samimi, R. Wang, G.Caire, T. S. Rappaport and A. F. Molisch, "Joint Spatial Division and Multiplexing for mm-Wave Channels," in *IEEE Journal on Selected Areas in Communications*, vol. 32, no. 6, pp. 1239–1255, 2014.

[93] L. Zheng and D. N. C. Tse, “Diversity and multiplexing: a fundamental tradeoff in multiple-antenna channels,” in *IEEE Transactions on Information Theory*, vol. 49, no. 5, pp. 1073–1096, 2003.

[94] S. M. Alamouti, “A simple transmit diversity technique for wireless communications,” in *IEEE Journal on Selected Areas in Communications*, vol. 16, no. 8, pp. 1451–1458, 1998.

[95] V. A. Aalo, “Performance of maximal-ratio diversity systems in a correlated Nakagami-fading environment,” in *IEEE Transactions on Communications*, vol. 43, no. 8, pp. 2360–2369, 1995.

[96] A. Leon-Garcia, *Probability, Statistics, and Random Process for Electrical Engeneering*, Pearson Prentice Hall: New Jersey, USA: Third Edition, pp. 359-410, 2008.

[97] 3GPP, “Study on Channel Model for Frequencies From 0.5 to 100 GHz,” 3GPP TR38.901 version 15.0.0 Release 15, 2018.

[98] V. Tarokh, N. Seshadri and A. R. Calderbank, “Space-time codes for high data rate wireless communication: performance criterion and code construction,” in *IEEE Transactions on Information Theory*, vol. 44, no. 2, pp. 744-765, March 1998.

[99] A. R. Hammons and H. El Gamal, “On the theory of space-time codes for PSK modulation,” in *IEEE Transactions on Information Theory*, vol. 46, no. 2, pp. 524-542, March 2000.

[100] J. N. Laneman, D. N. C. Tse and G. W. Wornell, “Cooperative diversity in wireless networks: Efficient protocols and outage behavior,” in *IEEE Transactions on Information Theory*, vol. 50, no. 12, pp. 3062-3080, Dec. 2004.

[101] Lizhong Zheng and D. N. C. Tse, “Diversity and multiplexing: a fundamental tradeoff in multiple-antenna channels,” in *IEEE Transactions on Information Theory*, vol. 49, no. 5, pp. 1073-1096, May 2003.

[102] S. Sun, T. S. Rappaport, R. W. Heath, A. Nix and S. Rangan, “MIMO for millimeter-wave wireless communications: beamforming, spatial multiplexing, or both?,” in *IEEE Communications Magazine*, vol. 52, no. 12, pp. 110-121, 2014.

[103] A. Gorokhov, D. A. Gore and A. J. Paulraj, “Receive antenna selection for MIMO spatial multiplexing: theory and algorithms,” in *IEEE Transactions on Signal Processing*, vol. 51, no. 11, pp. 2796-2807, 2003.

[104] C. A. Balanis, *Antenna Teory: Analysis and Design*, Wiley: New Jersey, USA: Third Edition, pp. 811-882, 2005.

[105] K. Carver and J. Mink, “Microstrip antenna technology,” in *IEEE Transactions on Antennas and Propagation*, vol. 29, no. 1, pp. 2-24, January 1981.

[106] Fan Yang and Y. Rahmat-Samii, “Microstrip antennas integrated with electromagnetic band-gap (EBG) structures: a low mutual coupling design for array applications,” in *IEEE Transactions on Antennas and Propagation*, vol. 51, no. 10, pp. 2936-2946, Oct. 2003.

[107] L. Yuan, K. Sun, S. Liu, B. Chen and D. Yang, “Wideband SIW Half-Mode/Quarter-Mode-Fed Microstrip Patch Complementary Antennas With Back Radiation Suppression,” in *IEEE Access*, vol. 9, pp. 48963-48970, 2021.

[108] E. Rajo-Iglesias, P.-S. Kildal, “Numerical studies of bandwidth of parallel-plate cut-off realised by a bed of nails, corrugations and mushroom-type electromagnetic bandgap for use in gap waveguides,” in *IET Microwaves, Antennas & Propagation*, vol. 5, no. 3, pp. 282-289, 2011.

[109] P.-S. Kildal, A. U. Zaman, E. Rajo-Iglesias, E. Alfonso and A. Valero-Nogueira, “Design and experimental verification of ridge gap waveguide in bed of nails for parallel-plate mode suppression,” in *IET Microwaves, Antennas & Propagation*, vol. 5, no. 3, pp. 262-270, 2011.

[110] H. Raza, J. Yang, P.-S. Kildal and E. Alfonso, “Resemblance between gap waveguides and hollow waveguides,” in *IET Microwaves, Antennas & Propagation*, vol. 7, no. 15, pp. 1221-1227, 2013.

[111] Feng Xu and Ke Wu, “Guided-wave and leakage characteristics of substrate integrated waveguide,” in *IEEE Transactions on Microwave Theory and Techniques*, vol. 53, no. 1, pp. 66-73, Jan. 2005.

[112] D. Deslandes and Ke Wu, “Accurate modeling, wave mechanisms, and design considerations of a substrate integrated waveguide,” in *IEEE Transactions on Microwave Theory and Techniques*, vol. 54, no. 6, pp. 2516-2526, June 2006.

[113] Li Yan, Wei Hong, Guang Hua, Jixin Chen, Ke Wu and Tie Jun Cui, “Simulation and experiment on SIW slot array antennas,” in *IEEE Microwave and Wireless Components Letters*, vol. 14, no. 9, pp. 446-448, Sept. 2004.

[114] J. Liu, D. R. Jackson and Y. Long, “Substrate Integrated Waveguide (SIW) Leaky-Wave Antenna With Transverse Slots,” in *IEEE Transactions on Antennas and Propagation*, vol. 60, no. 1, pp. 20-29, Jan. 2012.

[115] F. Gatti, M. Bozzi, L. Perregrini, K. Wu and R. G. Bosisio, “A Novel Substrate Integrated Coaxial Line (SICL) for Wide-Band Applications,*" 2006 European Microwave Conference*, Manchester, UK, 2006, pp. 1614-1617.

[116] F. Zhu, W. Hong, J. Chen and K. Wu, “Ultra-Wideband Single and Dual Baluns Based on Substrate Integrated Coaxial Line Technology,” in *IEEE Transactions on Microwave Theory and Techniques*, vol. 60, no. 10, pp. 3062-3070, Oct. 2012.

[117] A. Belenguer, A. L. Borja, H. Esteban and V. E. Boria, “High-Performance Coplanar Waveguide to Empty Substrate Integrated Coaxial Line Transition,” in *IEEE Transactions on Microwave Theory and Techniques*, vol. 63, no. 12, pp. 4027-4034, Dec. 2015.

[118] Y. Shao, X. Li, L. Wu and J. Mao, “A Wideband Millimeter-Wave Substrate Integrated Coaxial Line Array for High-Speed Data Transmission,” in *IEEE Transactions on Microwave Theory and Techniques*, vol. 65, no. 8, pp. 2789-2800, Aug. 2017.

[119] A. Li and K. -M. Luk, “Millimeter-Wave End-Fire Magneto-Electric Dipole Antenna and Arrays with Asymmetrical Substrate Integrated Coaxial Line Feed,” in *IEEE Open Journal of Antennas and Propagation*, vol. 2, pp. 62-71, 2021.

[120] J. A. J. Ribeiro, *Engenharia de Micro-ondas: Fundamentos e Aplicações*, Érica: São Paulo, Brazil: First Edition, pp. 173-205, 2012, in portuguese.

[121] W. H. Watson, “Resonant slots,” in *Journal of the Institution of Electrical Engineers - Part IIIA: Radiolocation*, vol. 93, no. 4, pp. 747-777, 1946.

[122] Jesper Thaysen and Kaj B. Jakobsen, “Envelope correlation in (N, N) MIMO antenna array from scattering parameters,” *Microwave and Optical Technology Letters*, vol. 48, no. 5, pp. 832-834, 2006.